

UCSF

UC San Francisco Electronic Theses and Dissertations

Title

Identification and characterization of the nucleotide exchange factor eIF2B as the target of a memory-enhancing inhibitor of the integrated stress response

Permalink

<https://escholarship.org/uc/item/7sz0s147>

Author

Tsai, Jordan

Publication Date

2018

Peer reviewed|Thesis/dissertation

Identification and characterization of the nucleotide exchange factor
eIF2B as the target of a memory-enhancing inhibitor of the integrated
stress response

by

Jordan C. Tsai

DISSERTATION

Submitted in partial satisfaction of the requirements for the degree of

DOCTOR OF PHILOSOPHY

in

Biochemistry and Molecular Biology

in the

GRADUATE DIVISION

of the

UNIVERSITY OF CALIFORNIA, SAN FRANCISCO

Dedicated to my family

Shawn, Toshi, Brandon, Pearl and Devon Tsai

ACKNOWLEDGEMENTS

It's a daunting a task to properly acknowledge all the different individuals in my life that made this dissertation possible. I promise to do my best.

I first want to thank my family for supporting me through the many years. It humbles me to recall my parents many sacrifices that enabled me to be here today. It was not easy for them to move to a new country away from family, to speak a new language, and to work as artists to support us growing up. However, out of love they embraced a more difficult life with the promise that our family would have the better future that is presently being realized. I want to thank my brother Brandon for being an older brother through it all, always reassuring me that I would finish and taking me out to eat as a hungry grad student. I want to thank Pearl who stood by my side through the many ups and downs of grad school. She was there through the many late nights in lab, the long drives home, and sustained me through a constant supply of prayers, encouragement, and love. Thanks egg! Thus this dissertation is dedicated to my family.

I want to thank Peter for his mentorship, generosity, vision, and naturally the opportunity to carry out my graduate research in his lab. It was a privilege to learn to be a scientist from Peter and to work with the amazing people in the lab he crafted over many years. There's not many places where you could work and pursue scientific questions with such freedom and I'm thankful to have been a part of it. Above all what I'm most grateful for is how Peter cared for me not only professionally but personally. He always promoted my well-being and interests to the best of his extent, and it's truly this that I'll miss most. Thanks Peter.

I want to thank faculty and thesis committee members Adam Frost, David Morgan, and Jonathan Weissman for their mentorship, guidance, and advice. They've been involved and

invested in my graduate career since the beginning and I'm thankful for their wisdom and scientific input.

I want to thank the whole Walter lab past and present for much scientific support and friendship over the years. Carmela, Martin, and Luke for mentoring me in the beginning. Aditya and Lakshmi for the amazing work we got done together, and the good times in lab. Owen for the friendship over the years and teaching me to TC. I want to thank Margaret, Elif, and Jirka for teaching me how to be a biochemist from AKTA and beyond. Marivic, Fran, Christine and Silke for just making everything actually work in our lab, and spending time to chat about life and everything else. I want to thank Billy, Danny, Rachel, and Toni for making the TETRAD graduate program actually function. None of us could do it without you guys!

I want to thank Jamie Cate for his decision to invest in me during my sophomore year of undergrad at UC Berkeley. It was in his lab I learned the foundations of scientific reasoning and cultivated a desire to do scientific research in the future. Additionally, from this time my mentors: Elizabeth Znameroski, Ian Wallace, and Owen Ryan.

I want to thank my many friends from college and church that supported me through grad school. There are really too many to name here, but many of them spent long nights in lab with me, bringing me dinner, bringing encouragement in the midst of failing experiments and long hours, driving back with me to the East Bay, and much more. These are the friends that were by my side through it all, and I'm thankful for the years and decades of committed friendship that persists in the highs and lows of life.

One thing I will take away from this whole experience is to continue seeking out both scientific and philosophical truths. In a day and age where truth no longer holds much sway and

value among the masses, we must be people who fight to reclaim reality and sanity. Indeed it's the truth that will set us free.

**IDENTIFICATION AND CHARACTERIZATION OF THE NUCLEOTIDE
EXCHANGE FACTOR EIF2B AS THE TARGET OF A MEMORY-ENHANCING
INHIBITOR OF THE INTEGRATED STRESS RESPONSE**

ABSTRACT

The mammalian integrated stress response (ISR) is a major translational control point activated in response to diverse cellular stresses, such as unfolded proteins in the ER, viral infection, heme-deficiency and amino-acid starvation. The ISR is mediated by four kinases that activate upon stress and phosphorylate the alpha subunit of eukaryotic translation initiation factor 2 (eIF2). This phosphorylation event renders eIF2 an inhibitor of its dedicated guanine exchange factor, eIF2B, leading to the attenuation of global protein synthesis and selective translation of uORF-containing mRNAs, e.g. the stress-responsive transcription factor ATF4. Using a cell-based screen, our lab discovered the small molecule ISRIB (integrated stress response inhibitor) which reverses the effects of eIF2 α -phosphorylation, restores protein synthesis and remarkably enhances cognition in both wild-type mice and corrects cognitive deficits after brain injury. In this work a reporter-based shRNA screen identified eIF2B as a potential molecular target of ISRIB. We found that ISRIB stabilizes an eIF2B heterodecamer and enhances the GEF activity of eIF2B independent of eIF2 phosphorylation. We also designed new analogs of ISRIB that improve its EC₅₀ to 600pM in cell culture. Furthermore, to gain mechanistic and structural insight into ISRIB's activity we established a robust recombinant system for eIF2B and solved a 2.8Å cryo-EM structure of ISRIB-bound human eIF2B. The structure revealed ISRIB's binding site at the symmetric core of the eIF2B heterodecamer. Structural and biochemical analyses further revealed that the fully active eIF2B heterodecamer depends on assembly of two identical tetrameric subcomplexes, and that

ISRIB promotes this step by bridging the symmetry interface. Thus, regulation of eIF2B assembly appears as a new translational control point central to the integrated stress response.

TABLE OF CONTENTS

CHAPTER 1

PHARMACOLOGICAL DIMERIZATION AND ACTIVATION OF THE EXCHANGE FACTOR EIF2B ANTAGONIZES THE INTEGRATED STRESS RESPONSE 1

ABSTRACT	3
INTRODUCTION	4
RESULTS.....	7
<i>Knockdown of eIF2B renders cells resistant to ISRIB.....</i>	<i>7</i>
<i>Structure-activity relationship of ISRIB suggests a twofold symmetric target.....</i>	<i>9</i>
<i>ISRIB promotes dimerization of eIF2B in cells</i>	<i>11</i>
<i>ISRIB enhances the thermo-stability of eIF2B4.....</i>	<i>13</i>
<i>ISRIB enhances the GEF activity of eIF2B</i>	<i>14</i>
DISCUSSION.....	16
<i>How does ISRIB modulate eIF2B?</i>	<i>17</i>
<i>Importance of eIF2-mediated translational control in disease</i>	<i>21</i>
MATERIALS AND METHODS	36
ACKNOWLEDGEMENTS.....	62
REFERENCES	63

CHAPTER 2

STRUCTURE OF THE NUCLEOTIDE EXCHANGE FACTOR EIF2B REVEALS MECHANISM OF MEMORY-ENHANCING MOLECULE 72

ABSTRACT	74
----------------	----

INTRODUCTION	75
RESULTS	78
<i>ISRIB stabilizes decameric eIF2B, accelerating GEF activity</i>	78
<i>ISRIB binds in a deep cleft, bridging the two-fold symmetric interface of the eIF2B decamer</i>	80
<i>Structural model predicts the activity of modified compounds and mutations</i>	82
<i>ISRIB induces dimerization of tetrameric eIF2B subcomplexes</i>	83
<i>Loss and gain-of-function dimerization mutants resist or bypass the effects of ISRIB</i>	85
DISCUSSION.....	87
MATERIALS AND METHODS	110
ACKNOWLEDGEMENTS	135
REFERENCES	137

APPENDIX A

PHARMACOKINETICS OF ISRIB 1.5	143
--	------------

LIST OF FIGURES

CHAPTER 1

Figure 1-1	<i>Knockdown of eIF2B subunits renders cells more resistant to ISRIB</i>	24
Figure 1-2	<i>SAR analyses suggest ISRIB interacts with a two-fold symmetric target</i>	26
Figure 1-2-S1	<i>EC50 of ISRIB analogs</i>	27
Figure 1-3	<i>ISRIB induces dimerization of eIF2B in cells</i>	29
Figure 1-3-S1	<i>ISRIB A1 & A18 structures</i>	31
Figure 1-3-S2	<i>Analysis of the gradients subjected to mass spectrometric analysis</i>	32
Figure 1-4	<i>ISRIB enhances the thermo-stability of the regulatory subunit of eIF2B</i>	33
Figure 1-5	<i>ISRIB enhances the GEF activity of eIF2B in vitro</i>	34
Figure 1-5-S1	<i>Purified human eIF2 and rabbit reticulocyte eIF2B</i>	35

CHAPTER 2

Figure 2-1	<i>ISRIB stabilizes decameric eIF2B, accelerating GEF activity</i>	89
Figure 2-2	<i>Atomic resolution reconstruction of ISRIB-bound eIF2B</i>	91
Figure 2-3	<i>eIF2B structure predicts activity of ISRIB analogs</i>	92
Figure 2-4	<i>ISRIB induces dimerization of tetrameric eIF2B subcomplexes</i>	94
Figure 2-5	<i>Loss & gain-of-function mutants resist or bypass the effects of ISRIB</i>	95
Figure 2-6	<i>Model for ISRIB's mechanism of action</i>	97
Figure 2-S1	<i>Purification and characterization of decameric eIF2B</i>	98
Figure 2-S2	<i>Purification of substrate eIF2 and implementation of GDP exchange assay</i>	99
Figure 2-S3	<i>Cryo-EM local resolution</i>	100
Figure 2-S4	<i>Particle orientation distribution and resolution determination</i>	101

Figure 2-S5	<i>Symmetry and multiple conformer interpretation of the ligand density</i>	102
Figure 2-S6	<i>ISRIB binding environment and key mutants</i>	103
Figure 2-S7	<i>Characterization of ISRIB-A19 enantiomers A19(R,R) and A19(S,S)</i>	104
Figure 2-S8	<i>Characterization of βH188 mutations by sedimentation velocity</i>	105
Figure 2-S9	<i>eIF2B($\beta\gamma\delta\epsilon$) mutants enhance ISRIB-mediated dimerization</i>	106

APPENDIX A

Figure A-1	<i>Structures of ISRIB 1.0 and 1.5</i>	146
Figure A-2	<i>Pharmacokinetics summary</i>	147

LIST OF TABLES

CHAPTER 2

Table 2-S1	<i>Data collection paramaters</i>	107
Table 2-S2	<i>Refinement parameters</i>	108
Table 2-S3	<i>Modeling</i>	109

APPENDIX A

Table A1	<i>Dosing route and volume</i>	148
-----------------	--------------------------------------	-----

Chapter 1

Pharmacological dimerization and activation of the exchange factor

eIF2B antagonizes the integrated stress response

**Pharmacological dimerization and activation of the exchange factor
eIF2B antagonizes the integrated stress response**

*Carmela Sidrauski^{1,2}, *Jordan C. Tsai^{1,2}, Martin Kampmann^{2,3}, Brian R. Hearn⁴, Punitha Vedantham⁴, Priyadarshini Jaishankar⁴, Masaaki Sokabe⁵, Aaron Mendez^{1,2}, Billy W. Newton⁶, Edward L. Tang^{6,7}, Erik Verschueren⁶, Jeffrey R. Johnson^{6,7}, Nevan J. Krogan^{6,7}, Christopher S. Fraser⁵, Jonathan S. Weissman^{2,3}, Adam R. Renslo⁴, and Peter Walter^{1,2}

¹ Department of Biochemistry and Biophysics, University of California, San Francisco

² Howard Hughes Medical Institute, University of California, San Francisco

³ Department of Cellular and Molecular Pharmacology, University of California, San Francisco

⁴ Department of Pharmaceutical Chemistry and the Small Molecule Discovery Center, University of California at San Francisco

⁵ Department of Molecular and Cellular Biology, University of California, Davis

⁶ QB3, California Institute for Quantitative Biosciences, University of California, San Francisco

⁷ Gladstone Institutes, San Francisco

* Both authors contributed equally to this work

This work originally appeared in eLife 2015;4:e07314 and is reproduced under a Creative Commons Attribution 4.0 International license (CC BY 4.0)

ABSTRACT

The general translation initiation factor eIF2 is a major translational control point. Multiple signaling pathways in the integrated stress response phosphorylate eIF2 serine-51, inhibiting nucleotide exchange by eIF2B. ISRIB, a potent drug-like small molecule, renders cells insensitive to eIF2 α phosphorylation and enhances cognitive function in rodents by blocking long-term depression. ISRIB was identified in a phenotypic cell-based screen, and its mechanism of action remained unknown. We now report that ISRIB is an activator of eIF2B. Our reporter-based shRNA screen revealed an eIF2B requirement for ISRIB activity. Our results define ISRIB as a symmetric molecule, show ISRIB-mediated stabilization of activated eIF2B dimers, and suggest that eIF2B4 (δ -subunit) contributes to the ISRIB binding site. We also developed new ISRIB analogs, improving its EC₅₀ to 600 pM in cell culture. By modulating eIF2B function, ISRIB promises to be an invaluable tool in proof-of-principle studies aiming to ameliorate cognitive defects resulting from neurodegenerative diseases.

INTRODUCTION

In the integrated stress response (ISR), phosphorylation of the α -subunit of the eukaryotic translation initiation factor eIF2 (eIF2 α -P) at serine-51 acts as a major regulatory step that controls the rate of translation initiation. Four distinct eIF2 α kinases can catalyze phosphorylation at this single residue, each acting in response to different cellular stress conditions: PERK senses accumulation of unfolded polypeptides in the lumen of the endoplasmic reticulum (ER), GCN2 responds to amino acid starvation and UV-light, PKR responds to viral infection, and HRI responds to heme deficiency. Their convergence on the same molecular event leads to a reduction in overall protein synthesis. Concomitant with a decrease in new protein synthesis, preferential translation of a small subset of mRNAs that contain small upstream open reading frames (uORFs) in their 5' untranslated region is induced (Harding et al., 2003; Wek et al., 2006). ISR-translational targets include the well-known mammalian ATF4 (Activating Transcription Factor 4) and CHOP (a pro-apoptotic transcription factor) (Harding et al., 2000; Vattem and Wek, 2004; Palam et al., 2011). ATF4 regulates genes involved in metabolism and nutrient uptake and was shown to have a cytoprotective role upon stress in many cellular contexts (Ye et al., 2010). ATF4 is also a negative regulator of 'memory genes' and its preferential translation in neurites can transmit a neurodegenerative signal in neurons (Chen et al., 2003; Baleriola et al., 2014). ISR activation leads to preferential translation of key regulatory molecules and thus its level and duration of induction must be tightly regulated. Cells ensure that the effects of eIF2 α -P are transient by also activating a negative feedback loop. This is accomplished by GADD34 induction, which encodes the regulatory subunit of the eIF2 α phosphatase (Lee et al., 2009). GADD34 induction leads to a reduction of eIF2 α -P, allowing cells to restore translation (Novoa et al., 2001).

eIF2 is a trimeric complex (comprised of α , β and γ subunits) that binds to both GTP and the initiator methionyl tRNA (Met-tRNA_i) to form a ternary complex (eIF2•GTP•Met-tRNA_i). After engaging the 40S ribosomal subunit at an AUG start codon recognized by Met-tRNA_i, GTP is hydrolyzed by the GTPase activating protein (GAP) eIF5, and the 60S ribosomal subunit joins to form a complete 80S ribosome ready for polypeptide elongation. eIF2•GDP is released, and eIF2 must then be reloaded with GTP to enter another round of ternary complex formation (Hinnebusch and Lorsch, 2012). In addition to being a GAP for eIF2, eIF5 is also a GDP dissociation inhibitor that prevents GDP release from eIF2 (Jennings and Pavitt, 2015). The exchange of GDP with GTP in eIF2 is catalyzed by its dedicated guanine nucleotide exchange factor (GEF) eIF2B, which has the dual function of catalyzing the release of both eIF5 and GDP (Jennings et al., 2013). eIF2B is a complex molecular machine, composed of five different subunits, eIF2B1 through eIF2B5, also called the α , β , γ , δ , and ϵ subunits. eIF2B5 catalyzes the GDP/GTP exchange reaction and, together with a partially homologous subunit eIF2B3, constitutes the ‘catalytic core’ (Williams et al., 2001). The three remaining subunits (eIF2B1, eIF2B2, and eIF2B4) are also highly homologous to one another and form a ‘regulatory sub-complex’ that provides binding sites for eIF2B's substrate eIF2 (Dev et al., 2010). When phosphorylated on Ser-51, eIF2 α -P dissociates more slowly from the eIF2B regulatory sub-complex and locks eIF2B into an inactive state (Krishnamoorthy et al., 2001). Phosphorylation thus renders eIF2 an inhibitor of its own GEF. Because eIF2 is more abundant than eIF2B, a small amount of eIF2 α -P is sufficient to sequester a large proportion of available eIF2B, leading to a substantial reduction in overall protein synthesis.

Using a cell-based high-throughput screen, we recently identified a small molecule, ISRIB (for integrated stress response inhibitor) that renders cells resistant to the inhibitory effects of eIF2 α -P. ISRIB, the only *bona fide* ISR inhibitor identified to date, is a highly potent compound

(EC₅₀ = 5 nM in cells) and has good pharmacokinetic properties (Sidrauski et al., 2013). In agreement with the phenotype of genetically modified mice having reduced eIF2 α -P, we showed that treatment with ISRIB enhances memory consolidation in rodents. Moreover, ISRIB comprehensively and selectively blocked the effects of eIF2 α phosphorylation on mRNA translation and triggered rapid stress granule disassembly (Sidrauski et al., 2015). To date, the molecular target of ISRIB is not known. The fast kinetics of action of ISRIB and the remarkable specificity of its effects in response to eIF2 α phosphorylation strongly suggested that its target is a factor that closely interacts with the eIF2 translation initiation complex. The existence of eIF2B mutations in yeast that, like ISRIB, render cells resistant to eIF2 α -P led us to propose that eIF2B was a likely target of this small molecule (Sidrauski et al., 2013). Here, we draw on clues from two independent approaches, an unbiased genetic screen and structure/activity analyses of ISRIB, to converge on the hypothesis that the mammalian eIF2B complex indeed is the molecular target of ISRIB. We demonstrate that a symmetric ISRIB molecule induces or stabilizes eIF2B dimerization, increasing its GEF activity and desensitizing it to inhibition by eIF2-P. Thus ISRIB directly modulates the central regulator in the ISR.

RESULTS

Knockdown of eIF2B renders cells resistant to ISRIB

To identify the molecular target of ISRIB, we conducted a genetic screen for genes whose knockdown modulated the sensitivity of cells to the drug. Using this strategy, we were previously able to pinpoint the molecular targets of cytotoxic compounds and to delineate their mechanism of action (Matheny et al., 2013; Julien et al., 2014). Here, we conducted a reporter-based screen using a sub-library of our next-generation shRNA library targeting 2933 genes involved in aspects of proteostasis. This focused library targets each protein-coding gene with ~25 independent shRNAs and contains a large set (>1000) of negative-control shRNAs. We have previously shown that the use of such libraries and analysis using a rigorous statistical framework generates robust results from forward genetic screens (Bassik et al., 2013; Kampmann et al., 2013). We screened the shRNA library in a K562 cell line expressing an uORF-ATF4-venus reporter (Figure 1-1A), similar to the translational reporters that we and others previously used to measure activation of the ISR. In cells bearing this reporter, the venus fluorescent protein is translationally induced upon eIF2 α phosphorylation. We chose the K562 cell line for the screen because these cells are non-adherent and allow for efficient fluorescence-activated cell sorting (FACS). Treatment with thapsigargin (Tg), an ER stress inducer that inhibits the ER-localized Ca²⁺-ATPase, resulted in a sixfold increase in mean fluorescence intensity and, as expected, ISRIB substantially reduced induction of the reporter (Figure 1-1B). As a first step in the screen, we transduced the reporter cell line with the library and selected shRNA-expressing cells. We next divided the population and induced ER stress with Tg in the presence or absence of ISRIB. To optimize the dynamic range of the screen and to focus on early translational effects elicited by eIF2 α phosphorylation, we incubated cells for 7 hr, at which time full induction of the reporter was reached. To identify genes

whose knockdown resulted in either enhanced or reduced sensitivity to ISRIB, we used a concentration of drug corresponding to the EC₅₀ (15 nM) in this cell type. Cells from each subpopulation (Tg-treated and Tg + ISRIB-treated) were then FACS-sorted to isolate the third of the population with the lowest reporter expression and the third of the population with the highest reporter expression (see schematic in Figure 1-1C). To quantify frequencies of cells expressing each shRNA, we isolated genomic DNA from the sorted populations and then PCR-amplified, purified and analyzed by deep-sequencing the shRNA-encoding cassettes. To determine the enrichment or depletion of each shRNA, we compared its frequency in the Low and High reporter populations. For each gene, we calculated a p value by comparing the distribution of log₂ enrichment for the 25 shRNAs targeting the gene to the negative control shRNAs. We then plotted p values for each gene determined in ER stress-induced cells in the absence (x-axis) vs the presence (y-axis) of ISRIB (Figure 1-1D).

The data shown in Figure 1-1D revealed that knockdown of the majority of the genes in the library did not change the expression of the reporter upon either treatment and thus congregated in the center of the plot. By contrast, knockdown of genes that changed the expression of the reporter to the same degree in both treatments localized to the diagonal. We focused our analysis on genes that when knocked-down in the presence of ISRIB, affected the expression of the reporter selectively. In this plot these genes are displaced along the y-axis and encode proteins whose reduced expression modulates the cells' sensitivity to ISRIB. Knockdown of genes that confer resistance to ISRIB lie above the diagonal, while knockdown of genes that confer hypersensitivity to ISRIB lie below it.

Of particular interest was the pronounced effect of the knockdown of (i) two subunits of eIF2B, eIF2B4 and eIF2B5, that significantly reduced the sensitivity ($p < 1.4 \cdot 10^{-6}$ and $p <$

2.4·10⁻¹¹, respectively) and (ii) eIF4G1 that significantly enhanced the sensitivity ($p < 3.4 \cdot 10^{-10}$) of cells to ISRIB, each without affecting induction of the reporter (i.e., no displacement along the x-axis). Individual shRNAs targeting either eIF2B4 or eIF2B5 were enriched in the High reporter population of the ISRIB-treated sample and stood out from the negative control shRNA population (Figure 1-1E). Knockdown of other translation initiation factors (highlighted in Figure 1-1D) revealed no effects on ISRIB sensitivity (locating close to the diagonal of the plot). Based on these data and the fact that eIF2 α -P is a direct inhibitor of eIF2B, we postulated that eIF2B is a promising candidate target of ISRIB. Moreover, the data suggest that ISRIB acts as an activator of eIF2B: when eIF2B levels are reduced, cells become resistant to the effects of ISRIB when there is a lower supply of molecules that can be activated.

Structure-activity relationship of ISRIB suggests a twofold symmetric target

Structure-activity studies of synthetic ISRIB analogs provided further clues as to the nature of its molecular target in cells. Of particular note is that the progenitor member of this class (ISRIB, also denoted herein as ISRIB-A1, Figure 1-2A) exhibits twofold rotational symmetry and is bisected longitudinally by a mirror plane. The molecule is thus achiral but can exist as either *cis* or *trans* diastereomers, depending on the relative orientation of the side chains at positions 1 and 4 of the cyclohexane ring (Figure 1-2A, ISRIB-A1 and ISRIB-A2). We previously showed in cell-based assays that the *trans*-isomer (ISRIB-A1, EC₅₀ = 5 nM) is > 100-fold more potent than the *cis*-isomer (ISRIB-A2, EC₅₀ > 600 nM). This indicated a preference for an extended binding conformation, with both side chains adopting an equatorial position, as would be expected in the preferred chair conformation of the *trans* diastereomer (ISRIB-A1) (Sidrauski et al., 2013). By contrast, the *cis* diastereomer ISRIB-A2 would need to adopt a higher-energy

boat-like conformation to project both side chains in pseudo-equatorial orientations. Further structure-activity studies revealed that a 1,4-phenyl spacer could reasonably substitute for 1,4-cyclohexyl, although a 10-fold loss in potency was observed (ISRIB-A7, $EC_{50} = 53$ nM). Replacement of the 1,4-cyclohexyl ring with *cis* or *trans*-1,3-cyclobutyl spacers resulted in a more dramatic loss of potency (ISRIB-A4, $EC_{50} = 142$ nM; ISRIB-A5, $EC_{50} = 1000$ nM), indicating that the distance between the distal aromatic rings in ISRIB analogs is as important as their positioning in space. This distance dependence was also observed in analogs with acyclic spacers (e.g., ISRIB-A3 and ISRIB-A6). Thus, the *n*-butyl linker in ISRIB-A3 (maintaining the spacing of ISRIB-A1) was better tolerated than the shorter *n*-propyl linker in ISRIB-A6, an analog without measurable activity. The 60-fold reduction in the potency of ISRIB-A3 as compared to ISRIB-A1 can be explained by the increased flexibility of the *n*-butyl chain, resulting in a higher entropic cost associated with adopting the conformation required for binding.

Extensive structure-activity relationship (SAR) studies were also carried out on the distal aryl substituents. Overall, we found that the SAR was consistent with the idea that ISRIB analogs bind across a symmetrical interface. Thus, sequential modification of one and then both side chains in ISRIB analogs was additive, both for favorable modifications and for unfavorable modifications. For example, a *para*-chloro substituent was found to be optimal in ISRIB analogs. Replacing one or both *para*-chloro substituents with fluoro, methyl, or cyano groups led to predictable deterioration of potencies, with the doubly modified analogs least potent in every case (Figure 1-2B, compare ISRIB-A8 with A9, ISRIB-A10 with A11 and ISRIB-A12 with A13). Conversely, the addition of a *meta*-chloro or *meta*-fluoro substituent enhanced the potency of ISRIB analogs, and introducing such modifications on both side chains produced the most potent analogs (Figure 1-2C, compare ISRIB-A14 with A15, ISRIB-A16 with A17). Among these more potent analogs

is ISRIB-A17, which is nearly 10-fold more potent than ISRIB-A1, lowering the EC₅₀ into the picomolar range. A full account of our SAR studies will be provided elsewhere but the data presented here demonstrate that the electronics of the phenoxy substituents are important drivers of potency and support the notion that the two halves of ISRIB analogs are engaged in similar recognition events with the target. The most plausible explanation of these findings is that the functional twofold symmetry of ISRIB reflect a target that is likewise twofold symmetric. Taken together, the results obtained by the shRNA screen described above and the recent discovery of eIF2B dimers suggest that ISRIB may act by directly binding to eIF2B at a twofold symmetric interface that stabilizes it as a dimer (Gordiyenko et al., 2014; Wortham et al., 2014).

ISRIB promotes dimerization of eIF2B in cells

To test directly whether ISRIB induces or stabilizes the dimeric form of eIF2B, we treated cells with or without ISRIB. We prepared extracts in a high-salt buffer to dissociate eIF2B from its substrate eIF2 and analyzed the lysates by velocity sedimentation on sucrose gradients. In the absence of ISRIB, eIF2B (as detected by immunoblotting with antibodies against eIF2B4 and eIF2B5) migrated predominantly in fractions 3–6 in the gradient, consistent a combined molecular mass of four of its subunits (225 kDa). In the high-salt buffer used, the eIF2B complex lacked the eIF2B1 subunit, which was found predominantly in fractions 1–3 of the gradient. By contrast, when cells were treated with ISRIB, we observed a substantial shift in sedimentation towards a higher molecular mass (predominantly found in fractions 5–8), demonstrating a substantial increase in complex size. By comparing the relative mobility of eIF2B4 and eIF2B5 to that of a background band (marked with a red asterisk in the upper panel of Figure 1-3), the shift in size of eIF2B is easily appreciated. The magnitude of the shift is consistent with a doubling in the

molecular mass of the complex. Interestingly, in extracts from ISRIB-treated cells, eIF2B1 also shifted to the heavier fractions, suggesting that its association with the rest of the complex was stabilized. In contrast to the eIF2B subunits, we did not observe a shift in eIF3a or eIF2 α . These data strongly support the notion that ISRIB induces the formation of a stable eIF2B dimer.

To determine if eIF2B's ostensible increase in molecular mass was due to dimerization of a complete eIF2B complex, we used mass spectrometry to validate the shift of all of its five subunits. To this end, we treated cells with ISRIB or with an inactive analog ('ISRIB^{inact}' [ISRIB-A18], Figure 1-3-S1) and subjected extracts to fractionation on sucrose gradients. We used ISRIB^{inact} to control for non-specific hydrophobic interactions of ISRIB with proteins in the extract. We determined the complete protein composition in the fractions in which eIF2B peaked in the presence of ISRIB (fractions 6–9, Figure 1-3-S2) by mass spectrometry. This analysis revealed a significant ISRIB-dependent enrichment of all five eIF2B subunits (Figure 1-3B). Notably, eIF2B subunits in ISRIB samples exhibited a characteristic profile in which all subunits collectively peaked in fraction 7. By contrast eIF2B subunits in ISRIB^{inact} samples were most abundant in fraction 6 and trailed further into the gradient. As expected, two other large protein complexes, the proteasome (Figure 1-3B; data shown for subunit PSMD1) and eIF3 (Figure 1-3B; data shown for subunit eIF3A), showed no displacement upon ISRIB treatment.

Because the mass spectrometric analysis of the gradient was performed with a non-targeted method, it allowed us to ask whether additional proteins would associate with eIF2B potentially contributing to the shift in size. To address this question, we correlated the intensity profiles of all other proteins identified through the analyzed fractions to the sedimentation profile exhibited by a representative subunit, eIF2B4. We plotted the correlation coefficient (R-value) for each comparison. We were excited to find that all eIF2B subunits (eIF2B1, eIF2B2, eIF2B3, eIF2B5)

stood out as most strongly correlated to eIF2B4, all exhibiting correlation coefficients (R-values) > 0.98 (Figure 1-3C), strongly indicating that the increase in molecular mass of eIF2B upon ISRIB addition indeed resulted from eIF2B dimerization. Moreover, these analyses strongly support the notion that eIF2B forms a complete complex upon ISRIB treatment.

ISRIB enhances the thermo-stability of eIF2B4

To identify the subunit of eIF2B targeted by ISRIB, we monitored drug-target engagement, utilizing a cellular extract thermal shift assay (CETSA) (Martinez Molina et al., 2013). This method relies on the principle that ligand binding can stabilize protein folding and hence increase the protein's resistance to heat denaturation. To this end, we incubated a cell lysate with and without ISRIB and then heated aliquots to different temperatures, followed by centrifugation to separate soluble from precipitated denatured proteins. We then analyzed the soluble fractions by Western blotting with antibodies against eIF2B1, eIF2B4 and eIF2B5. When the lysate was pre-incubated with ISRIB, we observed an increase in thermal stability of eIF2B4 (Figure 1-4, lanes 4 and 5, arrows). Although slight, the increase was highly reproducible and, as was the case for the analysis of the eIF2B shift in the sucrose gradients shown in Figure 1-3, a background band that cross-reacts with the anti-eIF2B4 antibody (red asterisk) provided a convenient internal control for the exclusive stabilization of eIF2B4. By contrast, no ISRIB-dependent increase in thermal stability was observed with the two other eIF2B subunits analyzed (eIF2B1 and eIF2B5), or with the translation initiation factors eIF2 α or eIF3a (Figure 1-4). This analysis suggests that eIF2B subunits act autonomously in this assay, as eIF2B4 was stabilized while other subunits denatured and precipitated. We conclude that ISRIB binds eIF2B4 eliciting this stabilization.

ISRIB enhances the GEF activity of eIF2B

To explore the functional consequences of ISRIB binding on eIF2B's GEF activity, we directly tested its effect on the rate of GDP release from eIF2. To this end, we pre-loaded purified eIF2 with radioactive GDP ($[^3\text{H}]\text{-GDP}$) and measured the fraction that remained bound as a function of time in the presence of an excess of unlabeled GDP. As expected, the intrinsic rate of nucleotide release was slow; after 20 min of incubation, only 20% of $[^3\text{H}]\text{-GDP}$ dissociated from the eIF2 complex (Figure 1-5A, black dashed line). The intrinsic rate of GDP release was not affected by the addition of ISRIB (Figure 1-5A, red dashed line). Upon addition of eIF2B, we observed a significant increase in the rate of GDP release ($t_{1/2} = 3.2$ min), leading to an 80% release after 10 min (Figure 1-5A, solid black line). Excitingly, GDP release was threefold faster upon addition of ISRIB ($t_{1/2} = 1.1$ min) (Figure 1-5A, solid red line).

We next tested the behavior of phosphorylated eIF2 (eIF2-P) in these assays. To this end, we generated eIF2-P by incubating eIF2 with recombinantly expressed PERK kinase and ATP. We next loaded eIF2-P with $[^3\text{H}]\text{-GDP}$ and measured GDP release. As expected from the known inhibitory role of eIF2 α phosphorylation on eIF2B, GDP release from eIF2-P remained virtually unchanged in the presence of eIF2B (Figure 1-5B, black solid line). We next asked whether ISRIB allows eIF2-P to be a substrate for eIF2B. Our data show that ISRIB did not stimulate GDP release from eIF2-P (Figure 1-5B, red solid line), indicating that this is not the case. We next explored whether ISRIB can overcome the inhibitory effects of eIF2-P on eIF2B. To this end, we tested if ISRIB can promote GDP release from unphosphorylated eIF2 in the presence eIF2-P by mixing $[^3\text{H}]\text{-GDP}$ -loaded eIF2 with eIF2-P in a 3:1 or 1:1 ratio. Although the exchange reaction was slower, ISRIB stimulated GDP release at the eIF2:eIF2-P ratio of 3:1 (-ISRIB: $t_{1/2} = 6.7$ min, vs +ISRIB: $t_{1/2} = 2.7$ min) (Figure 1-5C), whereas we observed hardly any stimulation at the 1:1 ratio

(-ISRIB: $t_{1/2} = 6.4$ min, vs + ISRIB: $t_{1/2} = 5.3$ min) (Figure 1-5D). Thus, the relative ratio of substrate (eIF2) to inhibitor (eIF2-P) emerges as an important parameter affecting ISRIB's ability to modulate eIF2B activity. Taken together, these functional data underscore the notion that ISRIB acts as an activator of eIF2B and that ISRIB alleviates inhibition by eIF2-P, as long as eIF2-P is present below threshold levels.

DISCUSSION

The ISR is controlled by phosphorylation of the general eukaryotic translation initiation factor eIF2. Multiple cell signaling pathways converge at a single phosphorylation site on its α -subunit where phosphorylation of Ser-51 modulates eIF2 α 's interaction with its dedicated, multi-subunit guanine nucleotide-exchange factor (GEF) eIF2B. We previously identified and characterized a potent small molecule ISR inhibitor (ISRIB) with good pharmacological properties and showed that it renders cells insensitive to eIF2 α phosphorylation upon ISR induction and enhances cognitive function in rodents (Sidrauski et al., 2013). Within a few minutes after administration, ISRIB reverses the effects triggered by eIF2 α phosphorylation dissolving RNA stress granules and restoring translation of inhibited mRNAs while reversing de-repression of uORF-containing mRNAs (Sidrauski et al., 2015). Because ISRIB was identified in a phenotypic cell-based screen, its mechanism of action remained obscure. Here, we report the identification of eIF2B as the molecular target of ISRIB. To this end, we used reporter-based shRNA screening, structure–function analyses of ISRIB analogs, biochemical characterization of eIF2B oligomerization and thermal stability, and enzymatic analyses of eIF2B's GEF activity. The results of our multipronged approach provide a rationale for why ISRIB analogs exhibit twofold symmetry, showed ISRIB-mediated stabilization and activation of eIF2B dimers, and suggested eIF2B δ , also known as its δ -subunit, as a candidate to contain the ISRIB binding site. In the course of this work, we also developed more active ISRIB analogs, improving potency by almost 10-fold and lowering EC₅₀ values into the high picomolar range in cell culture.

How does ISRIB modulate eIF2B?

In this work, ISRIB emerged as an eIF2B activator. First, ISRIB promoted the formation of or stabilized eIF2B dimers ('[eIF2B]₂') and enhanced GEF activity in biochemical assays. Second, knockdown of both eIF2B4 and eIF2B5 subunits rendered cells resistant to the action of ISRIB, presumably because under these conditions the total amount of eIF2B that can be activated in cells is reduced. Note that the three other subunits of eIF2B were not represented in our focused shRNA library and therefore could not have been identified in the screen. Functioning as an activator, ISRIB joins the still sparsely populated group of unnatural small molecule enzyme activators, while the vast majority of synthetic small molecules that modulate enzyme activity are inhibitors (Wiseman et al., 2010; Zorn and Wells, 2010; Wang et al., 2014). Conversely, knockdown of eIF4G1 sensitized cells to ISRIB. This can be explained because, under conditions of reduced eIF4G1, overall cap-dependent translation initiation is reduced. A lower concentration of ISRIB could then suffice to generate sufficient amounts of GTP-loaded eIF2 to maintain normal rates of translation, even in the presence of eIF2 α -P. Intriguingly, knockdown of other components of the cap-binding complex, such as eIF4A1, or components of the eIF3 complex, such as eIF3f and eIF3b, not only reduced sensitivity to ISRIB but also affected induction of the reporter upon ER stress alone. In agreement with studies in yeast and plants (Szamecz et al., 2008; Roy et al., 2010), knockdown of the eIF3 subunits in the library (eIF3a, eIF3b, and eIF3f) reduced translational induction of the reporter, presumably due to eIF3's stimulatory effects on re-initiation after translation of short uORFs. Our data therefore provide the first evidence that the mechanism of re-initiation may be similar in mammalian cells.

The differences observed between assorted initiation factors on reporter expression is likely to reflect the extent to which translation initiation was reduced under the different knockdown

conditions. Importantly however, only knockdown of the eIF2B subunits targeted by shRNAs in the library conferred resistance to ISRIB.

We previously proposed two models that could explain how ISRIB renders cells resistant to the inhibitory effects of eIF2 α -P (Sidrauski et al., 2013). First, ISRIB could weaken the effect of eIF2 α -P on eIF2B by interfering with its tight and non-productive binding. In this way, more eIF2B would be available to reload eIF2 with GTP. Second, ISRIB could enhance the basal activity of eIF2B so that the fraction not engaged with eIF2 α -P would produce sufficient levels of ternary complex to sustain translation in cells. Currently, our in vitro enzymatic data do not allow us to distinguish between these models. While we showed that the rate of GDP release from purified eIF2 by eIF2B was significantly enhanced upon addition of ISRIB (and therefore can explain the effect of ISRIB in living cells), we do not know what fraction of our eIF2 preparation was isolated in a eIF2 α (Ser-51)-phosphorylated state. ISRIB could thus either increase the GEF activity of eIF2B on eIF2 or diminish the inhibitory effect of a small amount eIF2-P present in the assay, akin to the regime that we directly tested by adding increasing amounts of in vitro phosphorylated eIF2 to the assay. Our analyses confirmed however that eIF2 α -P is not a substrate for eIF2B (in agreement with previous reports [Kimball et al., 1998]), and determined that ISRIB does not enable eIF2B to use eIF2-P as a substrate.

While catalyzing guanine nucleotide exchange on other GTPases can be effected by relatively simple enzymes, eIF2B is a complex molecular machine composed of five different subunits. Much remains uncertain about the structural arrangement of the subunits and how eIF2B's activity is regulated (Jennings and Pavitt, 2014). Similarly, how ISRIB exerts its effects on eIF2B remains unknown. eIF2B subunits are organized into two modules, called the catalytic (eIF2B3 and eIF2B5) and regulatory (eIF2B1, eIF2B2 and eIF2B4) sub-complexes, containing

two and three homologous proteins, respectively. The subunits of the regulatory subcomplex are characterized by highly homologous Rossman folds that bind nucleotides and are adorned by N-terminal extensions of lesser homology between the subunits. Intriguingly, recombinantly expressed eIF2B1 purified and crystallized as a stable homodimer, with an extensive buried interface contributed by the nucleotide-binding domains (Bogorad et al., 2014). The residues contributing to the interface are highly conserved among its homologs in the complex. Combined with the SAR analyses indicating ISRIB's obligate twofold symmetry, the discovery that (eIF2B)₂ exist in both yeast and mammalian cells was instrumental in suggesting to us that eIF2B is the target of ISRIB (Gordiyenko et al., 2014; Wortham et al., 2014). According to this model, ISRIB binds to two regulatory eIF2B subunits that form part of the interface linking two pentamers. Native mass spectrometry of mammalian eIF2B revealed the existence of stable subcomplexes that lack the eIF2B1 subunit, indicating that this subunit is more loosely associated, as we confirmed here by sedimentation of the non-ISRIB treated control extracts (Wortham et al., 2014). We have shown by biochemical analysis that ISRIB binding stabilizes (eIF2B)₂, rendering it resistant to dissociation of eIF2B1 in the high-salt buffers used in the sucrose gradient analysis. Importantly, we showed by mass spectrometric proteomic analysis that no other protein co-profiled with (eIF2B)₂ in the gradients, demonstrating that the observed ISRIB-dependent effects were confined exclusively to eIF2B subunits.

Given the relative stability of the eIF2B1 homodimer ($K_d < 1$ nM; [Bogorad et al., 2014]) and our observation that ISRIB stabilized complete (eIF2B)₂, it is likely that two opposing eIF2B1 subunits form an essential part of the interface that links two eIF2B pentamers. ISRIB could favor this interaction by adding to the affinity provided by a (eIF2B1)₂ tether via the stabilization of an additional interface formed between homologous regions of two eIF2B4 subunits. This view would

be in agreement with our data that showed protection by ISRIB of eIF2B4 to thermal denaturation. For symmetry reasons, as elegantly discussed in (Bogorad et al., 2014), this arrangement would leave the interfaces of the two identical eIF2B2 subunits in the complex unpaired. Alternatively, ISRIB may stabilize interfaces between eIF2B4 in one eIF2B pentamer and eIF2B2 in an opposing pentamer. If this were the case, ISRIB would bind at a pseudo-symmetric interface formed by two different, yet strongly homologous components. We note in this scenario, two ISRIB molecules binding to two identical interfaces of opposite polarity ($eIF2B2 \rightarrow eIF2B4$ and $eIF2B4 \rightarrow eIF2B2$) may bind and stabilize one $(eIF2B)_2$, which may contribute to its potency. This would open the possibility that design and synthesis of non-symmetric analogs could further improve ISRIB's efficacy. A definite assignment of ISRIB's binding site will have to await the structural determination of ISRIB-bound $(eIF2B)_2$ or genetic analyses in which loss-of-function mutations are suppressed by compensating changes in ISRIB analogs.

Consistent with the notion that the regulatory sub-complex provides binding sites for eIF2, mutations in eIF2B in yeast that render cells resistant to phosphorylation of eIF2 α map to eIF2B1 and eIF2B4 (Pavitt et al., 1997). Moreover, two different variants in mammalian eIF2B4 (generated by alternative splicing) contain different N-terminal extension domains and exclusive expression of the longer variant desensitizes cells to eIF2 α phosphorylation (Martin et al., 2010), phenocopying the effects elicited by ISRIB in mammalian cells. In the structure of $(eIF2B1)_2$ the N-terminal domains reach across the interface and interact with the nucleotide binding domain of the partnering eIF2B1 molecule. We speculate that the extended N-terminal domain of eIF2B4 may stabilize $(eIF2B)_2$, mimicking the effects of ISRIB.

Importance of eIF2-mediated translational control in disease

Phosphorylation of eIF2 is important in long-term depression (LTD), and we have recently shown that this modulation of synaptic plasticity can explain cognitive enhancement elicited by ISRIB treatment of wild type rodents (Di Prisco et al., 2014). Engagement of metabotropic glutamate receptors (mGluR) in post-synaptic hippocampal cells leads to eIF2 phosphorylation and preferential translation of neuronally expressed oligophrenin-1 (encoded by OPHN1), a protein that mediates the initial steps of downregulation of postsynaptic AMPA receptors by endocytosis (Nadif Kasri et al., 2011). Like ATF4, the 5'-UTR of OPHN1 mRNA contains two uORFs that repress expression of the downstream coding sequence unless eIF2 is phosphorylated. Importantly, both genetic ablation of eIF2 phosphorylation and treatment with ISRIB but not the inactive analog ISRIB-A18 abolished the reduction in surface AMPARs and blocked mGluR-LTD (Di Prisco et al., 2014). These findings hold promise that targeting the effects of phosphorylation of eIF2 by pharmacologically modulating eIF2B with drugs such as ISRIB could result in therapies for cognitive disorders. Activation of the ISR with its characteristic increase in eIF2 phosphorylation has been reported in numerous neurodegenerative diseases, including Alzheimer's disease, Parkinson's disease, Frontotemporal Dementia, Amyotrophic Lateral Sclerosis, and prion neurodegenerative diseases, but its role in disease progression has just recently begun to be interrogated (Kim et al., 2013; Leitman et al., 2014; Ma et al., 2013; Moreno et al., 2013, 2012). The importance of eIF2 and eIF2B in brain function is underscored by the existence of mutations in these factors that cause human disease. A familial intellectual disability syndrome was mapped to a mutation in the γ subunit of eIF2 (encoded by EIF2S3). When an analogous mutation was introduced into yeast cells, it impaired eIF2-mediated translation initiation (Borck et al., 2012). Mutations in the different subunits of eIF2B cause childhood ataxia with central nervous system

(CNS) hypomyelination (CACH) or vanishing white matter disease (VWMD). All affected individuals have two altered copies of a single eIF2B gene (autosomal recessive inheritance) and the majority are missense mutations that cause a single amino acid change while the remainder is a mixture of premature nonsense mutations, some causing a frame-shift and others altered splicing. All subunits of eIF2B are essential and the biochemical analysis of 40 different VWMD mutations revealed that the majority are hypomorphs, that is, cause partial loss-of function of eIF2B GEF activity (Leegwater et al., 2001; Li et al., 2004; Fogli and Boespflug-Tanguy, 2006). Whether ISRIB can reverse the deleterious effects of mutations in eIF2B in VWMD patients is not known, but we speculate that it may protect from a further reduction in GEF activity by stress-induced eIF2 α -P. Intriguingly, the onset of VWMD is varied but generally exacerbated by head trauma and febrile illnesses. Interestingly, two VWMD mutations have been characterized that affect the integrity and dimerization of the eIF2B complex. A mutation in eIF2B1(V183F) maps to the dimerization interface and the mutant recombinant protein is predominantly in the monomeric form and a mutation in eIF2B4(A391D) affects complex integrity in the absence of eIF2B1 and dimerization (Wortham et al., 2014). ISRIB induces dimerization and complex stability and thus may rescue the effects of such mutations.

Given the wide spectrum of potential applications for ISRIB in neurological diseases, the identification of its molecular target is an important step. Having established a proof-of-principle that eIF2B can be pharmacologically modulated, now enables directed screening efforts to identify new series of compounds and thereby enhance the probability of developing clinically useful pharmaceuticals that address currently unmet needs.

Note added at proof

While this work was under review, Sekine et al. reported the independent identification of eIF2B as the molecular target of ISRIB (Sekine et al., 2015).

Figure 1-1

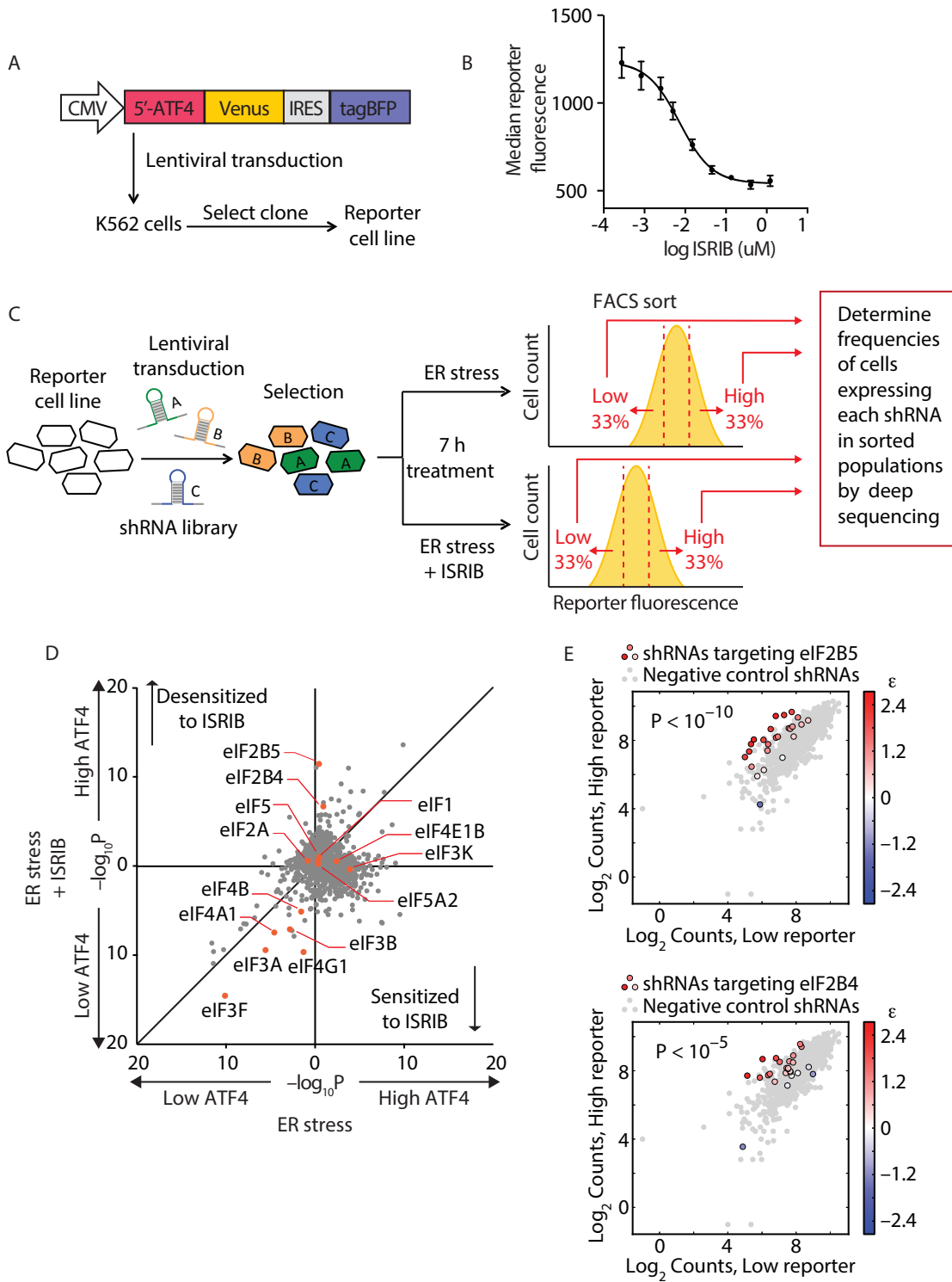
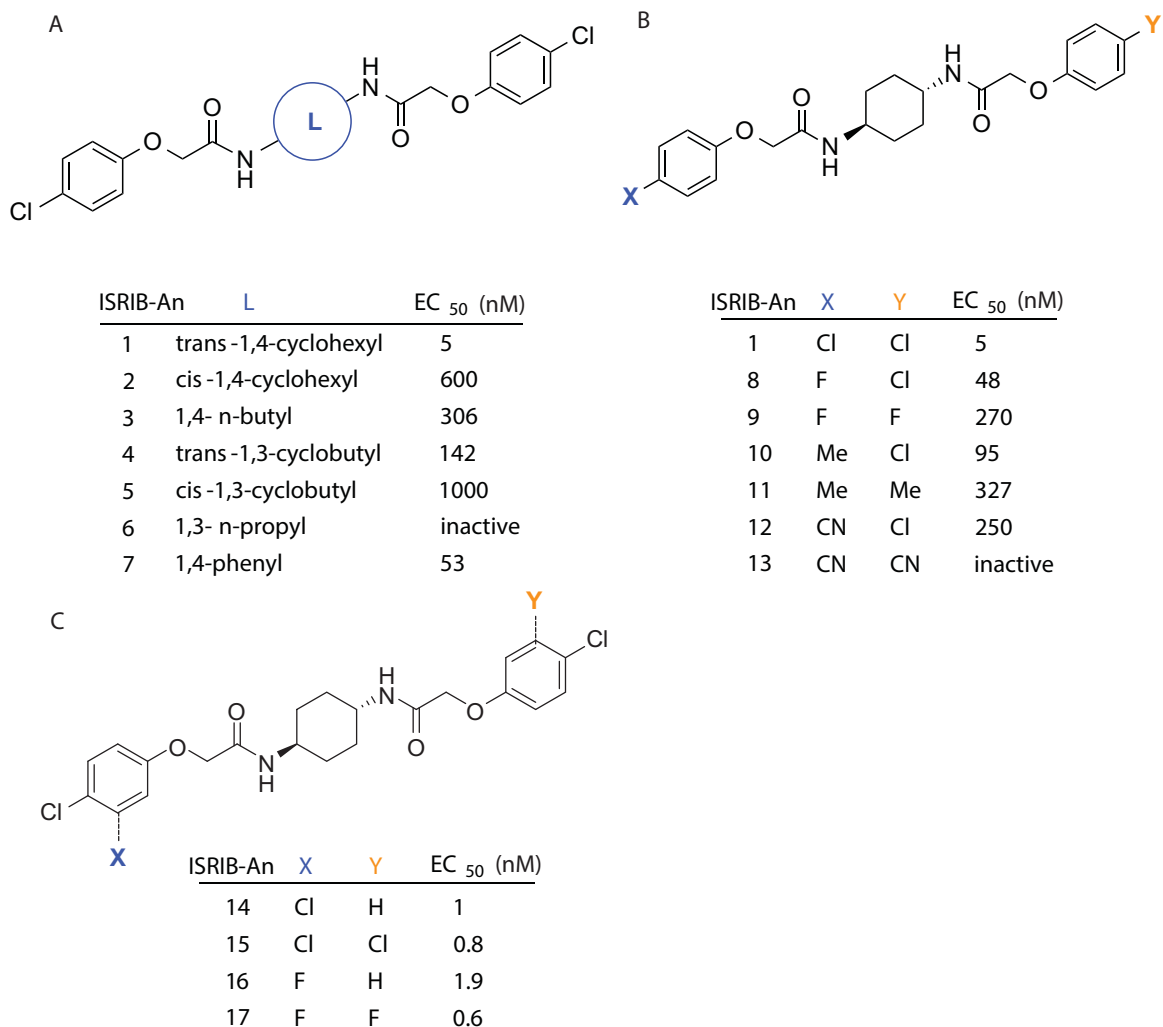


Figure 1-1

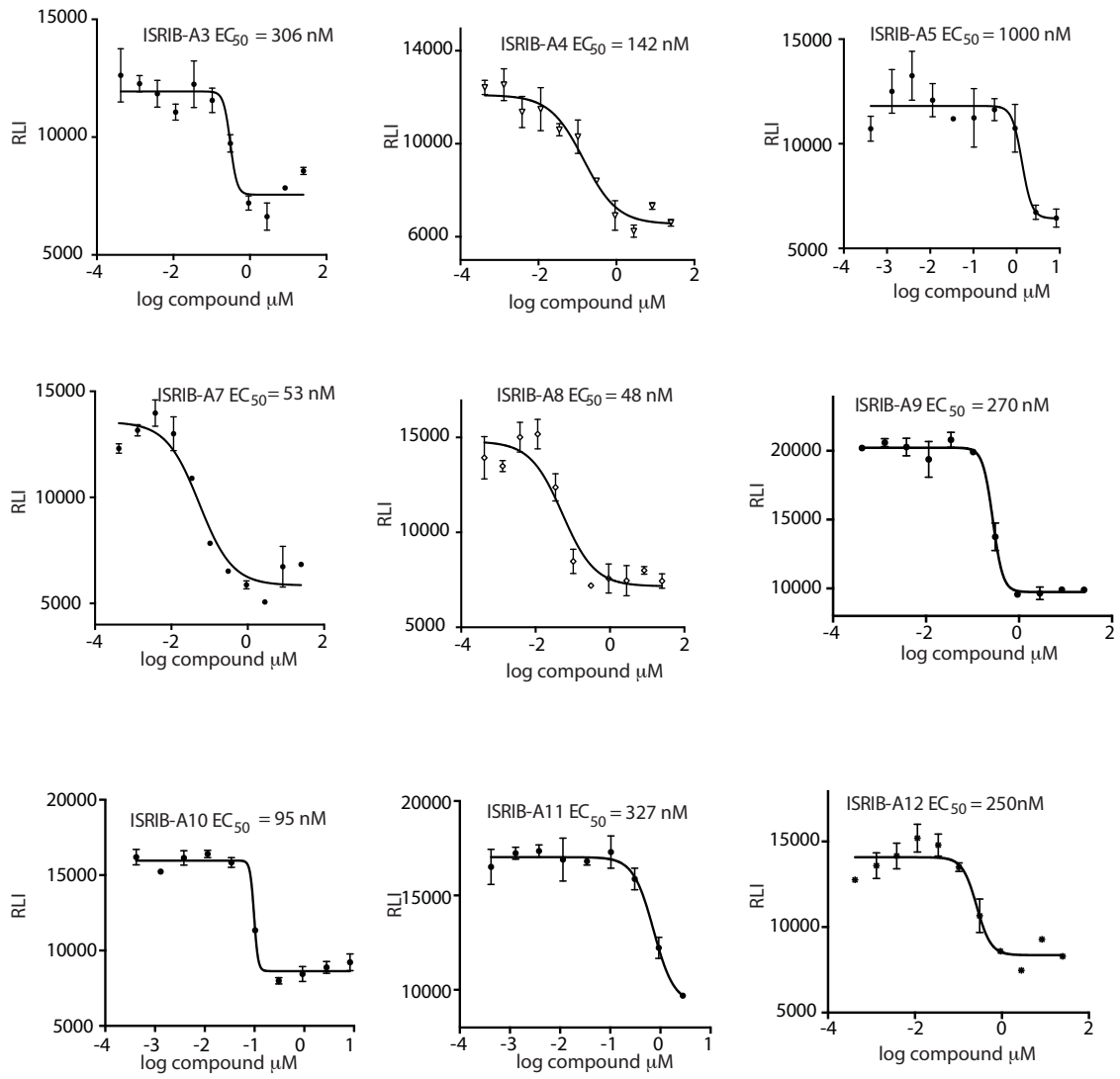
Knockdown of eIF2B subunits renders cells more resistant to ISRIB: (A) Schematic representation of the ATF4-venus reporter used for the screen. The 5' end of the human ATF4 mRNA up to the start codon of the ATF4-encoding ORF was fused to venus, followed by the EMCV internal ribosomal entry site (IRES) and BFP and inserted into a lentiviral system. (B) ISRIB reduces activation of the ATF4-venus reporter. K562 cells were incubated with Tg (300 nM) for 6 h in the presence of different concentrations of ISRIB. Reporter fluorescence was measured by flow cytometry and median values were plotted (N = 3, +/- SD). (C) Schematic of the shRNA screen aimed to identify the target ISRIB. K562 cells expressing the screening reporter were transduced with a pooled shRNA library and transduced cells were selected. The population was then divided into two and either treated with Tg (ER stress) or Tg + ISRIB (ER stress + ISRIB) for 7h. Cells were sorted based on their fluorescence (venus) intensity into three bins and the third of the population with the Low and High-reporter levels were collected. Note that the ER stress + ISRIB population had a lower overall fluorescence intensity (median) as ISRIB partially blocks induction of the reporter when added at a concentration corresponding to its EC50 in these cells (15 nM). DNA was extracted from the sorted subpopulations for each treatment and shRNA-encoding cassettes were PCR-amplified and subjected to deep sequencing to determine their frequency. (D) Effect of knockdown of individual genes in the proteostasis library on reporter expression upon ISR induction in the presence and absence of ISRIB. Gene P values for enrichment and depletion were compared between the ER stress (x-axis) versus the ER stress + ISRIB (y-axis) experiments. For each gene, a P value was calculated by comparing the distribution of log2 enrichment values for the 25 shRNAs targeting the gene to the negative control shRNAs. (E) The log2 counts for eIF2B5 (top panel) or eIF2B4 (bottom panel) targeting shRNAs in the High-reporter population (x-axis) versus the Low-reporter population (y-axis) was plotted and color coded based on the log2 enrichment as depicted in the side bar. Red colors indicate a shift towards higher reporter levels, blue colors shifts towards lower reporter levels. Negative control shRNAs in the library are colored grey.

Figure 1-2



SAR analyses suggest ISRIB interacts with a two-fold symmetric target: (A) ISRIB analogs bearing various linkers (L) between the pendant side chains and their corresponding EC₅₀ values. (B) Sequential replacement of the *para*-chloro substituent (X and Y) with F, Me, or CN on the distal aromatic rings has unfavorable and additive effects on potency. (C) Sequential addition of a *meta*-substituent (X and Y) on the distal aromatic rings had favorable and additive effects on potency. Dose response curves of the different ISRIB analogs are shown in Figure 1-2-S1.

Figure 1-2-S1



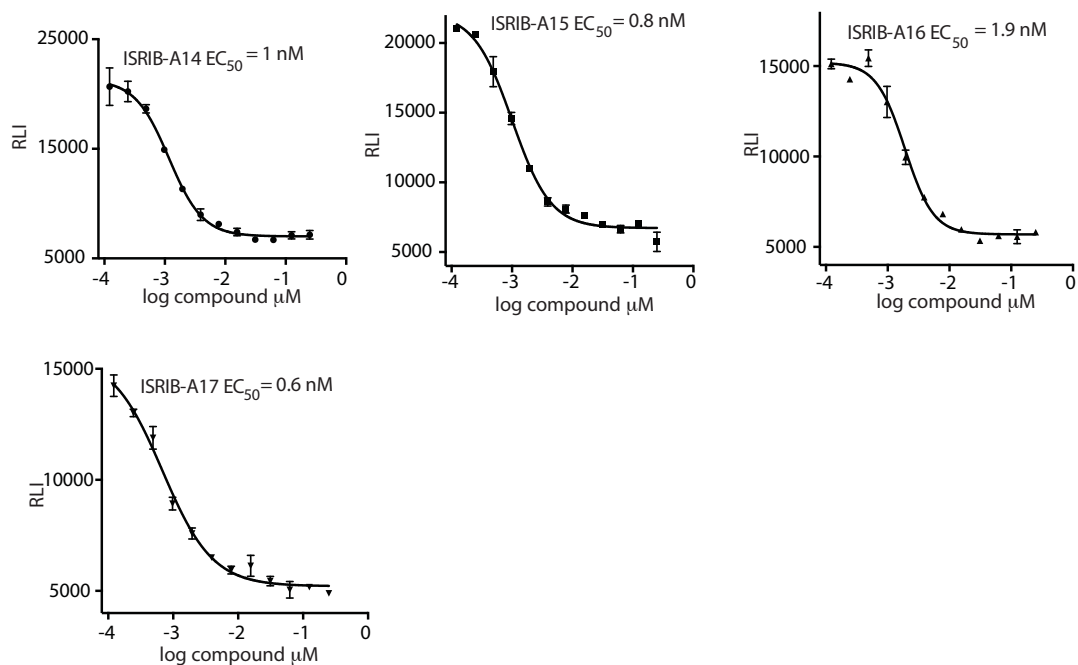


Figure 1-2-S1

EC₅₀ of ISRIB analogs: Activation of the ATF4 luciferase reporter in HEK293T cells was measured. Cells were treated with 1 μg/ml of tunicamycin to induce ER stress and different concentrations of the analogs for 7 h. Relative luminescence intensity (RLI) was plotted as a function of the concentration of the indicated ISRIB analog (N = 2, mean +/- SD).

Figure 1-3

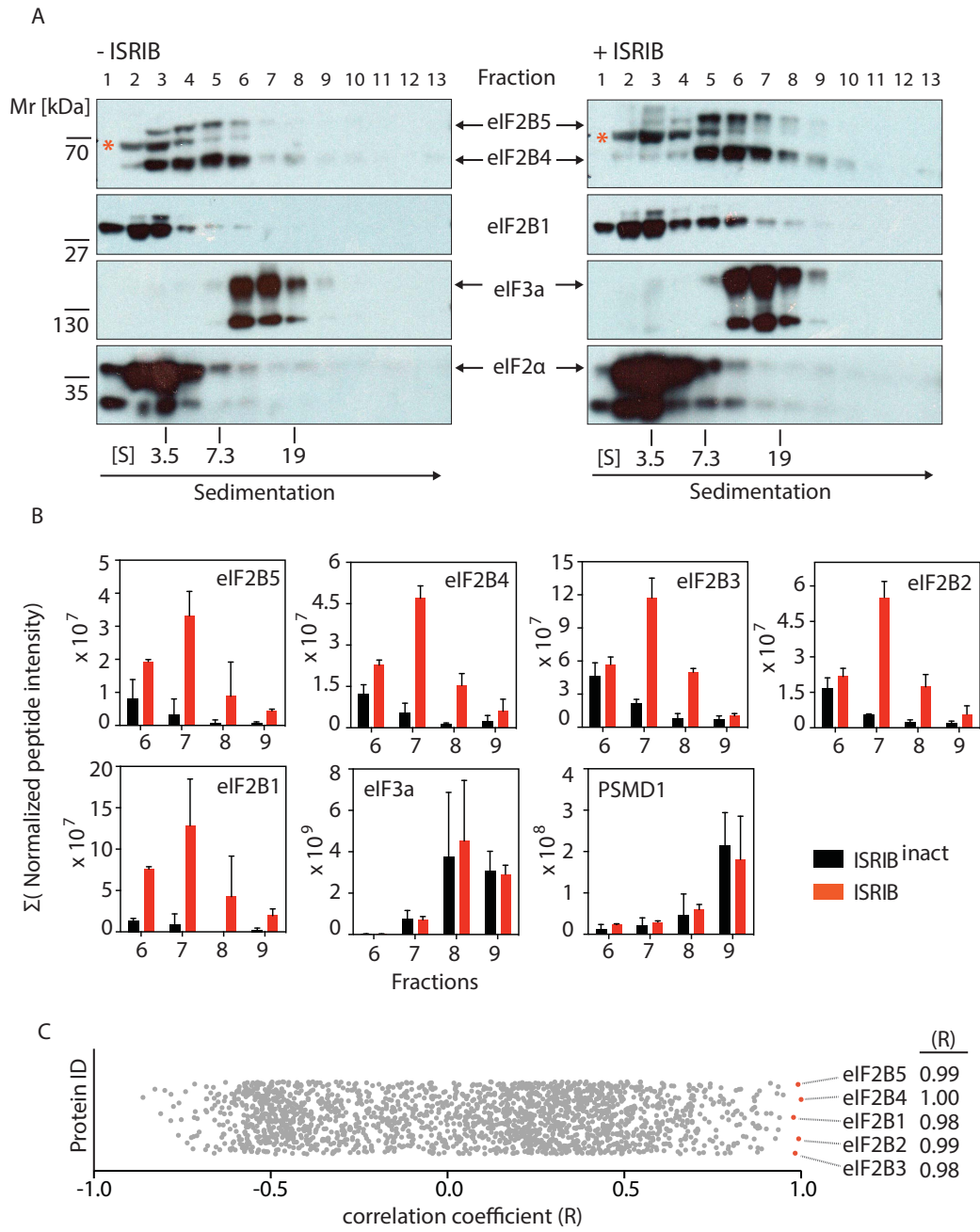
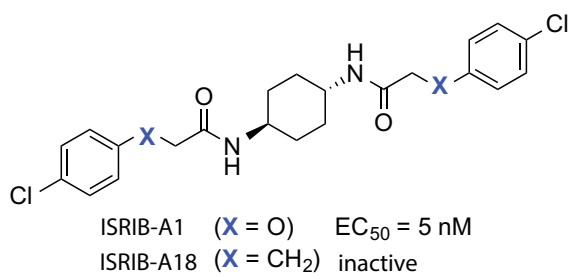


Figure 1-3

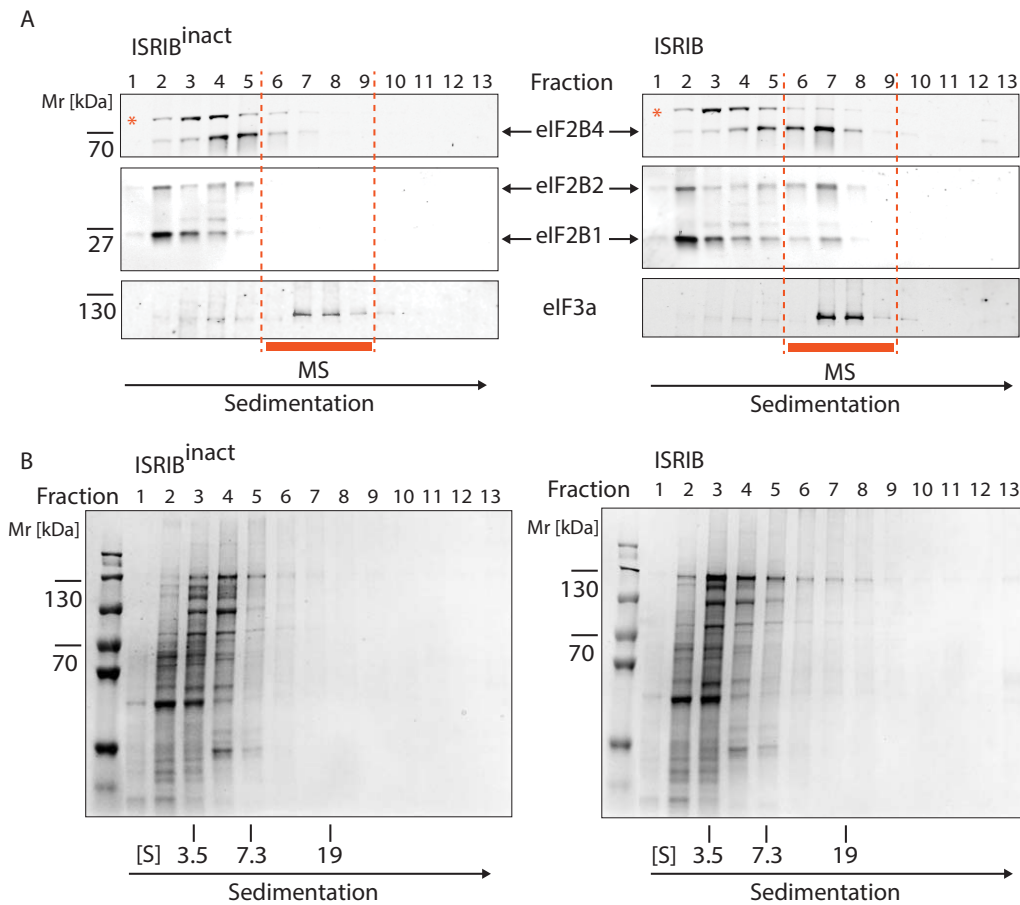
ISRIB induces dimerization of eIF2B in cells: (A) HEK293T cells were treated with or without 200 nM ISRIB and clarified lysates were loaded on a 5-20% sucrose gradient and subjected to centrifugation. Thirteen equal-size fractions were collected, protein was precipitated and run on a SDS-PAGE gel and immunoblotted with the indicated antibodies. The red asterisk indicates a background band that cross-reacts with the eIF2B4 antibody. Sedimentation was from left to right. Gradients were calibrated (in Svedberg units, “S”) with ovalbumin (S = 3.5; Mr = 44 kD); aldolase (S = 7.3; Mr = 158 kD) and thyroglobulin (S = 19; Mr = 669 kD). Shown is a representative blot (N = 3). (B) HEK293T cells and lysates were treated with 200 nM ISRIB or 200 nM ISRIBinact (ISRIB- A18; figure supplement 1) and clarified lysates were loaded on a 5-20% sucrose gradient and subjected to centrifugation. Thirteen equal sized fractions were collected and fractions 6-9 were precipitated, trypsinized and subjected to mass spectrometric analysis. The sum of the normalized peptide intensity of each eIF2B subunit as well as two control proteins, eIF3a and PSMD1 in each fraction was plotted. Two biological replicates were analyzed per condition (N = 2, +/-SEM). (C) Correlation coefficient (R) of the sum of the normalized peptide intensity profile through fractions 6-9 for each protein identified in the analysis with respect to eIF2B4 was plotted.

Figure 1-3-S1



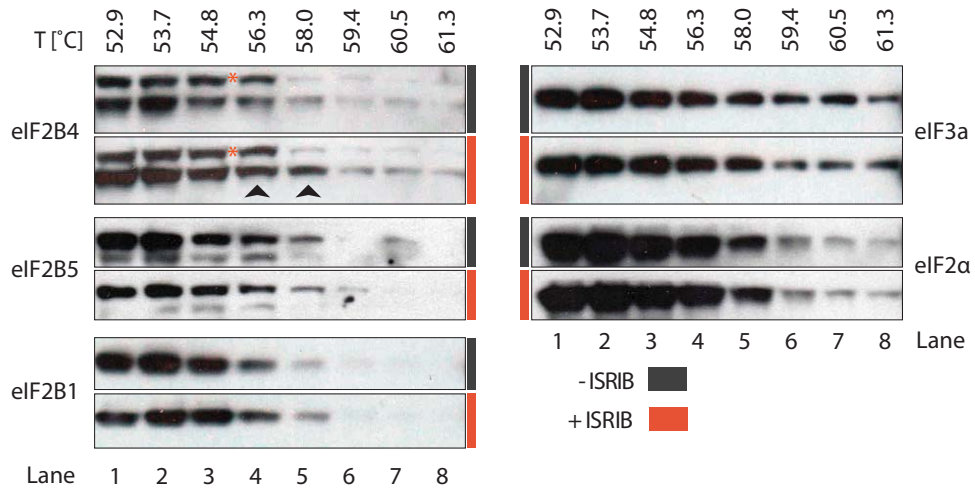
Structures of ISRIB (ISRIB-A1) and ISRIBinact (ISRIB-A18).

Figure 1-3-S2



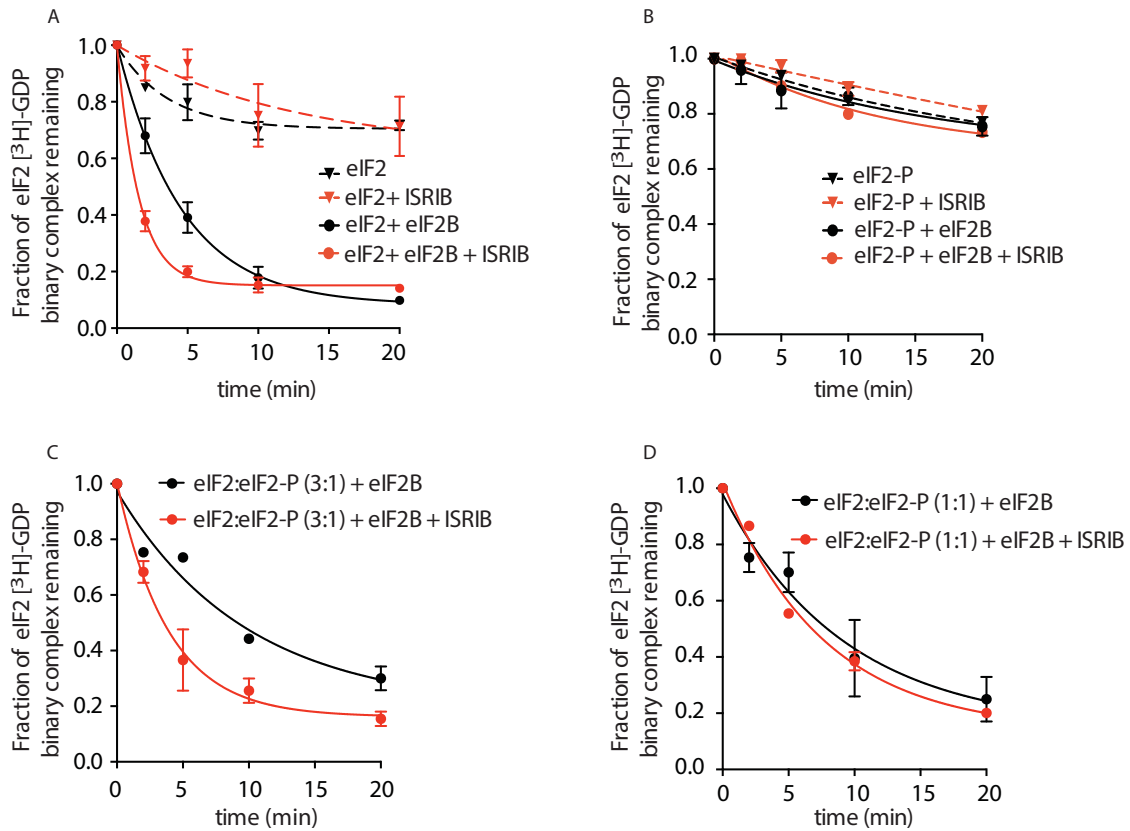
Analysis of the gradients subjected to mass spectrometric analysis in Fig. 1-3B: (A) Western blot analysis as in Fig. 3A. The protein composition of fractions 6-9 was analyzed by mass spectrometry (Fig. 1-3B). (B) Total protein across the sucrose gradient visualized by Coomassie blue staining.

Figure 1-4



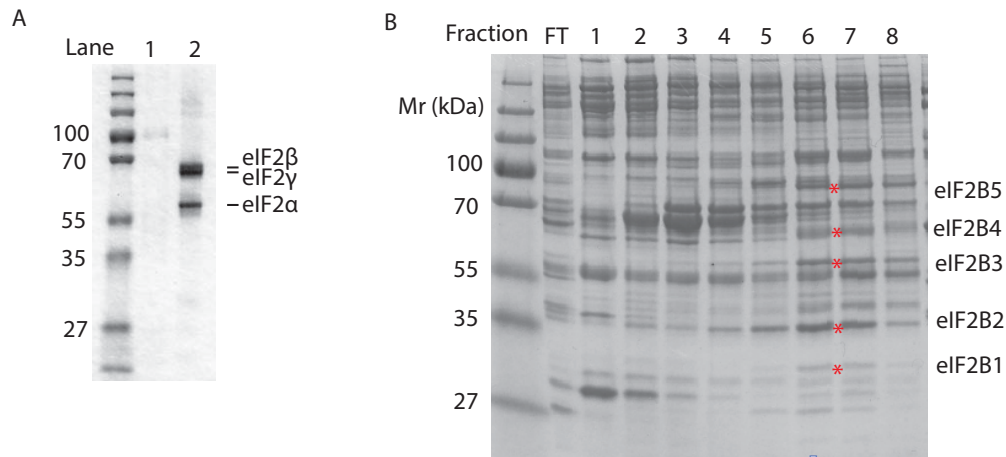
ISRIB enhances the thermo-stability of the regulatory subunit of eIF2B: Clarified HEK293 cell lysates were treated with DMSO (-ISRIB) or with 200 nM ISRIB (+ ISRIB) for 20 min. Treated and untreated lysates were partitioned into smaller aliquots and heated to different temperatures for 3 min and then centrifuged to remove precipitated proteins. The supernatant fraction was loaded onto a SDS-PAGE gel and immunoblotted with the indicated antibodies. The red asterisk indicates a background band that cross-reacts with the eIF2B4 antibody. Shown is a representative blot (N = 3).

Figure 1-5



ISIRIB enhances the GEF activity of eIF2B in vitro: eIF2 was preloaded with [3H]-GDP and the fraction of binary complex remaining was measured by filter binding. Partially purified eIF2B or buffer was added at $t = 0$ min. An aliquot of the reaction was stopped at the indicated times, filtered through a nitrocellulose membrane and radioactivity was measured. (A) Purified eIF2 was incubated with buffer (± 100 nM ISIRIB, dashed lines) or partially purified eIF2B (± 100 nM ISIRIB, solid lines) for the indicated times and the remaining fraction of [3H]-GDP-eIF2 was measured ($N = 3$, \pm SD). (B) Purified and phosphorylated eIF2 (eIF2-P) was preloaded with [3H]-GDP and incubated with buffer (± 100 nM ISIRIB, dashed lines) or partially purified eIF2B (± 100 nM ISIRIB, solid lines) for the indicated times and the remaining fraction of [3H]-GDP-eIF2 was measured ($N = 2$, \pm SD). (C) eIF2 was preloaded with [3H]-GDP and mixed with eIF2-P at a ratio of 3:1 and then incubated with eIF2B with or without 100 nM ISIRIB for the indicated times and the remaining fraction of [3H]-GDP-eIF2 was measured ($N = 2$, \pm SD). (D) eIF2 was preloaded with [3H]-GDP and mixed with eIF2-P at a ratio of 1:1 and then incubated with eIF2B with or without 100 nM ISIRIB for the indicated times and the remaining fraction of [3H]-GDP-eIF2 was measured ($N = 2$, \pm SD). Purified human eIF2 and partially purified rabbit reticulocyte eIF2B are shown in Figure 1-5-S1.

Figure 1-5-S1



Purified human eIF2 and rabbit reticulocyte eIF2B: Purified human eIF2 (panel A, lane 2), recombinant GST-PERK (panel A, lane 1) and partially purified rabbit reticulocyte eIF2B (panel B) were analyzed by SDS-PAGE and stained with Coomassie blue dye. Red asterisks indicate the migration of the five subunits of eIF2B. We utilized fractions 6 and 7 of the Mono-Q column for the guanine nucleotide exchange assays in Figure 1-5. We estimate that the eIF2B complex represents ~ 10% of the total protein in these fractions.

MATERIALS AND METHODS

Chemicals

Thapsigargin (Tg) was obtained from Sigma–Aldrich (St Louis, MO). Tunicamycin (Tm) was obtained from Calbiochem EMB Bioscience (Billerica, CA). The GSK PERK inhibitor (G797800) was obtained from Toronto Research Chemicals (North York, ON, Canada).

Cell culture

HEK293T and K562 cells were maintained at 37C, 5% CO₂ in either DMEM (HEK293T) or RPMI (K562) media supplemented with 10% FBS, L-glutamine and antibiotics (penicillin and streptomycin).

shRNA screening reporter cell line

The lentiviral reporter vector, pMK1163, contains a CMV promoter driving expression of a fusion transcript with the following elements: the 5' end of the human ATF4 mRNA up to the start codon of the ATF4-encoding ORF, an ORF encoding Venus (adapting a previously published strategy [Lu et al., 2004; Vattam and Wek, 2004]), followed by an IRES driving translation of tagBFP. The elements of this vector were generated as follows: we PCR-amplified the ATF4 region from human cDNA prepared from K562 cells using primers:

oMK305 (5'-CGTACTCGAGTTTCTACTTTGCCCGCCACAG-3') and

oMK306 (5'-GCTCCTCGCCCTTGCTCACCATGTTGCGGTGCTTTGCTGGAATCG-3').

Venus was amplified from DAA307 (gift from Diego Acosta-Alvear), using primers

oMK272 (5'-ATGGTGAGCAAGGGCGAGGAGC-3') and

oMK308 (5'-GCTAGAATTCTTACTTGTACAGCTCGTCCATGCC-3').

The ATF4-Venus fusion was generated by PCR reaction using the two PCR products described above as templates, and oMK305 and oMK308 as primers. The EMCV IRES was amplified from plasmid pPPCX-IRES-GFP (gift from Diego Acosta-Alvear). tagBFP was amplified from a tagBFP plasmid (Evrogen, Moscow, Russia). The plasmid pMK1163 is in the lentiviral vector pSicoR (Ventura et al., 2004), and its sequence is provided in Figure 1—source data 1. Human K562 cells were transduced with pMK1163 and monoclonal cell lines were generated using FACS. One clone was selected as our reporter cell line based on low base-line expression of Venus and high expression following thapsigargin treatment (high dynamic range).

Pooled shRNA screen

The reporter cell line was transduced with a pooled next-generation shRNA library. We used a sub-library that targets 2933 human genes associated with proteostasis, each with on average 25 independent shRNAs, and contains >1000 negative control shRNAs. After transduction, transduced cells were selected with puromycin (0.65 $\mu\text{g}/\text{ml}$) for 2 days, and then grown in the absence of puromycin for 2 days. Cells were then separated into two populations, which were treated for 7 hr with either 300 nM thapsigargin alone or 300 nM thapsigargin and 15 nM ISRIB. Cells were then sorted based on reporter fluorescence using a BD FACS Aria2. Cells from the thirds of the population with the highest and lowest reporter levels were collected. Genomic DNA was isolated from FACS-sorted populations, and shRNA-encoding cassettes were PCR-amplified and subjected to deep sequencing as previously described (Kampmann et al., 2014). Using our previously described analysis pipeline (Kampmann et al., 2013, 2014), we calculated a quantitative phenotype ε for each shRNA, which represents the \log_2 ratio of its frequency in the high-

fluorescence population over its frequency in the low-fluorescence population, from which the median of the negative control phenotypes was subtracted (Kampmann et al., 2013). For each gene, ϵ phenotypes for the ~ 25 shRNAs targeting the gene were compared to ϵ phenotypes for the negative control shRNAs, and p values were calculated using the Mann–Whitney U test to detect genes whose knockdown significantly modulated activation of the uORFs-ATF4-venus reporter in response to thapsigargin in the absence or presence of ISRIB. p values for all 2933 genes targeted by the sublibrary we used are listed in Figure 1—source data 2.

Cell-based assay to measure the potency of ISRIB analogs

HEK293T cells carrying an ATF4 luciferase reporter (as previously described in [Sidrauski et al., 2013]) were plated on poly-lysine coated 96 well plates (Greiner Bio-One, Monroe, NC) at 30,000 cells per well. Cells were treated the next day with tunicamycin (1 $\mu\text{g/ml}$) and different concentrations (serial dilution) of each compound for 7 hr. Luminescence was measured using One Glo (Promega, Madison, WI) as specified by the manufacturer. EC50 values were calculated by plotting $\log_{10} [\mu\text{M}]$ for each compound as a function of the relative luminescence intensity or response. The EC50 corresponds to the concentration that provokes a half-maximal response.

Sucrose gradients

HEK293T cells were plated on 150 mm plates, treated with or without 200 nM ISRIB for 20 min, washed twice with ice-cold PBS, collected and centrifuged for 3 min at 800 rcf at 4°C. The pellets were resuspended in ice-cold lysis buffer: 50 mM Tris pH = 7.5, 400 mM KCl, 4 mM Mg(OAc)₂, 0.5% Triton X-100 and protease inhibitors (EDTA-free protease inhibitor tablets, Roche, South San Francisco, CA). The lysates were clarified at 20,000 \times g for 15 min at 4°C and the supernatant

was then subjected to a high-speed spin at 100,000×g for 30 min at 4°C to pellet the ribosomes. The supernatants were then loaded on a 5–20% sucrose gradient and centrifuged in a SW55 rotor for 14 hr at 40,000 rpm 4°C. 13 fractions were collected, protein was chloroform-methanol precipitated, resuspended in SDS-PAGE loading buffer and loaded on SDS-PAGE 10% gels (Bio-Rad, Hercules, CA).

Protein analysis

Proteins were transferred to nitrocellulose and probed with primary antibodies diluted in phosphate-buffered saline supplemented with 0.1% Tween 20 and 5% bovine serum albumin. The following antibodies were used: eIF2B1 (1:1000; Proteintech 18010-1-AP, Chicago, IL), eIF2B2 (1:500; Proteintech 11034-1-AP), eIF2B4 (1:1000; Proteintech 11332-1-AP), eIF2B5 (1:500; Santa Cruz Biotechnologies sc-5558, Dallas, TX), eIF3a (1:1500; Cell Signaling Technology #3411, Danvers, MA) and eIF2 α (1:1500; Cell Signaling Technology #5324). Following primary antibody incubation, either HRP-conjugated secondary antibody (Promega) or IRdye conjugated secondary antibodies (LI-COR Biosciences, Lincoln, NE) was used. Immunoreactive bands were detected using either enhanced chemi-luminescence (Bio-Rad) or the LI-COR Odyssey imaging system.

Mass spectrometry of sucrose gradient fractions

HEK293T cells were treated with ISRIB or ISRIBinact (ISRIB-A18, Figure 1-3-S1) at 200 nM for 20 min. Cells were then subjected to three liquid nitrogen freeze–thaw cycles in a modified lysis buffer devoid of Triton X-100 and supplemented with ISRIB or ISRIBinact at 50 nM. Lysates were loaded onto a 5–20% sucrose gradient. Proteins in fractions 6–9 were chloroform-methanol

precipitated and re-suspended in 0.1 M tetraethylammonium bromide (TEAB), 150 mM NaCl and 8M Urea and digested with trypsin as previously described (Ramage et al., 2015). Digested peptide mixtures were analyzed in technical duplicate by LC-MS/MS on a Thermo Scientific LTQ Orbitrap Elite mass spectrometry system equipped with a Proxeon Easy nLC 1000 ultra high-pressure liquid chromatography and autosampler system. Samples were injected onto a C18 column (25 cm × 75 µm I.D.) packed with ReproSil Pur C18 AQ (1.9 µm particles) in 0.1% formic acid and then separated with a 1-hr gradient from 5% to 30% ACN in 0.1% formic acid at a flow rate of 300 nl/min. The mass spectrometer collected data in a data-dependent fashion, collecting one full scan in the Orbitrap at 120,000 resolution followed by 20 collision-induced dissociation MS/MS scans in the dual linear ion trap for the 20 most intense peaks from the full scan. Dynamic exclusion was enabled for 30 s with a repeat count of one. Charge state screening was employed to reject analysis of singly charged species or species for which a charge could not be assigned. Raw mass spectrometry data were analyzed using the MaxQuant software package (version 1.3.0.5) (Cox and Mann, 2008). Data were matched to the SwissProt human proteins (downloaded from UniProt on 2/15/13, 20,259 protein sequence entries). MaxQuant was configured to generate and search against a reverse sequence database for false discovery rate calculations. Variable modifications were allowed for methionine oxidation and protein N-terminus acetylation. A fixed modification was indicated for cysteine carbamidomethylation. Full trypsin specificity was required. The first search was performed with a mass accuracy of ± 20 parts per million and the main search was performed with a mass accuracy of ± 6 parts per million. A maximum of five modifications were allowed per peptide. A maximum of two missed cleavages were allowed. The maximum charge allowed was 7+. Individual peptide mass tolerances were allowed. For MS/MS matching, a mass tolerance of 0.5 Da was allowed and the top six peaks per 100 Da were analyzed.

MS/MS matching was allowed for higher charge states, water and ammonia loss events. The data were filtered to obtain a peptide, protein, and site-level false discovery rate of 0.01. The minimum peptide length was 7 amino acids. Results were matched between runs with a time window of 2 min for technical duplicates.

CETSA

CETSA were adapted from a previously described protocol (Martinez Molina et al., 2013). HEK293T cells were lysed in a buffer containing: 50 mM Tris pH = 7.5, 400 mM KCl, 4 mM Mg(OAc)₂, 0.5% Triton X-100 and protease inhibitors (EDTA-free protease inhibitor tablets, Roche). The lysates were clarified at 20,000×g for 15 min at 4°C. The supernatant was then incubated with ISRIB (1 μM, 0.1% DMSO) or DMSO (0.1%) at 30°C for 20 min, and subsequently spun at 100,000×g for 30 min at 4°C to pellet ribosomes. Supernatants following the high-speed spin were divided into PCR tubes and subjected to a gradient of temperatures for 3 min using the thermal cycler's built-in gradient function, such that column one corresponded to 52°C and column 12 corresponded to 62°C (Tetrad 2 Thermal Cycler, Bio-Rad). Samples were allowed to cool for 3 min at room temperature, transferred to microfuge tubes, and spun at 20,000×g for 20 min at 4°C to separate the soluble fraction from the insoluble precipitates. The soluble fraction was then loaded on a 10% SDS-PAGE gel (Bio-Rad) and analyzed by Western blotting as described above.

Purification of eIF2B

Rabbit reticulocyte lysate was obtained from Greenhectares (<http://greenhectares.com>). eIF2B was purified as previously described (Oldfield and Proud, 1992). In brief, the reticulocyte lysate was thawed and protease inhibitor added (EDTA-free protease inhibitor tablets, Roche). Ribosomes

were precipitated by centrifugation (45,000 rpm for 4.5 hr, Beckman 50.2 Ti at 4°C) and the supernatant was used as a source of eIF2B. KCl was added slowly to 100 mM final concentration and filtered using a 0.2 µm conical tube filter unit. The filtrate was loaded on a SP-Sepharose fast flow column (20 ml) pre-equilibrated with Buffer A (20 mM Hepes/NaOH pH = 7.6, 10% glycerol, 100 mM KCl, 0.1 mM EDTA and 2 mM DTT). A step gradient was used (100, 200 and 400 mM KCl). eIF2B eluted at 400 mM KCl. The eluate was diluted slowly by adding Buffer A (with no KCl) to 100 mM KCl and then loaded on a Q-Sepharose (20 ml) pre-equilibrated with Buffer A. A step gradient was used (300 mM and 500 mM KCl) with eIF2B eluting at 500 mM KCl. The eluate was dialyzed overnight with Buffer A and loaded to a Mono Q (5-50 GL, GE Healthcare, Wauwatosa, WI) equilibrated with buffer A (a continuous gradient 100–500 mM KCl was used) and eIF2B eluted at 350 mM KCl. The eluate was buffer exchanged with Buffer A and aliquots were flash frozen in liquid N₂.

Purification of eIF2

Human eIF2 was purified from HeLa cells as described previously (Fraser et al., 2007). In brief, from the 40–50% ammonium sulfate precipitate of post-nuclear HeLa cell lysate, eIF2 was purified through a series of chromatographic steps which included a Mono Q 10/10 column (GE Healthcare), a Mono S 10/10 column (GE Healthcare), a CHT5-1 ceramic hydroxyapatite column (Bio-Rad), and a Superose 6 16/60 column (GE Healthcare). The protein was stored at –80°C in buffer containing 20 mM Hepes-K pH 7.5, 150 mM KCl, 1 mM DTT, and 10% glycerol.

GDP dissociation assay

GDP dissociation assays were adapted from a previously described protocol (Sokabe et al., 2012). For each reaction purified eIF2 (21 pmol) was incubated with 0.6 μ Ci [3 H]-GDP (40 Ci/mmol, PerkinElmer, Waltham, MA) in a reaction buffer (20 mM HEPES pH 7.5, 80 mM KCl, 1 mM DTT, 1 mg/ml creatine phosphokinase (EMD Millipore, Billerica, MA), 5% glycerol) without magnesium at 37°C for 10 min, and then further incubated with 1 mM Mg(OAc)₂ at 30°C for 3 min with or without ISRIB (100 nM) in a total volume of 60 μ l. The reaction was initiated by the addition of 60 nmol unlabeled GDP with or without eIF2B (0.6 μ l of partially purified rabbit reticulocyte eIF2B, which correspond to approximately 0.3 pmoles of the complex). At each time point, an aliquot was taken (10 μ l) and the reaction was stopped by addition to 300 μ l ice-cold stop buffer (reaction buffer with 5 mM Mg(OAc)₂), immediately filtered through a HAWP nitrocellulose membrane filter (EMD Millipore) on a vacuum manifold and washed twice with 1 ml ice-cold stop buffer. Filters were dried and remaining [3 H]-GDP bound to eIF2 was counted by liquid scintillation in Ecoscint (National Diagnostics, Atlanta, GA). Data collected were fitted to a first-order exponential decay.

eIF2-P was synthesized by incubating eIF2 (1.76 μ M) with recombinant GST-PERK (500 nM) at 37°C for 45 min in a reaction buffer containing: 0.5 mM ATP, 50 mM Tris-HCl pH 7.5, 4 mM MgCl₂, 100 mM NaCl, 1 mM *tris*(2-carboxyethyl)phosphine (TCEP), 1% glycerol. The phosphorylation reaction was stopped by the addition of 1 μ M GSK PERK inhibitor (Toronto Research Chemicals) and 4 mM EDTA to chelate magnesium ions. For eIF2-P•GDP dissociation reactions (Figure 1-5B), eIF2-P (21 pmol) was loaded with [3 H]-GDP. For experiments where eIF2 was mixed with eIF2-P (Figure 1-5C,D, unphosphorylated eIF2 was loaded with [3 H]-GDP and mixed (3:1 or 1:1) with eIF2-P, which was not loaded with [3 H]-GDP, such that the sum of eIF2 and eIF2-P equaled 21 pmol. GDP dissociation assays were conducted as described above in the

presence of 50 nM GSK PERK inhibitor to ensure that the residual PERK kinase did not phosphorylate eIF2 during the course of the dissociation assay.

Purification of GST-PERK

Cytosolic human PERK was codon-optimized for *Escherichia coli* expression by Genewiz Inc. A construct was then cloned into a PGEX-6P-2 vector for expression using two rounds of In-Fusion cloning (Clontech, Mountain View, CA) (535–1093 Δ 660–868). The cytosolic portion of PERK, lacking the unstructured loop region (amino acids 535–1093 Δ 660–868) was then co-expressed with a tag-less lambda phosphatase to produce a fully dephosphorylated PERK protein in BL21 star (DE3) (Life Technologies, Carlsbad, CA). Cells were grown to an OD600 of 0.5 before induction with 0.1 mM IPTG at 15°C for 24 hr. Cells were harvested and lysed using AVESTIN Emulsiflex-C3 in a buffer containing 50 mM Tris-HCl, pH 8.0, 500 mM NaCl, 5% glycerol, 5 mM TCEP (buffer A) and EDTA-free COMPLETE protease inhibitor cocktail (Roche). The lysate was cleared by centrifugation at 100,000 \times g before batch-binding to a GST-Sepharose resin. The resin was washed 5 times with buffer A. The protein was loaded onto a HiTrap Q HP column to remove remaining lambda phosphatase. The PERK (535–1093 Δ 660–868) protein was then concentrated and fractionated on a Superdex 200 GL (GE Healthcare) to remove protein aggregates.

Chemical syntheses

General methods

Commercially available reagents and solvents were used as received. Compounds ISRIB-A1 and ISRIB-A2 were prepared as previously reported (Sidrauski et al., 2013b). Compound ISRIB-A7 was available commercially from Specs (The Netherlands). ¹H NMR spectra were recorded on a Varian INOVA-400 400 MHz spectrometer and a Bruker Avance 300 300 MHz spectrometer. Chemical shifts are reported in δ units (ppm) relative to residual solvent peak. Coupling constants (*J*) are reported in hertz (Hz). LC-MS analyses were carried out using Waters 2795 separations module equipped with Waters 2996 photodiode array detector, Waters 2424 ELS detector, Waters micromass ZQ single quadropole mass detector, and an XBridge C18 column (5 μ m, 4.6 \times 50 mm). Microwave reactions were carried out in a CEM Discover microwave reactor.

General procedure A for amide coupling

To a solution of the carboxylic acid (1 equiv.) in *N,N*-dimethylformamide, were sequentially added 1-hydroxybenzotriazole hydrate (1.2 equiv.), 1-(3-dimethylaminopropyl)-3-ethylcarbodiimide hydrochloride (1.2 equiv.), 2-(4-chlorophenoxy)-*N*-[(1*r*,4*r*)-4-aminocyclohexyl]acetamide trifluoroacetic acid (1.0 equiv., prepared as described in the synthesis of ISRIB-A8, below) and *N,N*-diisopropylethylamine (1.5 equiv). The reaction mixture was stirred at room temperature until judged complete by LC-MS and then diluted with water (2 ml). The mixture was vigorously vortexed, centrifuged and the water was decanted. This washing protocol was repeated with water (2 ml) and then with diethyl ether (2 ml). The wet solid was dissolved in dichloromethane (10 ml)

and dried over anhydrous magnesium sulfate. The solids were removed by filtration and the filtrate was concentrated by rotary evaporation to obtain the product.

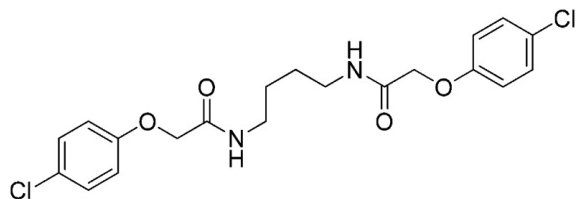
General procedure B for amide coupling

To a solution of the carboxylic acid (2 equiv.) in N,N-dimethylformamide were sequentially added 1-hydroxybenzotriazole hydrate (2 equiv.), 1-(3-dimethylaminopropyl)-3-ethylcarbodiimide hydrochloride (2 equiv.), the diamine (1.0 equiv.) and N,N-diisopropylethylamine (6 equiv.). The reaction mixture was stirred at room temperature until judged complete by LC-MS and then diluted with water. The precipitate formed was washed with water and 10% diethyl ether in dichloromethane. The precipitate was dried in vacuo to obtain the product.

General procedure C for amide coupling

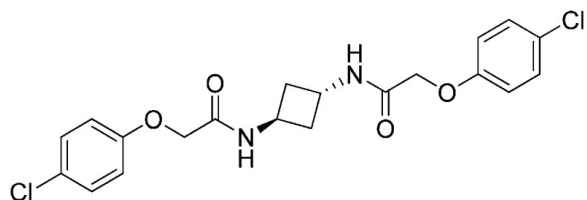
To a solution of (1r,4r)-cyclohexane-1,4-diamine (1 equiv.) in N,N-dimethylformamide were added the carboxylic acid (2 equiv.), 1-[bis(dimethylamino)methylene]-1H-1,2,3-triazolo[4,5-b]pyridinium 3-oxid hexafluorophosphate (2.1 equiv.) and N,N-diisopropylethylamine (4 equiv.). The reaction mixture was vigorously stirred at room temperature until judged complete by LC-MS. Water (2 ml) was added. The mixture was centrifuged and the water was decanted. This washing protocol was repeated thrice and the resulting wet solid was concentrated down with toluene (10 ml) in a rotary evaporator. The residual product was washed with diethyl ether (10 ml) and concentrated using rotary evaporation to obtain the product.

2-(4-Chlorophenoxy)-N-{4-[2-(4-chlorophenoxy)acetamido]butyl}acetamide (ISRIB-A3)



To a solution of 1,4-diaminobutane (0.032 g, 0.2 mmol) in tetrahydrofuran (1.0 ml), were added 4-chlorophenoxyacetyl chloride (0.062 ml, 0.4 mmol) and N,N-diisopropylethylamine (0.173 ml, 1.0 mmol). The reaction mixture was stirred at room temperature for 20 hr and then partitioned between 1:1 mixture of water/dichloromethane (20 ml). The organic layer was washed with 10% aqueous potassium hydrogen sulfate, water and brine. The organic phase was then dried over magnesium sulfate, filtered, and concentrated to obtain a brownish orange solid. The brownish orange solid was triturated with diethyl ether and the resulting solids were separated by centrifugation and dried to obtain 26 mg (31%) of the title compound as tan powder. ¹H NMR (400 MHz, DMSO-d₆) δ 8.06 (t, J = 5.6 Hz, 2H), 7.30–7.32 m, 4H), 6.93–6.95 (m, 4H), 4.43 (s, 4H), 3.08 (d, J = 5.7Hz, 4H), 1.37 (br. s, 4H) LC-MS: m/z = 425 [M + H, ³⁵Cl]⁺, 427 [M + H, ³⁷Cl]⁺.

2-(4-Chlorophenoxy)-N-[(1r,3r)-3-[2-(4-chlorophenoxy)acetamido]cyclobutyl]acetamide (ISRIB-A4)

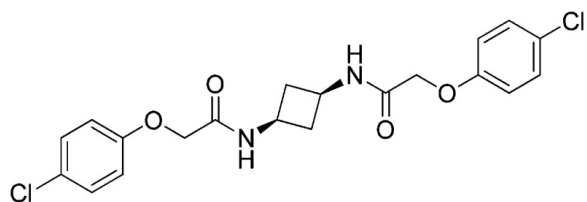


To a cooled (0°C) solution of tert-butyl N-[(1r,3r)-3-aminocyclobutyl]carbamate (0.05 g, 0.277 mmol) in 1,2-dichloroethane (1.38 ml), was added trifluoroacetic acid (1.38 ml). The reaction

mixture was stirred at room temperature for 2 hr and then concentrated down to dryness to obtain 100 mg of (1r,3r)-cyclobutane-1,3-bis(aminium) ditrifluoroacetate which was used without further purification.

To a solution 4-chlorophenoxyacetic acid (0.19 g, 0.63 mmol) in N,N-dimethylformamide (1.0 ml) were sequentially added 1-hydroxybenzotriazole hydrate (0.12 g, 0.63 mmol), 1-(3-dimethylaminopropyl)-3-ethylcarbodiimide hydrochloride (0.175 g, 0.63 mmol), (1r,3r)-cyclobutane-1,3-bis(aminium) ditrifluoroacetate (0.1 g, 0.31 mmol) and N,N-diisopropylethylamine (0.34 ml, 1.91 mmol). The reaction mixture was stirred at room temperature for 2 hr and then subjected to conditions described in procedure B to afford 72 mg (54%) of the title compound. ¹H NMR (300 MHz, CDCl₃) δ 7.29–7.35 (m, 4H), 6.91 (dd, *J* = 9, 2.2 Hz, 4H), 6.80 (d, *J* = 7.6 Hz, 2H), 4.60–4.62 (m, 2H), 4.48 (s, 4H), 2.46–2.51 (m, 4H) LC-MS: *m/z* = 423 [M + H]⁺.

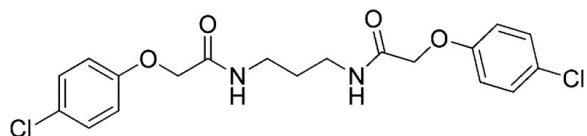
**2-(4-Chlorophenoxy)-N-[(1s,3s)-3-[2-(4-chlorophenoxy)acetamido]cyclobutyl]acetamide
(ISRIB-A5)**



To a cooled (0°C) solution of tert-butyl N-[(1 s,3 s)-3-aminocyclobutyl]carbamate (0.05 g, 0.277 mmol) in 1,2-dichloroethane (1.38 ml), was added trifluoroacetic acid (1.38 ml). The reaction mixture was stirred at room temperature for 1.5 hr and then concentrated down to dryness to obtain 100 mg of (1 s,3 s)-cyclobutane-1,3-bis(aminium) ditrifluoroacetate which was used without further purification.

To a solution 4-chlorophenoxyacetic acid (0.19 g, 0.63 mmol) in N,N-dimethylformamide (1.0 ml) were sequentially added 1-hydroxybenzotriazole hydrate (0.12 g, 0.63 mmol), 1-(3-dimethylaminopropyl)-3-ethylcarbodiimide hydrochloride (0.175 g, 0.63 mmol), (1 s,3 s)-cyclobutane-1,3-bis(aminium) ditrifluoroacetate (0.1 g, 0.31 mmol) and N,N-diisopropylethylamine (0.34 ml, 1.91 mmol). The reaction mixture was stirred at room temperature for 2 hr. The reaction mixture was then diluted with 5% methanol in dichloromethane, washed with water and brine. The organic layer was dried over magnesium sulfate, filtered and concentrated. The crude mixture was purified by flash column chromatography (40% acetone/hexanes) to obtain 34 mg (25%) of the title compound. ¹H NMR (300 MHz, CDCl₃) δ 7.26–7.29 (m, 4H), 6.84–6.87 (m, 4H), 6.77 (d, *J* = 6.5 Hz, 2H), 4.42 (m, 4H), 4.17–4.25 (s, 2H), 2.84–2.93 (m, 2H), 2.02–2.12 (m, 2H) LC-MS: *m/z* = 423 [M + H]⁺.

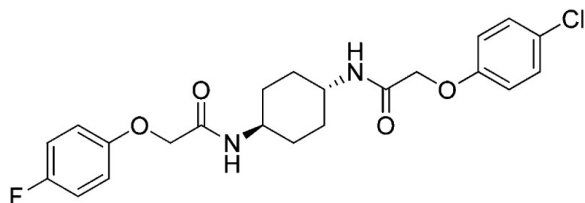
2-(4-Chlorophenoxy)-N-{3-[2-(4-chlorophenoxy)acetamido]propyl}acetamide (ISRIB-A6)



To a solution of 1,3-diaminopropane (0.017 ml, 0.2 mmol) in tetrahydrofuran (0.6 ml), was added 4-chlorophenoxyacetyl chloride (0.062 ml, 0.4 mmol) and N,N-diisopropylethylamine (0.08 ml, 0.5 mmol). The reaction mixture was stirred at room temperature for an hour and then partitioned between 1:1 mixture of water/dichloromethane (20 ml). The organic layer was washed with 10% aqueous potassium hydrogen sulfate, water and brine. The organic phase was then dried over magnesium sulfate, filtered and concentrated to obtain a brownish orange oil. The brownish orange oil was purified by flash column chromatography (5–80% acetone/dichloromethane) to obtain 41 mg (49%) of the title compound. ¹H NMR (400 MHz, CDCl₃) δ 7.24–7.26 (m, 4H), 7.15 (br.s,

2H), 6.85–6.87 (m, 4H), 4.45 (s, 4H), 3.08 (quint, $J = 6.3$ Hz, 4H), 1.37 (quint, $J = 6.2$ Hz, 2H)
LC-MS: $m/z = 411$ [M + H, ^{35}Cl]+, 413 [M + H, ^{37}Cl]+.

**2-(4-Fluorophenoxy)-N-[(1*r*,4*r*)-4-[2-(4-chlorophenoxy)acetamido]cyclohexyl]acetamide
(ISRIB-A8)**



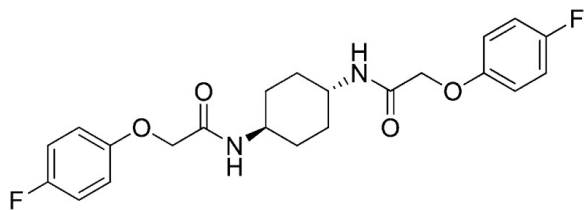
Step 1: To a mixture of *tert*-butyl *N*-[(1*r*,4*r*)-4-aminocyclohexyl]carbamate (0.750 g, 3.5 mmol) in THF (20 ml) were sequentially added *N,N*-diisopropylethylamine (0.914 ml, 5.25 mmol) and 4-chlorophenoxyacetyl chloride (0.573 ml, 3.78 mmol). The reaction mixture was vigorously stirred at room temperature for 3 hr and then diluted with water (100 ml). The precipitate was filtered and the solid was washed with water. The resulting solid was then diluted with diethyl ether and vacuum filtered. The filter cake was washed with diethyl ether. The residual ether was removed under vacuum to afford 1.103 g (82%) of *tert*-butyl *N*-[(1*r*,4*r*)-4-[2-(4-chlorophenoxy)acetamido]cyclohexyl]carbamate as a white solid. ^1H NMR (400 MHz, DMSO- d_6) δ 7.88 (d, $J = 7.87$ Hz, 1H), 7.25–7.37 (m, 2H), 6.93 (d, $J = 8.97$ Hz, 2H), 6.68 (d, $J = 7.69$ Hz, 1H), 4.41 (s, 2H), 3.51 (m, 1H), 3.13 (br. s., 1H), 1.72 (t, $J = 13.19$ Hz, 4H), 1.34 (s, 9H), 1.09–1.30 (m, 4H); LC-MS: $m/z = 405$ [M + Na, ^{35}Cl]+, 407 [M + Na, ^{37}Cl]+, 765 [2M + H, $^{35}\text{Cl} \times 2$]+, 767 [2M + H, ^{35}Cl , ^{37}Cl]+.

Step 2: To a suspension of *tert*-butyl *N*-[(1*r*,4*r*)-4-[2-(4-chlorophenoxy)acetamido]cyclohexyl]carbamate (0.5 g, 1.31 mmol) in dichloromethane (9 ml) were sequentially added triethylsilane (0.3 ml, 1.88 mmol), water (0.2 ml, 11.1 mmol), and

trifluoroacetic acid (3.0 ml, 39.2 mmol). The suspension quickly clarified and turned yellow upon addition of trifluoroacetic acid. The reaction mixture was vigorously stirred at room temperature for 30 min and then the solvent was removed by rotary evaporation. The resulting colorless oil was triturated with diethyl ether. After decanting the ether washes, residual solvent was removed under vacuum to afford 499 mg (96%) of 2-(4-chlorophenoxy)-N-[(1r,4r)-4-aminocyclohexyl]acetamide trifluoroacetic acid as a white solid. ¹H NMR (400 MHz, DMSO-d₆) δ 7.95 (d, *J* = 7.87 Hz, 1H), 7.77 (br. s., 3H), 7.31 (d, *J* = 8.97 Hz, 2H), 6.93 (d, *J* = 8.97 Hz, 2H), 4.43 (s, 2H), 3.54 (m, 1H), 2.93 (br. s., 1H), 1.90 (d, *J* = 9.16 Hz, 2H), 1.77 (d, *J* = 9.34 Hz, 2H), 1.31 (sxt, *J* = 11.50 Hz, 4H); LC-MS: *m/z* = 283 [M + H, ³⁵Cl]⁺, 285 [M + H, ³⁷Cl]⁺.

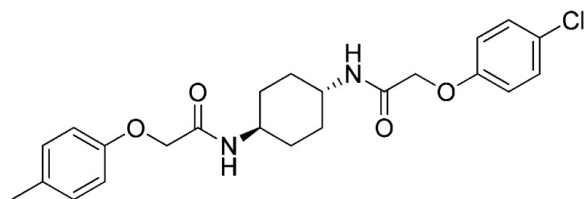
Step 3: To a solution of 4-fluorophenoxyacetic acid (0.009 g, 0.050 mmol) in N,N-dimethylformamide (1.0 ml) were sequentially added 1-hydroxybenzotriazole hydrate (0.009 g, 0.055 mmol), 1-(3-dimethylaminopropyl)-3-ethylcarbodiimide hydrochloride (0.012 g, 0.057 mmol), 2-(4-chlorophenoxy)-N-[(1r,4r)-4-aminocyclohexyl]acetamide trifluoroacetic acid (0.02 g, 0.050 mmol) and N,N-diisopropylethylamine (0.013 ml, 0.12 mmol). The reaction mixture was subjected to conditions described in procedure A to obtain 14 mg (60%) of the title compound as a white solid. ¹H NMR (400 MHz, DMSO-d₆) δ 7.88–7.92 (m, 2H), 7.31 (d, *J* = 9 Hz, 2H), 7.10 (t, *J* = 8.8 Hz, 2H), 6.92–6.95 (m, 4H), 4.39–4.42 (m, 4H), 3.57 (br. s, 2H), 1.74 (d, *J* = 5.9 Hz, 4H), 1.29–1.33 (m, 4H) LC-MS: *m/z* = 435 [M + H, ³⁵Cl]⁺, 437 [M + H, ³⁷Cl]⁺.

**2-(4-Fluorophenoxy)-N-[(1r,4r)-4-[2-(4-fluorophenoxy)acetamido]cyclohexyl]acetamide
(ISRIB-A9)**



To a solution 4-fluorophenoxyacetic acid (0.12 g, 0.7 mmol) in N,N-dimethylformamide (1.0 ml) were sequentially added 1-hydroxybenzotriazole hydrate (0.094 g, 0.7 mmol), 1-(3-dimethylaminopropyl)-3-ethylcarbodiimide hydrochloride (0.140 g, 0.7 mmol), (1r,4r)-cyclohexane-1,4-diamine (0.040 g, 0.35 mmol) and N,N-diisopropylethylamine (0.372 ml, 2.1 mmol). The reaction mixture was subjected to conditions described in procedure B to afford 73 mg (50%) of the title compound. ¹H NMR (300 MHz, CDCl₃) δ 7.02 (t, *J* = 8.3 Hz, 4H), 6.89–6.90 (m, 4H), 6.38 (d, *J* = 7.5 Hz, 2H), 4.43 (s, 4H), 3.88 (br. s, 2H), 2.07 (d, *J* = 5.7 Hz, 4H), 1.36–1.39 (m, 4H) LC-MS: *m/z* = 419 [M + H]⁺.

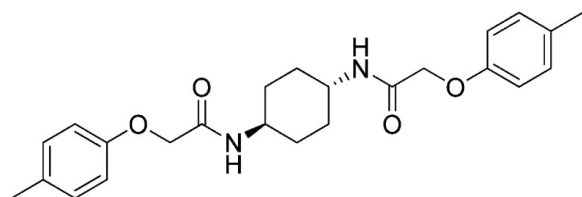
2-(4-Methylphenoxy)-N-[(1r,4r)-4-[2-(4-chlorophenoxy)acetamido]cyclohexyl]acetamide (ISRIB-A10)



To a solution 4-methyl-phenoxyacetic acid (0.016 g, 0.101 mmol) in N,N-dimethylformamide (1.0 ml) were sequentially added 1-hydroxybenzotriazole hydrate (0.014 g, 0.101 mmol), 1-(3-dimethylaminopropyl)-3-ethylcarbodiimide hydrochloride (0.02 g, 0.101 mmol), 2-(4-chlorophenoxy)-N-[(1r,4r)-4-aminocyclohexyl]acetamide trifluoroacetic acid (0.04 g, 0.101 mmol) and N,N-diisopropylethylamine (0.06 ml, 0.303 mmol). The reaction mixture was subjected to

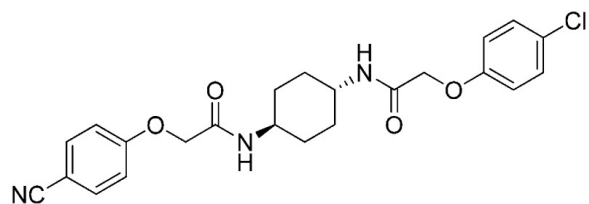
conditions described in procedure A to obtain 7 mg (16%) of the title compound as a white solid. ¹H NMR (400 MHz, DMSO-d₆) δ 7.91 (d, J = 8 Hz, 1H), 7.84 (d, J = 7.8 Hz, 1H), 7.31 (d, J = 8.8 Hz, 2H), 7.06 (t, J = 8.3 Hz, 2H), 6.94 (d, J = 8.8 Hz, 2H), 6.80 (d, J = 8.4 Hz, 2H), 4.42 (s, 2H), 4.35 (s, 2H), 3.56 (br. s, 2H), 2.20 (s, 3H), 1.73 (d, J = 6.6 Hz, 4H), 1.22–1.33 (m, 4H) LC-MS: m/z = 431 [M + H]⁺.

**2-(4-Methylphenoxy)-N-[(1r,4r)-4-[2-(4-methylphenoxy)acetamido]cyclohexyl]acetamide
(ISRIB-A11)**



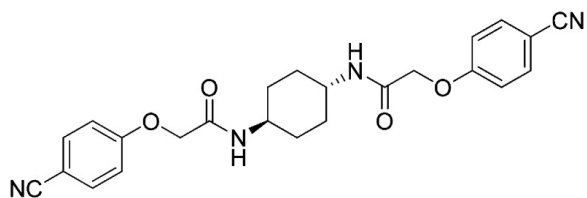
To a solution 4-methylphenoxyacetic acid (0.116 g, 0.7 mmol) in N,N-dimethylformamide (1.0 ml) were sequentially added 1-hydroxybenzotriazole hydrate (0.094 g, 0.7 mmol), 1-(3-dimethylaminopropyl)-3-ethylcarbodiimide hydrochloride (0.14 g, 0.7 mmol), (1r,4r)-cyclohexane-1,4-diamine (0.04 g, 0.35 mmol) and N,N-diisopropylethylamine (0.372 ml, 2.1 mmol). The reaction mixture was stirred at 52°C for 24 hr and then subjected to conditions described in procedure B to afford 84 mg (58%) of the title compound. ¹H NMR (400 MHz, DMSO-d₆) δ 7.84 (d, J = 6.8 Hz, 2H), 7.05 (d, J = 6.8 Hz, 4H), 6.80 (d, J = 6.6 Hz, 4H), 4.35 (s, 4H), 3.56 (br. s, 2H), 2.19 (s, 6H), 1.73 (br. s, 4H), 1.31 (br.s, 4H) LC-MS: m/z = 411 [M + H]⁺.

**2-(4-Cyanophenoxy)-N-[(1r,4r)-4-[2-(4-chlorophenoxy)acetamido]cyclohexyl]acetamide
(ISRIB-A12)**



To a solution 4-cyanophenoxyacetic acid (0.009 g, 0.050 mmol) in N,N-dimethylformamide (1.0 ml) were sequentially added 1-hydroxybenzotriazole hydrate (0.009 g, 0.055 mmol), 1-(3-dimethylaminopropyl)-3-ethylcarbodiimide hydrochloride (0.012 g, 0.057 mmol), 2-(4-chlorophenoxy)-N-[(1r,4r)-4-aminocyclohexyl]acetamide trifluoroacetic acid (0.02 g, 0.050 mmol) and N,N-diisopropylethylamine (0.013 ml, 0.12 mmol). The reaction mixture was subjected to conditions described in procedure A to obtain 14 mg (65%) of the title compound as a beige solid. ¹H NMR (400 MHz, DMSO-d₆) δ 7.99 (d, J = 7.9 Hz, 1H), 7.91 (d, J = 8.1 Hz, 1H), 7.76 (d, J = 8.8 Hz, 1H), 7.31 (d, J = 9.1 Hz, 1H), 7.07 (d, J = 8.8 Hz, 2H), 6.94 (d, J = 8.8 Hz, 2H), 4.55 (s, 2H), 4.42 (s, 2H), 3.56 (br. s, 2H), 1.74 (d, J = 7.7 Hz, 4H), 1.28–1.32 (m, 4H) LC-MS: m/z = 442 [M + H, ³⁵Cl]⁺, 444 [M + H, ³⁷Cl]⁺.

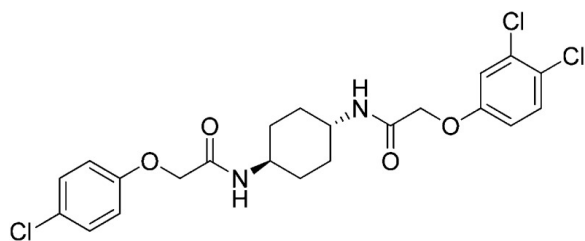
2-(4-Cyanophenoxy)-N-[(1r,4r)-4-[2-(4-cyanophenoxy)acetamido]cyclohexyl]acetamide (ISRIB-A13)



To a solution 4-cyanophenoxyacetic acid (0.124 g, 0.7 mmol) in N,N-dimethylformamide (1.0 ml) were sequentially added 1-hydroxybenzotriazole hydrate (0.094 g, 0.7 mmol), 1-(3-dimethylaminopropyl)-3-ethylcarbodiimide hydrochloride (0.14 g, 0.7 mmol), (1r,4r)-

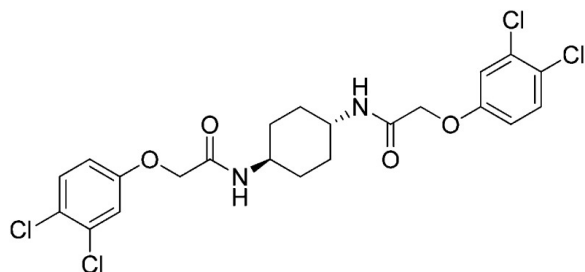
cyclohexane-1,4-diamine (0.04 g, 0.35 mmol) and N,N-diisopropylethylamine (0.372 ml, 2.1 mmol). The reaction mixture was subjected to conditions described in procedure B to afford 54 mg (36%) of the title compound. ¹H NMR (300 MHz, DMSO-d₆) δ 8.01 (d, *J* = 5.8 Hz, 2H), 7.76 (d, *J* = 6.8 Hz, 4H), 7.08 (d, *J* = 6.8 Hz, 4H), 4.55 (s, 4H), 3.56 (br. s, 2H), 1.75 (br. s, 4H), 1.31 (br. s, 4H) LC-MS: *m/z* = 433 [M + H]⁺.

2-(3,4-Dichlorophenoxy)-N-[(1r,4r)-4-[2-(4-chlorophenoxy)acetamido]cyclohexyl]acetamide (ISRIB-A14)



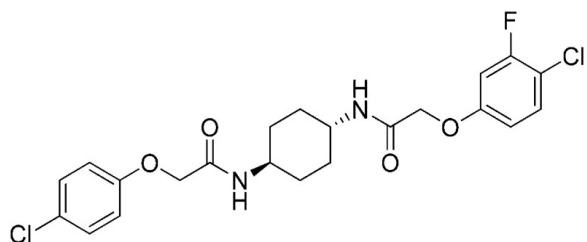
To a solution 3,4-dichlorophenoxyacetic acid (0.011 g, 0.050 mmol) in N,N-dimethylformamide (1.0 ml) were sequentially added 1-hydroxybenzotriazole hydrate (0.009 g, 0.055 mmol), 1-(3-dimethylaminopropyl)-3-ethylcarbodiimide hydrochloride (0.012 g, 0.057 mmol), 2-(4-chlorophenoxy)-N-[(1r,4r)-4-aminocyclohexyl]acetamide trifluoroacetic acid (0.020 g, 0.050 mmol) and N,N-diisopropylethylamine (0.013 ml, 0.12 mmol). The reaction mixture was subjected to conditions described in procedure A to obtain 21 mg (86%) of the title compound as a white solid. ¹H NMR (400 MHz, DMSO-d₆) δ 7.94 (d, *J* = 8.2 Hz, 1H), 7.91 (d, *J* = 8.2 Hz, 1H), 7.51 (d, *J* = 8.8 Hz, 1H), 7.31 (d, *J* = 9 Hz, 2H), 7.22 (d, *J* = 2.9 Hz, 1H), 6.92–6.95 (m, 3H), 4.48 (s, 2H), 4.42 (s, 2H), 3.56 (br. s, 2H), 1.74 (d, *J* = 6 Hz, 4H), 1.26–1.31 (m, 4H) LC-MS: *m/z* = 485 [M + H, ³⁵Cl]⁺, 487 [M + H, ³⁷Cl]⁺.

2-(3,4-Dichlorophenoxy)-N-[(1*r*,4*r*)-4-[2-(3,4-dichlorophenoxy)acetamido]cyclohexyl] acetamide (ISRIB-A15)



To a solution of (1*r*,4*r*)-cyclohexane-1,4-diamine (0.025 g, 0.2 mmol) in *N,N*-dimethylformamide (1 ml) were added 3,4-dichlorophenoxyacetic acid (0.097 g, 0.4 mmol), 1-[bis(dimethylamino)methylene]-1*H*-1,2,3-triazolo[4,5-*b*]pyridinium 3-oxid hexafluorophosphate (0.175 g, 0.5 mmol) and *N,N*-diisopropylethylamine (0.153 ml, 0.9 mmol). The reaction mixture was subjected to conditions described in procedure C to obtain 107 mg (94%) of the title compound as a cream colored solid. ¹H NMR (400 MHz, CDCl₃) δ 7.37 (d, *J* = 8.8 Hz, 2H), 7.04 (s, 2H), 6.78 (d, *J* = 8.8 Hz, 2H), 6.26 (d, *J* = 8.1 Hz, 2H), 4.42 (s, 4H), 3.85 (br. s, 2H), 2.05 (d, *J* = 6 Hz, 4H), 1.31–1.39 (m, 4H); LC-MS: *m/z* = 519 [M + H, 35Cl]⁺, 521 [M + H, 37Cl]⁺.

2-(4-Chloro-3-fluorophenoxy)-N-[(1*r*,4*r*)-4-[2-(4-chlorophenoxy)acetamido]cyclohexyl] acetamide (ISRIB-A16)

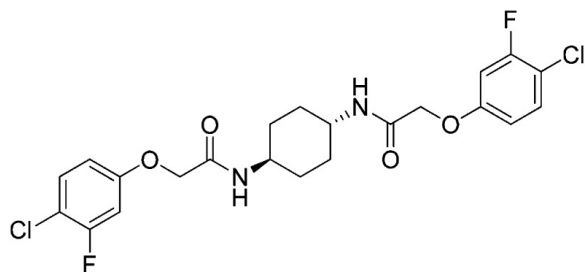


Step 1: To a cooled solution (0°C) of (1r,4r)-4-[2-(4-chlorophenoxy)acetamido]cyclohexan-1-aminium trifluoroacetate (0.550 g, 1.4 mmol) in THF and N,N-diisopropylethylamine (0.966 ml, 5.5 mmol) slowly added chloroacetyl chloride (0.121 ml, 1.5 mmol). The mixture was stirred at ambient temperature for 20 min. The reaction mixture was diluted in dichloromethane, washed with 0.1 N hydrochloric acid, water and brine. The organic layer was dried over magnesium sulfate, filtered and concentrated in a rotary evaporator to obtain about 430 mg of crude 2-(4-chlorophenoxy)-N-[(1r,4r)-4-(2-chloroacetamido)cyclohexyl]acetamide that was used without further purification.

Step 2: To a suspension of 2-(4-chlorophenoxy)-N-[(1r,4r)-4-(2-chloroacetamido)cyclohexyl]acetamide (0.036 g, 0.1 mmol) and 4-chloro-3-fluorophenol (0.015 g, 0.1 mmol) in acetone (1.0 ml), added potassium carbonate (0.021 g, 0.2 mmol) and stirred at 120°C in the microwave reactor for 20 min. The reaction mixture was concentrated down and suspended in water (10 ml). The mixture was vigorously vortexed then centrifuged, and the water was decanted. This washing protocol was repeated with water and then with diethyl ether (10 ml). The wet solid was dissolved in dichloromethane (10 ml) and dried over anhydrous magnesium sulfate. The solids were removed by filtration, and the filtrate was concentrated by rotary evaporation to afford 28 mg (60%) of the title compound as a tan solid. ¹H NMR (400 MHz, DMSO-d₆) δ 7.9 (t, *J* = 8.9 Hz, 2H), 7.46 (t, *J* = 8.9 Hz, 1H), 7.31 (d, *J* = 9 Hz, 2H), 7.03 (dd, *J* =

11.4, 2.7 Hz, 1H), 6.94 (d, $J = 9$ Hz, 2H), 6.81 (dd, $J = 8.5, 2.3$ Hz, 1H), 4.46 (s, 2H), 4.42 (s, 2H), 1.74 (d, $J = 6.2$ Hz, 4H), 1.29–1.35(m, 4H) LC-MS: $m/z = 469$ [M + H, ^{35}Cl]+, 471 [M + H, ^{37}Cl]+.

2-(4-Chloro-3-fluorophenoxy)-N-[(1*r*,4*r*)-4-[2-(4-chloro-3-fluorophenoxy)acetamido]cyclohexyl]acetamide (ISRIB-A17)



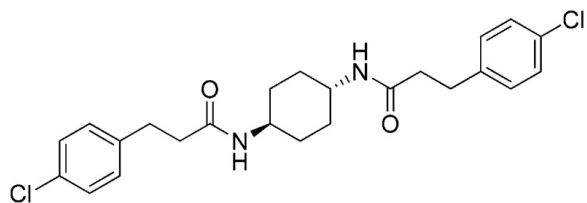
Step 1: To a solution 4-chloro-3-fluorophenol (0.100 g, 0.7 mmol) in N,N-dimethylformamide (2 ml), were added potassium carbonate (0.189 g, 1.4 mmol) and tert-butyl bromoacetate (0.111 ml, 0.8 mmol) and stirred at 65°C for 2 hr. The reaction mixture was diluted with ethyl acetate (10 ml), washed with water (3 × 10 ml) and brine (10 ml). The organic layer was dried over magnesium sulfate and concentrated in a rotary evaporator to obtain 177 mg of tert-butyl 2-(4-chloro-3-fluorophenoxy)acetate as a colorless oil which was used without further purification.

Step 2: To a solution of tert-butyl 2-(4-chloro-3-fluorophenoxy)acetate (177 mg, 0.7 mmol) in methanol/water (4.5 ml, 2:1) was added aqueous 5 N NaOH solution (0.7 ml, 3.5 mmol) and stirred at ambient temperature for an hour. The reaction mixture was concentrated in a rotary evaporator to remove methanol, diluted with water (5 ml) and extracted with ethyl acetate (5 ml). The aqueous layer was adjusted to about pH 2 with 1 N hydrochloric acid and extracted with ethyl acetate (3 × 5 ml). The organic extract was washed with brine (5 ml), dried over magnesium sulfate and

concentrated to obtain 108 mg of 2-(4-chloro-3-fluorophenoxy)acetic acid as a white solid which was used without further purification.

Step 3: To a solution of (1*r*,4*r*)-cyclohexane-1,4-diamine (0.02 g, 0.2 mmol) in N,N-dimethylformamide (1 ml) were added 2-(4-chloro-3-fluorophenoxy)acetic acid (0.072 g, 0.4 mmol), 1-[bis(dimethylamino)methylene]-1*H*-1,2,3-triazolo[4,5-*b*]pyridinium 3-oxid hexafluorophosphate (0.14 g, 0.4 mmol) and N,N-diisopropylethylamine (0.122 ml, 0.7 mmol). The reaction mixture was subjected to conditions described in procedure C to obtain 85 mg (>95%) of the title compound as a white solid. ¹H NMR (400 MHz, DMSO-*d*₆) δ 7.23–7.28 (m, 2H), 6.72 (d, *J* = 8 Hz, 2H), 6.61–6.64 (m, 4H), 4.36 (s, 4H), 3.56 (m, 2H), 1.95 (d, *J* = 6.2 Hz, 4H), 1.28–1.33 (m, 4H); LC-MS: *m/z* = 487 [M + H, ³⁵Cl]⁺, 489 [M + H, ³⁷Cl]⁺.

3-(4-Chlorophenyl)-N-[(1*r*,4*r*)-4-[3-(4-chlorophenyl)propanamido]cyclohexyl]propanamide (ISRIB-A18)



To a solution 3-(4-chlorophenyl)propionic acid (0.129 g, 0.7 mmol) in N,N-dimethylformamide (1.0 ml) were sequentially added 1-hydroxybenzotriazole hydrate (0.094 g, 0.7 mmol), 1-(3-dimethylaminopropyl)-3-ethylcarbodiimide hydrochloride (0.14 g, 0.7 mmol), (1*r*,4*r*)-cyclohexane-1,4-diamine (0.04 g, 0.35 mmol) and N,N-diisopropylethylamine (0.372 ml, 2.1 mmol). The reaction mixture was stirred at 52°C for 18 hr and then subjected to conditions described in procedure B to afford 103 mg (66%) of the title compound. ¹H NMR (400 MHz,

DMSO-d6) δ 7.65 (d, $J = 7.5$ Hz, 2H), 7.28 (d, $J = 8.1$ Hz, 4H), 7.17–7.19 (m, 4H), 3.41 (br.s, 2H), 2.73–2.76 (m, 4H), 2.26–2.30 (m, 4H), 1.66–1.68 (m, 4H), 1.10–1.12 (m, 4H) LC-MS: $m/z = 447$ [M + H, ^{35}Cl]+, 449 [M + H, ^{37}Cl]+.

Acknowledgements

We are indebted to Dr. Shiva Malek (Genentech) for suggesting the use of thermodenaturation to monitor ligand-target engagement. We thank Margaret Elvekrog for her technical advice and Diego Acosta-Alvear for reagents, and Jason Gestwicki for invaluable advice on the ISRIB SAR.

REFERENCES

- Baleriola J, Walker CA, Jean YY, Crary JF, Troy CM, Nagy PL, Hengst U. Axonally synthesized ATF4 transmits a neurodegenerative signal across brain regions. *Cell*. 2014;158:1159–1172. doi: 10.1016/j.cell.2014.07.001.
- Bassik MC, Kampmann M, Lebbink RJ, Wang S, Hein MY, Poser I, Weibezahn J, Horlbeck MA, Chen S, Mann M, Hyman AA, Leproust EM, McManus MT, Weissman JS. A systematic mammalian genetic interaction map reveals pathways underlying ricin susceptibility. *Cell*. 2013;152:909–922. doi: 10.1016/j.cell.2013.01.030.
- Bogorad AM, Xia B, Sandor DG, Mamonov AB, Cafarella TR, Jehle S, Vajda S, Kozakov D, Marintchev A. Insights into the architecture of the eIF2B $\alpha/\beta/\delta$ regulatory subcomplex. *Biochemistry*. 2014;53:3432–3445. doi: 10.1021/bi500346u.
- Borck G, Shin BS, Stiller B, Mimouni-Bloch A, Thiele H, Kim JR, Thakur M, Skinner C, Aschenbach L, Smirin-Yosef P, Har-Zahav A, Nürnberg G, Altmüller J, Frommolt P, Hofmann K, Konen O, Nürnberg P, Munnich A, Schwartz CE, Gothelf D, Colleaux L, Dever TE, Kubisch C, Basel-Vanagaite L. eIF2 γ mutation that disrupts eIF2 complex integrity links intellectual disability to impaired translation initiation. *Molecular Cell*. 2012;48:641–646. doi: 10.1016/j.molcel.2012.09.005.
- Chen A, Muzzio IA, Malleret G, Bartsch D, Verbitsky M, Pavlidis P, Yonan AL, Vronskaya S, Grody MB, Cepeda I, Gilliam TC, Kandel ER. Inducible enhancement of memory storage and synaptic plasticity in transgenic mice expressing an inhibitor of ATF4 (CREB-2) and C/EBP proteins. *Neuron*. 2003;39:655–669. doi: 10.1016/S0896-6273(03)00501-4.

- Cox J, Mann M. MaxQuant enables high peptide identification rates, individualized p.p.b.-range mass accuracies and proteome-wide protein quantification. *Nature Biotechnology*. 2008;26:1367–1372. doi: 10.1038/nbt.1511.
- Dev K, Qiu H, Dong J, Zhang F, Barthlme D, Hinnebusch AG. The beta/Gcd7 subunit of eukaryotic translation initiation factor 2B (eIF2B), a guanine nucleotide exchange factor, is crucial for binding eIF2 in vivo. *Molecular and Cellular Biology*. 2010;30:5218–5233. doi: 10.1128/MCB.00265-10.
- Di Prisco GV, Huang W, Buffington SA, Hsu CC, Bonnen PE, Placzek AN, Sidrauski C, Krnjević K, Kaufman RJ, Walter P, Costa-Mattioli M. Translational control of mGluR-dependent long-term depression and object-place learning by eIF2 α . *Nature Neuroscience*. 2014;17:1073–1082. doi: 10.1038/nn.3754.
- Fogli A, Boespflug-Tanguy O. The large spectrum of eIF2B-related diseases. *Biochemical Society Transactions*. 2006;34:22–29. doi: 10.1042/BST20060022.
- Fraser CS, Berry KE, Hershey JW, Doudna JA. eIF3j is located in the decoding center of the human 40S ribosomal subunit. *Molecular Cell*. 2007;26:811–819. doi: 10.1016/j.molcel.2007.05.019.
- Gordiyenko Y, Schmidt C, Jennings MD, Matak-Vinkovic D, Pavitt GD, Robinson CV. eIF2B is a decameric guanine nucleotide exchange factor with a $\gamma_2\epsilon_2$ tetrameric core. *Nature Communications*. 2014;5:3902. doi: 10.1038/ncomms4902.
- Harding HP, Novoa I, Zhang Y, Zeng H, Wek R, Schapira M, Ron D. Regulated translation initiation controls stress-induced gene expression in mammalian cells. *Molecular Cell*. 2000;6:1099–1108. doi: 10.1016/S1097-2765(00)00108-8.

Harding HP, Zhang Y, Zeng H, Novoa I, Lu PD, Calfon M, Sadri N, Yun C, Popko B, Paules R, Stojdl DF, Bell JC, Hettmann T, Leiden JM, Ron D. An integrated stress response regulates amino acid metabolism and resistance to oxidative stress. *Molecular Cell*. 2003;11:619–633. doi: 10.1016/S1097-2765(03)00105-9.

Hinnebusch AG, Lorsch JR. The mechanism of eukaryotic translation initiation: new insights and challenges. *Cold Spring Harbor Perspectives in Biology*. 2012;4:a011544. doi: 10.1101/cshperspect.a011544.

Jennings MD, Pavitt GD. A new function and complexity for protein translation initiation factor eIF2B. *Cell Cycle*. 2014;13:2660–2665. doi: 10.4161/15384101.2014.948797.

Jennings MD, Pavitt GD. eIF5 has GDI activity necessary for translational control by eIF2 phosphorylation. *Nature*. 2015;465:378–381. doi: 10.1038/nature09003.

Jennings MD, Zhou Y, Mohammad-Qureshi SS, Bennett D, Pavitt GD. eIF2B promotes eIF5 dissociation from eIF2*GDP to facilitate guanine nucleotide exchange for translation initiation. *Genes & Development*. 2013;27:2696–2707. doi: 10.1101/gad.231514.113.

Julien O, Kampmann M, Bassik MC, Zorn JA, Venditto VJ, Shimbo K, Agard NJ, Shimada K, Rheingold AL, Stockwell BR, Weissman JS, Wells JA. Unraveling the mechanism of cell death induced by chemical fibrils. *Nature Chemical Biology*. 2014;10:969–976. doi: 10.1038/nchembio.1639.

Kampmann M, Bassik MC, Weissman JS. Integrated platform for genome-wide screening and construction of high-density genetic interaction maps in mammalian cells. *Proceedings of the National Academy of Sciences of USA*. 2013;110:E2317–E2326. doi: 10.1073/pnas.1307002110.

- Kampmann M, Bassik MC, Weissman JS. Functional genomics platform for pooled screening and generation of mammalian genetic interaction maps. *Nature Protocols*. 2014;9:1825–1847. doi: 10.1038/nprot.2014.103.
- Kim HJ, Raphael AR, LaDow ES, McGurk L, Weber RA, Trojanowski JQ, Lee VM, Finkbeiner S, Gitler AD, Bonini NM. Therapeutic modulation of eIF2 α phosphorylation rescues TDP-43 toxicity in amyotrophic lateral sclerosis disease models. *Nature Genetics*. 2013;46:152–160. doi: 10.1038/ng.2853.
- Kimball SR, Fabian JR, Pavitt GD, Hinnebusch AG, Jefferson LS. Regulation of guanine nucleotide exchange through phosphorylation of eukaryotic initiation factor eIF2 α . Role of the α - and δ -subunits of eIF2 β . *Journal of Biological Chemistry*. 1998;273:12841–12845. doi: 10.1074/jbc.273.21.12841.
- Krishnamoorthy T, Pavitt GD, Zhang F, Dever TE, Hinnebusch AG. Tight binding of the phosphorylated subunit of initiation factor 2 (eIF2) to the regulatory subunits of guanine nucleotide exchange factor eIF2B is required for inhibition of translation initiation. *Molecular and Cellular Biology*. 2001;21:5018–5030. doi: 10.1128/MCB.21.15.5018-5030.2001.
- Lee YY, Cevallos RC, Jan E. An upstream open reading frame regulates translation of GADD34 during cellular stresses that induce eIF2 phosphorylation. *Journal of Biological Chemistry*. 2009;284:6661–6673. doi: 10.1074/jbc.M806735200.
- Leegwater PA, Vermeulen G, Könst AA, Naidu S, Mulders J, Visser A, Kersbergen P, Mobach D, Fonds D, van Berkel CG, Lemmers RJ, Frants RR, Oudejans CB, Schutgens RB, Pronk JC, van der Knaap MS. Subunits of the translation initiation factor eIF2B are mutant in leukoencephalopathy with vanishing white matter. *Nature Genetics*. 2001;29:383–388. doi: 10.1038/ng764.

- Leitman J, Barak B, Benyair R, Shenkman M, Ashery U, Hartl FU, Lederkremer GZ. ER stress-induced eIF2-alpha phosphorylation underlies sensitivity of striatal neurons to pathogenic huntingtin. *PLOS ONE*. 2014;9:e90803. doi: 10.1371/journal.pone.0090803.
- Li W, Wang X, van der Knaap MS, Proud CG. Mutations linked to leukoencephalopathy with vanishing white matter impair the function of the eukaryotic initiation factor 2B complex in diverse ways. *Molecular and Cellular Biology*. 2004;24:3295–3306. doi: 10.1128/MCB.24.8.3295-3306.2004.
- Lu PD, Harding HP, Ron D. Translation reinitiation at alternative open reading frames regulates gene expression in an integrated stress response. *The Journal of Cell Biology*. 2004;167:27–33. doi: 10.1083/jcb.200408003.
- Ma T, Trinh MA, Wexler AJ, Bourbon C, Gatti E, Pierre P, Cavener DR, Klann E. Suppression of eIF2 α kinases alleviates Alzheimer's disease-related plasticity and memory deficits. *Nature Neuroscience*. 2013;16:1299–1305. doi: 10.1038/nn.3486.
- Martin L, Kimball SR, Gardner LB. Regulation of the unfolded protein response by eIF2B Isoforms. *Journal of Biological Chemistry*. 2010;285:31944–31953. doi: 10.1074/jbc.M110.153148.
- Matheny CJ, Wei MC, Bassik MC, Donnelly AJ, Kampmann M, Iwasaki M, Piloto O, Solow-Cordero DE, Bouley DM, Rau R, Brown P, McManus MT, Weissman JS, Cleary ML. Next-generation NAMPT inhibitors identified by sequential high-throughput phenotypic chemical and functional genomic screens. *Chemistry & Biology*. 2013;20:1352–1363. doi: 10.1016/j.chembiol.2013.09.014.

- Martinez Molina DM, Jafari R, Ignatushchenko M, Seki T, Larsson EA, Dan C, Sreekumar L, Cao Y, Nordlund P. Monitoring drug target engagement in cells and tissues using the cellular thermal shift assay. *Science*. 2013;341:84–87. doi: 10.1126/science.1233606.
- Moreno JA, Halliday M, Molloy C, Radford H, Verity N, Axten JM, Ortori CA, Willis AE, Fischer PM, Barrett DA, Mallucci GR. Oral treatment targeting the unfolded protein response prevents neurodegeneration and clinical disease in prion-infected mice. *Science Translational Medicine*. 2013;5:206ra138. doi: 10.1126/scitranslmed.3006767.
- Moreno JA, Radford H, Peretti D, Steinert JR, Verity N, Martin MG, Halliday M, Morgan J, Dinsdale D, Ortori CA, Barrett DA, Tsaytler P, Bertolotti A, Willis AE, Bushell M, Mallucci GR. Sustained translational repression by eIF2 α -P mediates prion neurodegeneration. *Nature*. 2012;485:507–511. doi: 10.1038/nature11058.
- Nadif Kasri N, Nakano-Kobayashi A, Van Aelst L. Rapid synthesis of the X-linked mental retardation protein OPHN1 mediates mGluR-dependent LTD through interaction with the endocytic machinery. *Neuron*. 2011;72:300–315. doi: 10.1016/j.neuron.2011.09.001.
- Novoa I, Zeng H, Harding HP, Ron D. Feedback inhibition of the unfolded protein response by GADD34-mediated dephosphorylation of eIF2 α . *The Journal of Cell Biology*. 2001;153:1011–1022. doi: 10.1083/jcb.153.5.1011.
- Oldfield S, Proud CG. Purification, phosphorylation and control of the guanine-nucleotide-exchange factor from rabbit reticulocyte lysates. *European Journal of Biochemistry*. 1992;208:73–81. doi: 10.1111/j.1432-1033.1992.tb17160.x.
- Palam LR, Baird TD, Wek RC. Phosphorylation of eIF2 facilitates ribosomal bypass of an inhibitory upstream ORF to enhance CHOP translation. *The Journal of Biological Chemistry*. 2011;286:10939–10949. doi: 10.1074/jbc.M110.216093.

- Pavitt GD, Yang W, Hinnebusch AG. Homologous segments in three subunits of the guanine nucleotide exchange factor eIF2B mediate translational regulation by phosphorylation of eIF2. *Molecular and Cellular Biology*. 1997;17:1298–1313.
- Ramage HR, Kumar GR, Verschueren E, Johnson JR, Von Dollen J, Johnson T, Newton B, Shah P, Horner J, Krogan NJ, Ott M. A combined proteomics/genomics approach links hepatitis C virus infection with nonsense-mediated mRNA decay. *Molecular Cell*. 2015;57:329–340. doi: 10.1016/j.molcel.2014.12.028.
- Roy B, Vaughn JN, Kim BH, Zhou F, Gilchrist MA, Von Armin AG. The h subunit of eIF3 promotes reinitiation competence during translation of mRNAs harboring upstream open reading frames. *RNA*. 2010;16:748–761. doi: 10.1261/rna.2056010.
- Sekine Y, Zyryanova A, Crespillo-Casado A, Fisher PM, Harding HP, Ron D. Mutations in translation initiation factor identify the target of a memory-enhancing compound. *Science Express*. 2015 doi: 10.1126/science.aaa6986.
- Sidrauski C, Acosta-Alvear D, Khoutorsky A, Vedantham P, Hearn BR, Li H, Gamache K, Gallagher CM, Ang KK, Wilson C, Okreglak V, Ashkenazi A, Hann B, Nader K, Arkin MR, Renslo AR, Sonenberg N, Walter P. Pharmacological brake-release of mRNA translation enhances cognitive memory. *eLife*. 2013;2:e00498. doi: 10.7554/eLife.00498.
- Sidrauski C, McGeachy AM, Ingolia NT, Walter P. The small molecule ISRIB reverses the effects of eIF2 α phosphorylation on translation and stress granule assembly. *eLife*. 2015;4:e05033. doi: 10.7554/eLife.05033.
- Szamecz B, Rutkai E, Cuchalová L, Munzarová V, Herrmannová A, Nielsen KH, Burela L, Hinnebusch AG, Valášek L. eIF3a cooperates with sequences 5' of uORF1 to promote

- resumption of scanning by post-termination ribosomes for reinitiation on GCN4. *Genes & Development*. 2008;22:2414–2525. doi: 10.1101/gad.480508.
- Sokabe M, Fraser CS, Hershey JW. The human translation initiation multi-factor complex promotes methionyl-tRNAⁱ binding to the 40S ribosomal subunit. *Nucleic Acids Research*. 2012;40:905–913. doi: 10.1093/nar/gkr772.
- Vattem KM, Wek RC. Reinitiation involving upstream ORFs regulates ATF4 mRNA translation in mammalian cells. *Proceedings of the National Academy of Sciences of USA*. 2004;101:11269–11274. doi: 10.1073/pnas.0400541101.
- Ventura A, Meissner A, Dillon CP, McManus M, Sharp PA, Van Parijs L, Jaenisch R, Jacks T. Cre-lox-regulated conditional RNA interference from transgenes. *Proceedings of the National Academy of Sciences of USA*. 2004;101:10380–10385. doi: 10.1073/pnas.0403954101.
- Wang G, Han T, Nijhawan D, Theodoropoulos P, Naidoo J, Yadavalli S, Mirzaei H, Pieper AA, Ready JM, McKnight SL. P7C3 neuroprotective chemicals function by activating the rate-limiting enzyme in NAD salvage. *Cell*. 2014;158:1324–1334. doi: 10.1016/j.cell.2014.07.040.
- Wek RC, Jiang HY, Anthony TG. Coping with stress: eIF2 kinases and translational control. *Biochemical Society Transactions*. 2006;34:7–11. doi: 10.1042/BST20060007.
- Williams DD, Price NT, Loughlin AJ, Proud CG. Characterization of the mammalian initiation factor eIF2B complex as a GDP dissociation stimulator protein. *Journal of Biological Chemistry*. 2001;276:24697–24703. doi: 10.1074/jbc.M011788200.
- Wiseman RL, Zhang Y, Lee KP, Harding HP, Haynes CM, Price J, Sicheri F, Ron D. Flavonol activation defines an unanticipated ligand-binding site in the kinase-RNase domain of IRE1. *Molecular Cell*. 2010;38:291–304. doi: 10.1016/j.molcel.2010.04.001.

Wortham NC, Martinez M, Gordiyenko Y, Robinson CV, Proud CG. Analysis of the subunit organization of the eIF2B complex reveals new insights into its structure and regulation. *FASEB Journal*. 2014;28:2225–2237. doi: 10.1096/fj.13-243329.

Ye J, Kumanova M, Hart LS, Sloane K, Zhang H, De Panis DN, Bobrovnikova-Marjon E, Diehl JA, Ron D, Koumenis C. The GCN2-ATF4 pathway is critical for tumour cell survival and proliferation in response to nutrient deprivation. *The EMBO Journal*. 2010;29:2082–2096. doi: 10.1038/emboj.2010.81.

Zorn JA, Wells JA. Turning enzymes ON with small molecules. *Nature Chemical Biology*. 2010;6:179–188. doi: 10.1038/nchembio.318.

Chapter 2

**Structure of the nucleotide exchange factor eIF2B reveals
mechanism of memory-enhancing molecule**

**Structure of the nucleotide exchange factor eIF2B reveals
mechanism of memory-enhancing molecule**

Jordan C. Tsai^{1,2,†}, Lakshmi E. Miller-Vedam^{2,4,†}, Aditya A. Anand^{1,2,†}, Priyadarshini Jaishankar³,
Henry C. Nguyen^{2,4}, Adam R. Renslo³, Adam Frost^{2,4,*}, Peter Walter^{1,2,*}

¹Howard Hughes Medical Institute, University of California at San Francisco

²Department of Biochemistry and Biophysics, University of California at San Francisco

³Department of Pharmaceutical Chemistry, and Small Molecule Discovery Center, University of California at San Francisco

⁴Chan Zuckerberg Biohub, San Francisco, CA, USA

†The first three authors contributed equally to this work

This work was first submitted to bioRxiv as a preprint at doi.org/10.1101/222257

ABSTRACT

Regulation by the integrated stress response (ISR) converges on the phosphorylation of translation initiation factor eIF2 in response to a variety of stresses. Phosphorylation converts eIF2 from substrate to competitive inhibitor of its dedicated guanine nucleotide exchange factor, eIF2B, inhibiting translation. ISRIB, a drug-like eIF2B activator, reverses the effects of eIF2 phosphorylation, and enhances cognition and corrects cognitive deficits after brain injury in rodents. To determine its mechanism of action, we solved an atomic-resolution structure of ISRIB bound in a deep cleft within decameric human eIF2B by electron cryo-microscopy. Formation of fully active, decameric eIF2B holoenzyme depended on the assembly of two identical tetrameric subcomplexes, and ISRIB promoted this step by cross-bridging a central symmetry interface. Thus, regulation of eIF2B assembly emerges as a rheostat for eIF2B activity that tunes translation during the ISR and that can be further modulated by ISRIB.

INTRODUCTION

Protein quality control is essential to the maintenance of cellular and organismal health. To prevent the production of deleterious proteins, such as those from invading viruses or those produced in misfolding-prone environments, cells regulate protein synthesis. By arresting or accelerating the cardinal decision of translation initiation, cells effect proteome-wide changes that drive organismal functions, such as development, memory, and immunity (1-3).

A key enzyme in the regulation of protein synthesis is eukaryotic translation initiation factor 2B (eIF2B), a dedicated guanine nucleotide exchange factor (GEF) for translation initiation factor 2 (eIF2). eIF2B is composed of five subunits ($\alpha, \beta, \gamma, \delta, \epsilon$) that assemble into a decamer composed of two copies of each subunit (4-8). The eIF2B ϵ subunit contains the enzyme's catalytic center and associates closely with eIF2B γ (9). Two copies each of the structurally homologous eIF2B α , β , and δ subunits form the regulatory core that modulates eIF2B's catalytic activity (10-12). eIF2B's substrate, eIF2 is composed of three subunits (α, β, γ) and binds methionine initiator tRNA and GTP to form the ternary complex required to initiate translation on AUG start codons. eIF2's γ subunit contains the GTP-binding pocket (as reviewed in (13, 14)).

In response to various inputs, many of which are cell stresses, phosphorylation of eIF2 α at serine 51 converts eIF2 from a substrate for nucleotide exchange to a competitive inhibitor of eIF2B. Phosphorylated eIF2 binds to eIF2B with enhanced affinity, effectively sequestering the limiting eIF2B complex from engaging unphosphorylated eIF2 for nucleotide exchange (10-12). Such inhibition leads to an attenuation of general translation and, paradoxically, the selective translation of stress-responsive mRNAs that contain small upstream open reading frames. This latter set includes mRNAs that encode transcriptional activators such as ATF4 (15, 16). In this way eIF2 phosphorylation elicits an intricate gene expression program. This pathway was termed

the “integrated stress response”, following the discovery of several kinases that all phosphorylate eIF2 α at serine 51 to integrate different physiological signals such as the accumulation of misfolded proteins in the lumen of the endoplasmic reticulum, the accumulation of double-stranded RNA indicative of viral infection, the cell’s redox status, and nutrient availability (17).

We previously identified an ISR inhibitor (ISRIB) that reverses the effects of eIF2 α phosphorylation, restoring translation in stressed cells and blocking translation of ISR-activated mRNAs, such as ATF4 (18, 19). When administered systemically to wild-type rodents, ISRIB enhances cognition, leading to significant improvements in spatial and fear-associated learning (18). This effect relies on translation-dependent remodeling of neuronal synapses (20). eIF2 phosphorylation correlates with diverse neurodegenerative diseases and cancers, as well as normal aging (21-24). In addition, a number of mutations that impair eIF2B activity lead to a neurodegenerative disorder of childhood known as vanishing white matter disease (VWMD) that is marked by cerebellar ataxia, spasticity, hypersensitivity to head trauma and infection, coma and premature death (25). As a well-characterized small molecule with rapid cross-blood-brain barrier equilibration, reasonable bioavailability, and good tolerability in rodent efficacy models, ISRIB and related analogs offer great potential for treating VWMD and a range of other devastating diseases lacking therapeutic options (18, 26). Indeed in rodents, ISRIB entirely reverses cognitive deficits associated with traumatic brain injuries (27) and protects against neurodegeneration (26).

Previous work identified eIF2B as the molecular target of ISRIB (28, 29). ISRIB enhances eIF2B GEF activity three-fold, stabilizes a decameric form of the enzyme when analyzed in high salt conditions, and increases thermostability of eIF2B δ (28). Mutations that render cells insensitive to ISRIB cluster in the N-terminal region of the eIF2B δ subunit (29), and when projected onto the crystal structure of *S. pombe* eIF2B, two of the mutated residues map to its

symmetric interface (8). These data hinted that ISRIB may activate eIF2B by binding near adjacent δ subunits to exert its blunting effects on the ISR. Here we report mechanistic and structural insights into ISRIB's mechanism of action.

RESULTS

ISRIB stabilizes decameric eIF2B, accelerating GEF activity

To investigate the mechanism by which ISRIB enhances the GEF activity of eIF2B, we engineered a recombinant *E. coli* expression system for co-expression of all five subunits of human eIF2B (Fig. 1A). eIF2B purified as a monodisperse complex that sedimented at 13.6S, corresponding to the size of a decamer containing two copies of each subunit (Fig. 1B - AUC, Fig. S1A).

We adapted a fluorescent GDP exchange assay (29), to assess the enzymatic activity of recombinant eIF2B. We purified the substrate, non-phosphorylated human eIF2, from a *S. cerevisiae* expression system genetically edited to lack the only yeast eIF2 kinase (*gcn2Δ*) (30) (Fig. S2A, S2B). First, in a “GDP loading assay” we added fluorescent Bodipy-GDP to GDP-bound eIF2. We observed an eIF2B concentration-dependent increase in fluorescence corresponding to the dislodging of bound GDP and subsequent binding of Bodipy-GDP to eIF2 (Fig. S2C, Fig. S2D). Second, in a “GDP unloading assay”, we chased with a 1000-fold excess of unlabeled GDP and measured a decrease in fluorescence corresponding to the eIF2B-catalyzed dissociation of Bodipy-GDP from eIF2 (Fig. S2E). GEF activities were fit to a single-exponential (Fig. S2F) for calculating the reported k_{obs} values. Titrating substrate concentration to saturating levels in GDP unloading assays yielded K_m and k_{cat} values similar to those of eIF2B previously purified from mammalian cells (Fig. 1C) (31).

To investigate how ISRIB activates eIF2B, we fixed eIF2B and eIF2 in a multi-turnover regime at concentrations of 10 nM and 1 μM , respectively. Under these conditions, the eIF2 is subsaturating given its K_m of 1.5 μM (Fig. 1C). Previously, a three-fold stimulation of nucleotide exchange by ISRIB was seen under similar conditions (28). Surprisingly, ISRIB only marginally

activated the recombinant eIF2B decamer by 1.2-fold (Fig. 1D, (- ISRIB): $k_{\text{obs}} = 0.17 \pm 0.006 \text{ min}^{-1}$ and (+ ISRIB): $k_{\text{obs}} = 0.21 \pm 0.005 \text{ min}^{-1}$).

ISRIB stabilizes eIF2B decamers in lysates of HEK293T cells (28), suggesting a role during assembly of the active complex. To test this notion and its implications for ISRIB's mechanism of action, we purified eIF2B in the presence or absence of ISRIB. Under both conditions we obtained the fully assembled decamer (Fig. 1E, peak 3); however, in the absence of ISRIB we also obtained a partially assembled complex lacking the α subunit that eluted from the anion exchange column at a lower ionic strength (Fig. 1E, peak 2). These data suggest that ISRIB enhances the stability of the decamer. To test this idea, we expressed eIF2B($\beta\gamma\delta\epsilon$) and eIF2B α separately (Fig. S1B, Fig. S1C). Surprisingly, eIF2B($\beta\gamma\delta\epsilon$) purified as a heterotetramer, as determined by analytical ultracentrifugation (Fig. S1D), while eIF2B α purified as a homodimer, as previously observed (Fig. S1E) (6). We then combined eIF2B($\beta\gamma\delta\epsilon$) and eIF2B(α_2) under stringent conditions of elevated ionic strength (400 mM) to assess ISRIB's contribution to the stability of the decameric complex. When analyzed by velocity sedimentation in the absence of ISRIB, eIF2B($\beta\gamma\delta\epsilon$) sedimented as a tetramer (peak fractions 6-7), whereas eIF2B(α_2) peaked in fraction 4 (Fig. 1F, upper panel). By contrast, in the presence of ISRIB, eIF2B($\beta\gamma\delta\epsilon$) and eIF2B(α_2) sedimented together as a higher molecular weight complex deeper in the gradient (peak fractions 7-9) (Fig. 1F, lower panel). As we discuss below, the stabilized decamer peaked in fraction 10 of the gradient, indicating that under these conditions, the decamer partially dissociates during sedimentation. We surmise that dissociation during centrifugation led to the broad sedimentation profiles observed. Thus, ISRIB enhanced the stability of decameric eIF2B.

To understand the interplay between ISRIB binding, eIF2B(α_2) incorporation into the decamer, and GEF activity, we mixed independently purified eIF2B(α_2) and eIF2B($\beta\gamma\delta\epsilon$)

subcomplexes and assayed the combination for GDP unloading. When assayed under these conditions, the specific activity was four-fold reduced when compared to the fully assembled decamer (compare Fig. 1D and 1G, $k_{\text{obs}} = 0.17 \pm 0.006 \text{ min}^{-1}$ and $0.04 \pm 0.009 \text{ min}^{-1}$). Importantly, the addition of ISRIB restored GEF activity three-fold toward the level of fully assembled decamer ($k_{\text{obs}} = 0.11 \pm 0.002 \text{ min}^{-1}$) (Fig. 1G), suggesting that ISRIB's activity reflects enhanced decamer stability.

Using the GDP loading assay, we found that eIF2B activity was reduced profoundly ($k_{\text{obs}} = 0.01 \pm 0.007 \text{ min}^{-1}$) in the absence of eIF2B(α_2) (Fig. 1H), as previously reported (32, 33). Interestingly, ISRIB still activated eIF2B($\beta\gamma\delta\epsilon$) (Fig. 1I, $k_{\text{obs}} = 0.04 \pm 0.003 \text{ min}^{-1}$), indicating that ISRIB can enhance GEF activity independent of eIF2B(α_2) incorporation into the holoenzyme. To reconcile these unexpected findings, we next sought a structural understanding of the ISRIB-stabilized human eIF2B decameric complex.

ISRIB binds in a deep cleft, bridging the two-fold symmetric interface of the eIF2B decamer

We determined an atomic resolution structure of eIF2B bound to ISRIB by electron cryo-microscopy (cryoEM). We classified and refined a single consensus structure from 202,125 particles to an average resolution of 2.8 Å resolution, that varied from 2.7 Å in the stable core to >3.4 Å in the more flexible periphery (Fig. S3). The overall structure bears clear resemblance to the *S. pombe* two-fold symmetric decameric structure determined by X-ray crystallography (8). The symmetry interface comprises contacts between the α , β , and δ subunits, while the γ and ϵ subunits are attached at opposing ends (Fig. 2A-C). As in the *S. pombe* crystal structure, the catalytic HEAT domains of the ϵ subunits were not resolved, indicating their flexible attachment

to the regulatory core. By contrast, densities for the “ear” domains of the γ subunits were resolved, but at a resolution that precluded atomic interpretation (Fig. 2B, Fig. S3-4).

Importantly, we observed a clearly defined density consistent with the dimensions of ISRIB and not attributable to protein bridging the symmetry interface of the decamer (Fig. 2B, Fig. 2D-E, Fig. S5). Modeling suggests that ISRIB binds with its central cyclohexane ring in the expected low-energy chair conformation and with the side chains projecting to the same face of the cyclohexane ring and inserting the distal 4-chlorophenyl rings into deep binding pockets (Fig. 2D-F, Fig. S5). ISRIB’s “U-shaped” conformation may be stabilized by intramolecular N-H---O hydrogen bonding interactions between its amide nitrogen N-H bond and the aryl ether oxygens, possibly explaining why non-ether-linked congeners of ISRIB are much less potent (Fig. S6) (28, 34). The cryoEM density most likely corresponds with an average of at least two energetically equivalent ISRIB conformations related by 180° rotations about both N-C bonds to the cyclohexane ring (both depicted in Fig. 2F and Fig. S4-5). This superposition of two conformers accounts for the apparently symmetric density observed, even though in isolation each individual conformer is pseudo-symmetric (Fig. S5). The multiple observed ISRIB binding modes may contribute to its free energy of binding by providing additional entropic wiggle room.

The N-terminal loop of the δ subunit contributes key residues to the binding pocket, and this loop differs significantly from the ligand-free *S. pombe* structure (8). Residues in this loop are important for ISRIB activity (29), including δ V177 and δ L179, which contribute directly to the hydrophobic surface of the binding pocket (Fig. 2F, Fig. S6). In addition, the δ subunits contribute δ L485 to the hydrophobic wells that accommodate the halogenated benzene rings (Fig. 2F, Fig. S6). The center of the binding site comprises residues from the β subunit, including β N162 and β H188, which lie near ISRIB’s more polar functionality. In particular, one of the two C-H bonds

at the glycolamide α -carbon is oriented perpendicular to the plane of the aromatic histidine ring (Fig. 2F, Fig. S6), suggesting a C-H- π interaction with β H188. Residues on the β subunits also make key contributions to the hydrophobicity of the deep wells, including β V164 and β I190.

Thus, ISRIB enhances incorporation of the α subunit into the decamer despite not making direct contacts with this subunit. Rather, ISRIB stabilizes the symmetry interface of the β - δ core, which in turn favors stable eIF2B(α_2) binding. As such, ISRIB's enhancement of GEF activity derives from its ability to promote higher-order holoenzyme assembly.

Structural model predicts the activity of modified compounds and mutations

To validate the structural model, we synthesized ISRIB analogs bearing a methyl group at the α position of the glycolamide side chains. Two enantiomers, ISRIB-A19(*R,R*) and ISRIB-A19(*S,S*) were prepared (Fig. S7A) based on predicted steric clashes with residue δ L179 for ISRIB-A19(*R,R*) or β H188 for ISRIB-A19(*S,S*) in the ISRIB binding pocket (Fig. 2F, Fig S6). As expected, neither enantiomer enhanced GEF activity in vitro or in cells (Fig. 3A, Fig. S7B), nor did they enhance the stability of purified decameric eIF2B (Fig. S7C). We next engineered eIF2B to accommodate the additional methyl groups on ISRIB-A19(*R,R*) by mutating δ L179 to alanine. We tested the effects of both compounds on eIF2B(δ L179A) by velocity sedimentation and GEF activity. As predicted, ISRIB-A19(*R,R*) stabilized formation of mutant decamers (Fig. 3B) and stimulated nucleotide exchange (Fig. 3C). Treatment with ISRIB-A19(*R,R*) activated eIF2B(δ L179A) approximately three-fold (Fig. 3C, $k_{\text{obs}} = 0.027 \pm 0.001 \text{ min}^{-1}$), a similar fold-activation to eIF2B WT by ISRIB. By contrast and as predicted, ISRIB-A19(*S,S*) failed to activate eIF2B(δ L179A) (Fig. 3C, $k_{\text{obs}} = 0.007 \pm 0.001 \text{ min}^{-1}$). Notably, in the absence of ISRIB analogs, eIF2B(δ L179A) was five-fold less active than eIF2B (compare Fig. 3A and 3C, eIF2B $k_{\text{obs}} = 0.04 \pm 0.009 \text{ min}^{-1}$

and eIF2B(δ L179A) $k_{\text{obs}} = 0.008 \pm 0.002 \text{ min}^{-1}$), identifying δ L179A as a novel hypomorphic mutation and underscoring the importance of this surface for holoenzyme assembly.

We next sought to verify the existence of a putative C-H- π interaction between β H188 and ISRIB by mutating β H188 to alanine. As predicted, ISRIB did not stabilize eIF2B(β H188A) decamers (Fig. 3D-E, Fig. S8). By contrast, mutating β H188 to an aromatic tyrosine or phenylalanine—which are predicted to sustain and likely enhance C-H- π interactions—did not impair ISRIB's activity to stabilize decamers (Fig. 3D, Fig. 3F-G, Fig. S8). Rather, ISRIB stabilized eIF2B(β H188Y) and eIF2B(β H188F) decamers to an even greater extent than wild-type eIF2B decamers (Fig. 3D). Whereas ISRIB-stabilized wild-type eIF2B sedimented with a broad profile, indicating dissociation of the decamer through the course of sedimentation (Fig. 1F, Fig. 3D), ISRIB-stabilized eIF2B(β H188Y) and eIF2B(β H188F) formed a sharp symmetric peak in fraction 10, indicative of enhanced complex integrity through sedimentation, presumably owing to enhanced C-H- π bonding interaction with ISRIB (Fig. 3D, Fig. 3F-G, Fig. S8).

ISRIB induces dimerization of tetrameric eIF2B subcomplexes

Because ISRIB bridges the symmetry interface of the decamer without making direct contacts with eIF2B(α_2), we sought to understand how the small molecule promotes eIF2B(α_2) incorporation into the decamer. We imaged purified eIF2B($\beta\gamma\delta\epsilon$) tetramers in the presence and absence of ISRIB by cryoEM. In the presence of ISRIB, the images revealed a predominant species consistent with an octameric complex of eIF2B lacking the α subunits (Fig. 4A). By contrast, in the absence of ISRIB, the predominant species was consistent with a tetrameric complex divided along the symmetry axis of the octamer (Fig. 4B). In accordance with the ISRIB-dependent stabilization of the decamer by mutations in β H188 to other aromatic residues, β H188F and β H188Y mutants also

stabilized the octamer in high salt conditions (Fig. S9). These images suggest a model in which ISRIB dimerizes eIF2B($\beta\gamma\delta\epsilon$) by “stapling” the tetramers together to form the octameric binding platform for α subunit binding, consistent with the architecture of the ISRIB-bound decamer.

We next substantiated eIF2B($\beta\gamma\delta\epsilon$) dimerization by analytical ultracentrifugation under physiological salt conditions. In the absence of ISRIB, eIF2B($\beta\gamma\delta\epsilon$) sedimented as a predominant 8.0S peak and a minor 11.7S peak, corresponding to eIF2B($\beta\gamma\delta\epsilon$) and eIF2B($\beta\gamma\delta\epsilon$)₂, respectively (Fig. 4C). By contrast, in the presence of ISRIB, we observed a dramatic increase in the 11.7S peak, demonstrating ISRIB’s role in stabilizing the eIF2B($\beta\gamma\delta\epsilon$)₂ octamer. Together with the observation that eIF2B($\beta\gamma\delta\epsilon$) has greater activity in the presence of ISRIB (Fig. 11), these data show the importance of octamer assembly in activating GEF activity.

Dimerization of eIF2B($\beta\gamma\delta\epsilon$) effectively doubles the surface area for eIF2B(α_2) binding, suggesting that the ISRIB-enhanced incorporation of eIF2B(α_2) into the decamer originates from ISRIB’s ability to shift the tetramer/octamer equilibrium. To test this prediction, we combined eIF2B(α_2) and eIF2B($\beta\gamma\delta\epsilon$) in the presence and absence of ISRIB and assessed decamer assembly by analytical ultracentrifugation. Under the high protein concentrations used in these assays, we observed a predominant peak corresponding to the assembled eIF2B decamer at 13.6S both in the presence and absence of ISRIB, together with minor peaks corresponding to unincorporated eIF2B($\beta\gamma\delta\epsilon$) at 8.0S and eIF2B(α_2) at 4.1S (Fig. 4D). Importantly, we did not observe an octamer peak, suggesting the octamer has a high affinity for eIF2B(α_2) and assembles the full decamer under these conditions. Together with the cryoEM images, these data demonstrate that eIF2B(α_2) and ISRIB synergistically promote dimerization of eIF2B($\beta\gamma\delta\epsilon$).

Given that ISRIB binds across the eIF2B($\beta\gamma\delta\epsilon$)₂ interface such that each tetramer contributes half of the ISRIB binding site, we reasoned that high ISRIB concentrations may occupy half-sites

within the tetramers and interfere with octamer formation. Indeed, ISRIB promoted eIF2B($\beta\gamma\delta\epsilon$)₂ assembly at 1 μ M but failed to do so at 10 μ M (Fig. 4E). Similarly, ISRIB stimulated GEF activity of eIF2B($\beta\gamma\delta\epsilon$) at 200 nM but failed to do so at 5 μ M (Fig. 4F). Importantly, the high ISRIB concentrations used in this assay did not reduce GEF activity below that of eIF2B($\beta\gamma\delta\epsilon$), demonstrating that the effect did not result from non-specific enzymatic inhibition.

Loss and gain-of-function dimerization mutants resist or bypass the effects of ISRIB

To visualize the determinants of octamerization, we highlighted the solvent-excluded surface area along the symmetry interface of the β and δ subunits in adjacent tetramers (Fig. 5A-B, light yellow, light blue, green) and labeled the residues of the ISRIB binding pocket on this surface (Fig. 5A-B, gray). The tetramer-tetramer contact residues form a thin strip along each neighboring β and δ subunit. Most of the β subunit residues contact the δ subunit across the symmetry interface, while a small number of residues also cement β - β' contacts. Of these, β H160 and β R228 reside at the junction of β - β' and β - δ' subunits, suggesting that they play key roles in stabilizing the octamer. Accordingly, we observed that mutation of β H160 to aspartic acid, which we predicted would be repulsed by δ D450, completely precluded octamer assembly. Analytical ultracentrifugation of eIF2B($\beta\gamma\delta\epsilon$) containing the β H160D mutation revealed a sharp tetramer peak at 7S both in the absence and presence of ISRIB (Fig. 5C), and ISRIB was unable to enhance GEF activity for this mutant (Fig. 5D). Thus, the effect of this mutation on octamerization cannot be overcome by ISRIB binding, despite the fact that ISRIB binding buries an additional $\sim 11\%$ of solvent-exposed surface area—an increase from 3420 \AA^2 to 3790 \AA^2 —upon stapling of tetramers (Fig. 5A-B).

Serendipitously, we also identified a gain-of-function mutation in eIF2B. We initially engineered a δ L179V mutation alongside the δ L179A mutation used above to accommodate the

methylated analog ISRIB-A19(*R,R*) (Fig. 2F, Fig. S6). To our surprise, we discovered that the predominant species of δ L179V-eIF2B($\beta\gamma\delta\epsilon$) sedimented as a remarkably stable octamer in the absence of ISRIB (Fig. 5E). GEF activity assays revealed that δ L179V-eIF2B($\beta\gamma\delta\epsilon$)₂ was five-fold more active than the wild-type octamers formed in the presence of ISRIB, and was not further activated by ISRIB (compare Fig. 5F and Fig. 1I, eIF2B(δ L179V) $k_{\text{obs}} = 0.027 \pm 0.001 \text{ min}^{-1}$, eIF2B(δ L179V) + ISRIB $k_{\text{obs}} = 0.024 \pm 0.001 \text{ min}^{-1}$, WT + ISRIB $k_{\text{obs}} = 0.005 \pm 0.001 \text{ min}^{-1}$). Together with the ISRIB-bound structure, these mutants indicate that the major contribution of ISRIB to increased GEF activity lies at the step of tetramer dimerization and assembly of the bipartite surface for α subunit homodimer binding (Fig. 6).

DISCUSSION

We determined the structure of human eIF2B at sufficiently high resolution to characterize the binding-site and coordination of a small molecule with therapeutic potential. In concomitant work, Zyryanova et al. report similar findings (49). The atomic model of ISRIB-bound eIF2B reconciles structure-activity-relationships described previously (28, 34), predicted both loss- and gain-of-function mutations, and facilitates the rational design of small molecule modulators of eIF2B activity. The structure provides an intuitive view of how ISRIB activates nucleotide exchange: ISRIB stabilizes the active decameric form of the eIF2B holoenzyme by stapling the constituents together across a 2-fold symmetry axis.

Given that a catalytic residue essential for nucleotide exchange resides in the still unresolved HEAT repeat of the ϵ subunit, how does assembly of the decameric holoenzyme enhance activity? Crosslinking studies suggest that eIF2 binds across the decameric interface, engaging the eIF2B α subunit, and β and δ subunits from opposing tetramers (8). We surmise that decamer assembly creates a composite surface for eIF2 binding that allows the flexibly attached HEAT domain to reach and engage its target. While we consider it likely that the effects of ISRIB binding can be explained by the degree of holoenzyme assembly, additional ligand-induced allosteric changes may also contribute to its activity.

These observations provide a plausible model for ISRIB's ability to ameliorate the inhibitory effects of eIF2 α phosphorylation on ternary complex formation. ISRIB staples tetrameric building blocks together into an octamer, which enhances activity three-fold, and forms a platform for association of the dimeric α subunits. The integrated effect of these sequential steps is an order of magnitude enhancement of activity. The inhibition resulting from a limiting amount of phosphorylated eIF2 would be reduced by the surplus of GEF activity provided by ISRIB. By

contrast, an excess of ISRIB poisoned the assembly reaction by saturating half-binding sites on unassembled tetramers. Thus, within its effective concentration range, ISRIB will enhance ternary complex formation even in unstressed conditions, opening an untapped reservoir of additional enzymatic capacity. We surmise that in vivo these activities are likely to be realized near the equilibrium points of the assembly reactions for the holoenzyme, allowing for ISRIB's observed phenotypic effects. Thus, eIF2B is poised to integrate diverse signals that impact translation initiation. Phosphorylation of eIF2 may be just one of many mechanisms for modulating its activity. Post-translational modifications, expression of other modulatory components, or binding of yet-to-be-identified endogenous ligands to the ISRIB binding pocket or elsewhere are likely to modulate eIF2B activity under varying physiological conditions. Understanding the different modes of regulation of this vital translational control point will be of particular importance in the nervous system where ISRIB has been shown to have a range of effects.

Figure 2-1

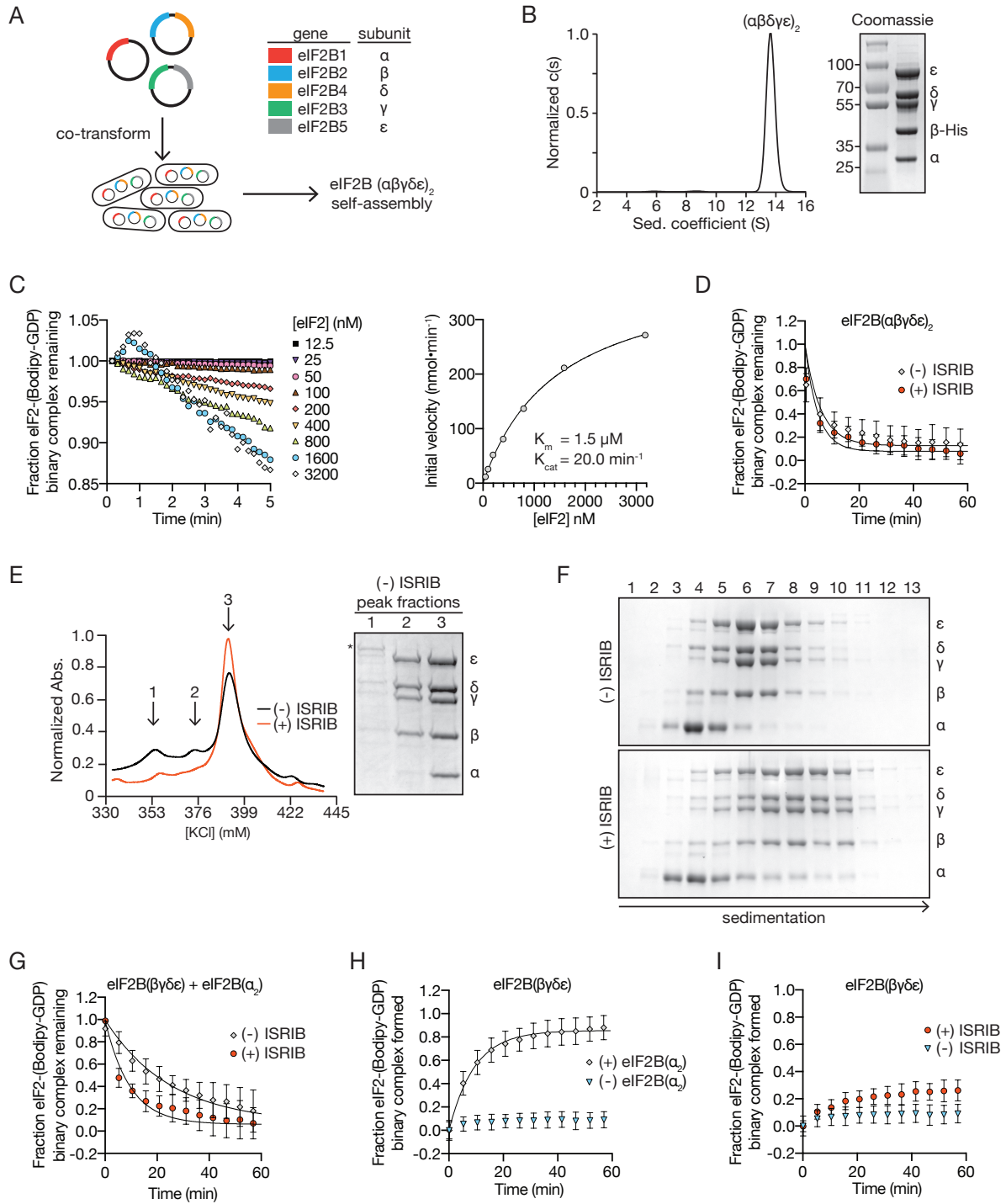
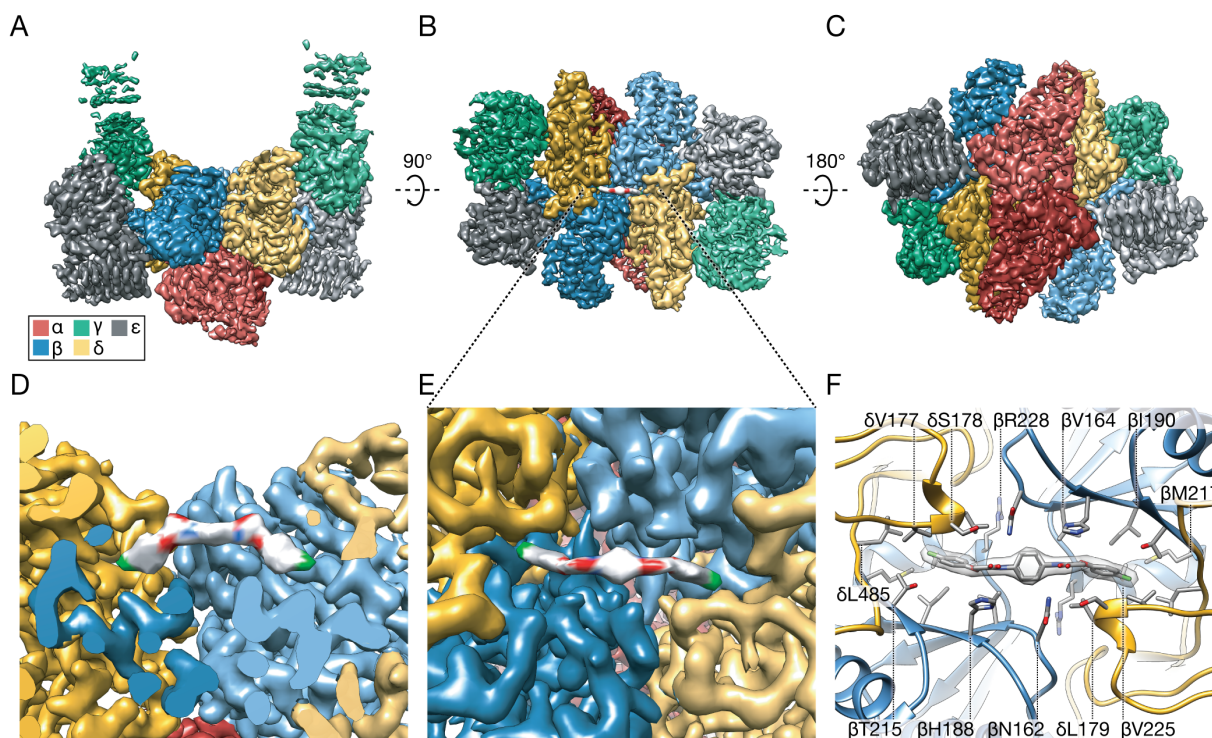


Figure 2-1

ISRIB stabilizes decameric eIF2B, accelerating GEF activity: (A) Schematic diagram for three plasmid expression of all five eIF2B genes in *E. coli*. (B) Characterization of eIF2B($\alpha\beta\gamma\delta\epsilon$)₂ by sedimentation velocity analytical ultracentrifugation and SDS-PAGE followed by Coomassie blue staining. (C) Initial rate of nucleotide exchange (right panel) plotted as a function of substrate concentration. Note that at high eIF2 concentration we reproducibly observed a transient increase in fluorescence that peaked at the 1 min time point (left panel). Such increase was reported previously (29) and remains unexplained. (D) GEF activity of eIF2B($\alpha\beta\gamma\delta\epsilon$)₂ as measured by unloading of fluorescent GDP from eIF2 in the presence and absence of ISRIB. (E) Representative absorbance 280 nm traces from an anion exchange column used in the purification of eIF2B in the presence (red) and absence (black) of ISRIB (n=3). Traces were normalized to total protein eluted in respective runs. Peak fractions from the (-) ISRIB purification were analyzed by SDS-PAGE and Coomassie-stained. eIF2B subunits are labeled (α - ϵ) and an asterisk denotes the presence of a contaminating protein that contributes to peak 1. (F) Stability of eIF2B($\alpha\beta\gamma\delta\epsilon$)₂ was assessed by sedimentation velocity on a 5-20% sucrose gradient in a 400 mM salt buffer. eIF2B($\beta\gamma\delta\epsilon$) and eIF2B(α_2) were combined with and without 500 nM ISRIB. Fractions were analyzed by SDS-PAGE and Coomassie-stained. (G) GEF activity of eIF2B assembled from purified eIF2B($\beta\gamma\delta\epsilon$) and eIF2B(α_2) in the presence and absence of ISRIB. (H) GEF activity of eIF2B($\beta\gamma\delta\epsilon$) in the presence and absence of eIF2B(α_2). (I) GEF activity of eIF2B($\beta\gamma\delta\epsilon$) in the presence and absence of ISRIB.

Figure 2-2



Atomic resolution reconstruction of ISRIB-bound eIF2B: (A-C) Three views of cryoEM density for eIF2B($\alpha\beta\gamma\delta\epsilon$)₂, colored in distinct shades for each subunit copy: red for α , blue for β , green for γ , gold for δ , and gray for ϵ (color code used throughout this manuscript). Density assigned to ISRIB depicted in CPK coloring: oxygens highlighted in red, nitrogens in blue and chlorines in green. The rotational relationships between the views depicted in A, B, and C are indicated. (D) Cross-section of (A), revealing view of the ISRIB binding pocket at the central decamer symmetry interface and density assigned to ISRIB CPK-colored by element. (E) Close-up view of density assigned to ISRIB and its binding pocket in (B) at the intersection of two β and two δ subunits. (F) Two conformers of ISRIB modeled into the density and all residues within a 3.7Å distance from the ligand rendered as sticks.

Figure 2-3

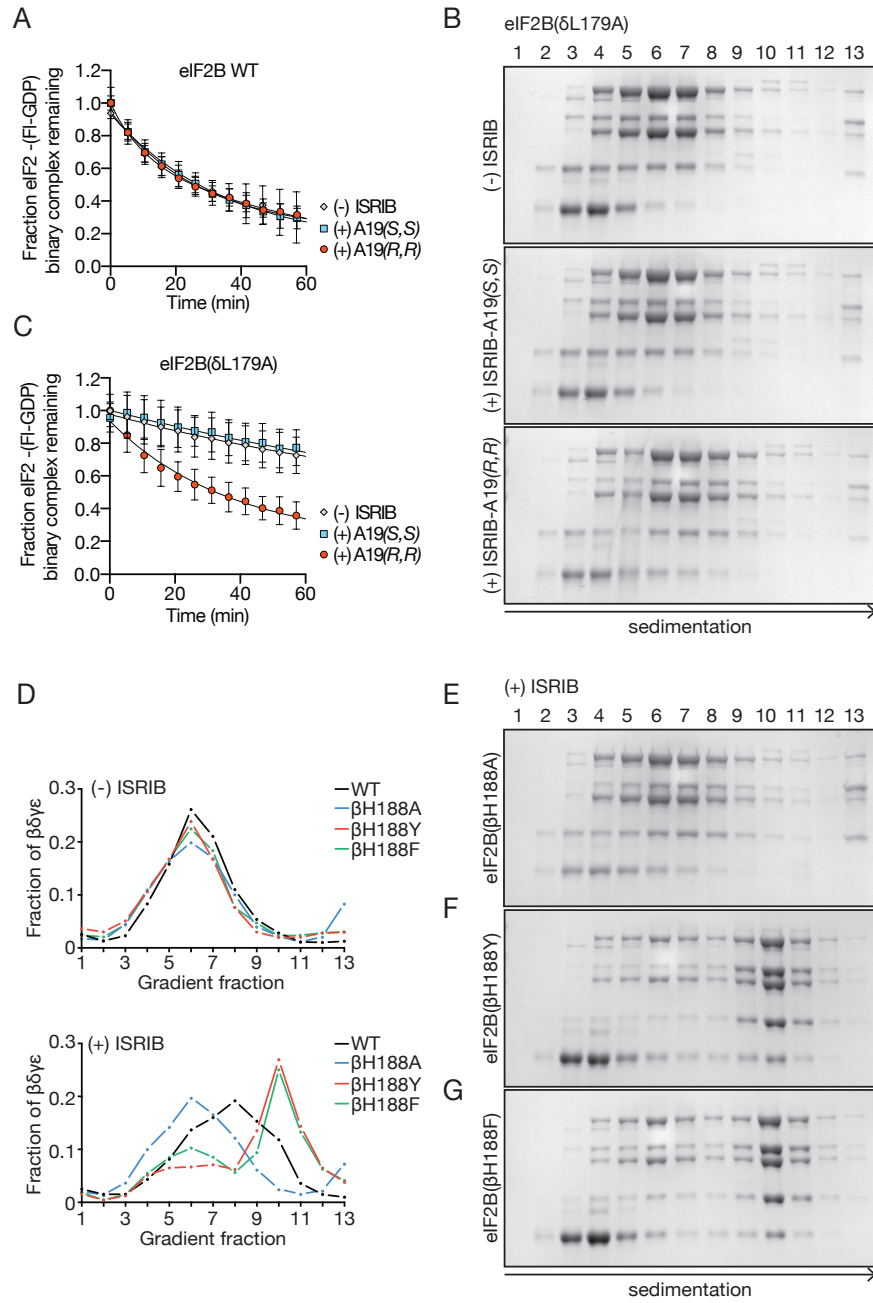
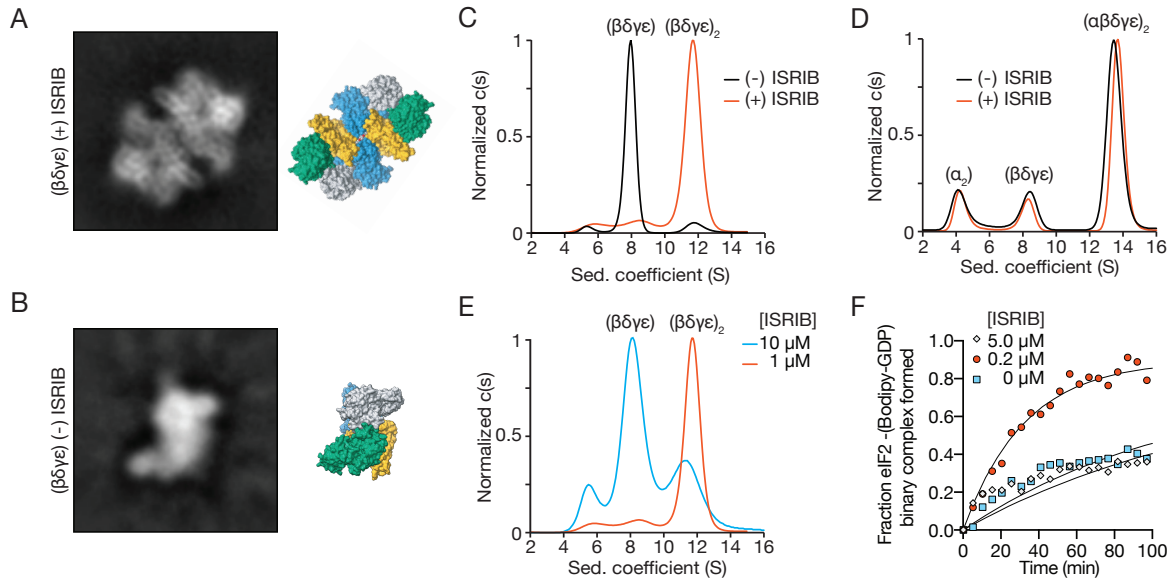


Figure 2-3

eIF2B structure predicts activity of ISRIB analogs: (A) GEF activity of assembled eIF2B($\beta\gamma\delta\epsilon$) and eIF2B(α_2) in the presence and absence of ISRIB-A19(*R,R*) and ISRIB-A19(*S,S*). (B) Stability of decameric eIF2B(δ L179A) in the absence of ISRIB (top), presence of ISRIB-A19(*S,S*) (middle), or presence of ISRIB-A19(*R,R*) (bottom) as assessed by velocity sedimentation on sucrose gradients. (C) eIF2B GEF activity of assembled eIF2B($\beta\gamma\delta\epsilon$) and eIF2B(α_2) containing a δ L179A mutation in the presence and absence of ISRIB-A19(*R,R*) and ISRIB-A19(*S,S*). (D) Quantification of eIF2B decamer stability gradients plotted as fraction of eIF2B($\beta\gamma\delta\epsilon$) present in each of lanes 1-13. eIF2B (for comparison from data shown in Fig. 1F), eIF2B(β H188A), eIF2B(β H188Y), eIF2B(β H188F) gradients are plotted in the presence (bottom panel) and absence (top panel) of 500 nM ISRIB. (E, F, G) Stability of decameric eIF2B(β H188A), eIF2B(β H188Y), and eIF2B(β H188F) in the presence of ISRIB as assessed by velocity sedimentation on sucrose gradients.

Figure 2-4



ISRIB induces dimerization of tetrameric eIF2B subcomplexes: The most abundant 2D class averages from cryoEM imaging of eIF2B($\beta\gamma\delta\epsilon$) in the presence (A) and absence (B) of ISRIB. (C) Characterization of eIF2B($\beta\gamma\delta\epsilon$) by sedimentation velocity analytical ultracentrifugation. eIF2B($\beta\gamma\delta\epsilon$) (1 μM) was analyzed in the presence and absence of 1 μM ISRIB. (D) Mixture of 1 μM eIF2B($\beta\gamma\delta\epsilon$) and 500 nM eIF2B(α_2) characterized by analytical ultracentrifugation in the presence and absence of 1 μM ISRIB. (E) eIF2B($\beta\gamma\delta\epsilon$) (1 μM) characterized by analytical ultracentrifugation in the presence of 1 μM or 10 μM ISRIB. (F) GEF activity of eIF2B($\beta\gamma\delta\epsilon$), here at a higher 100nM concentration to facilitate comparison of 0, 0.2, and 5 μM ISRIB.

Figure 2-5

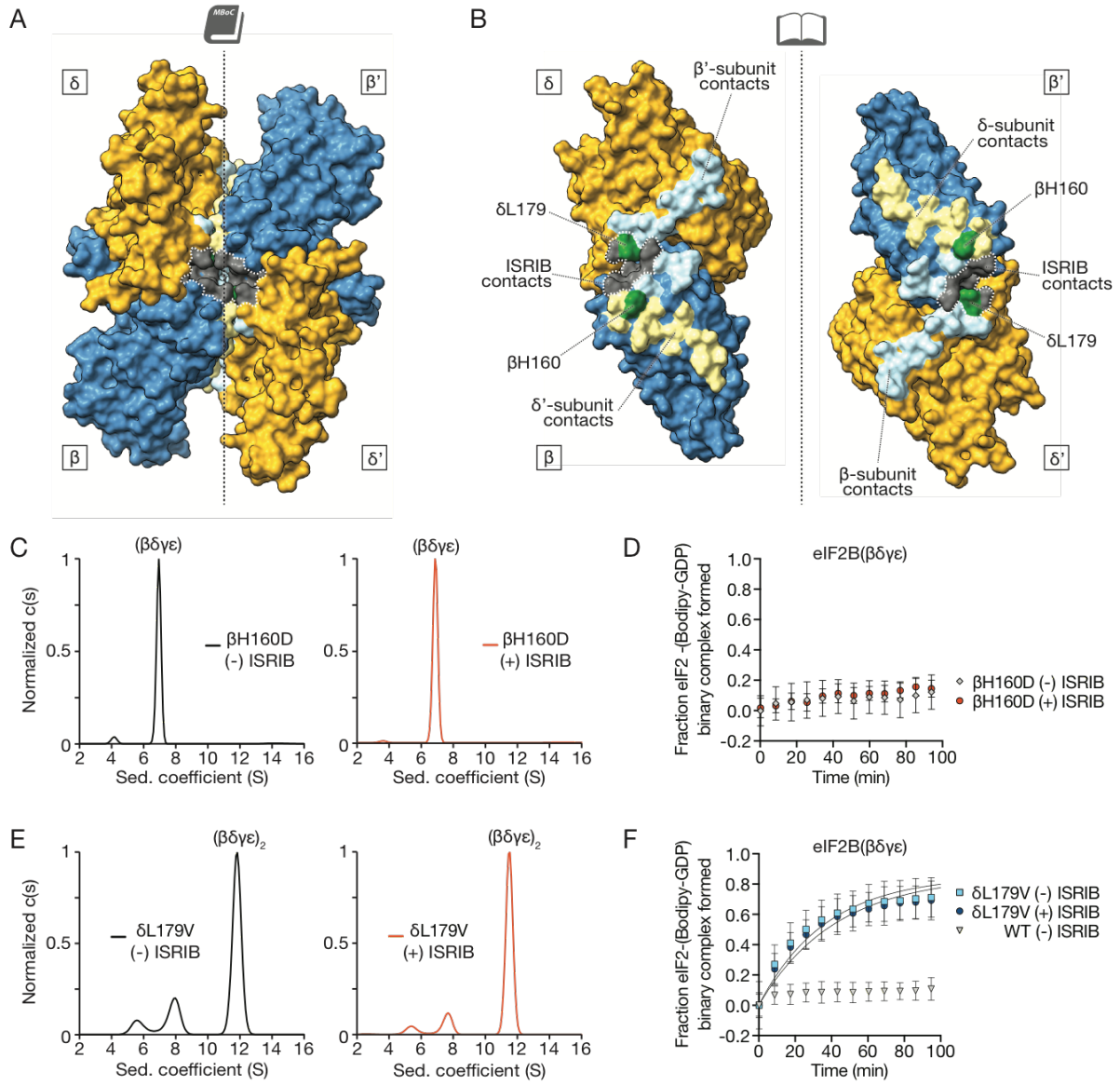
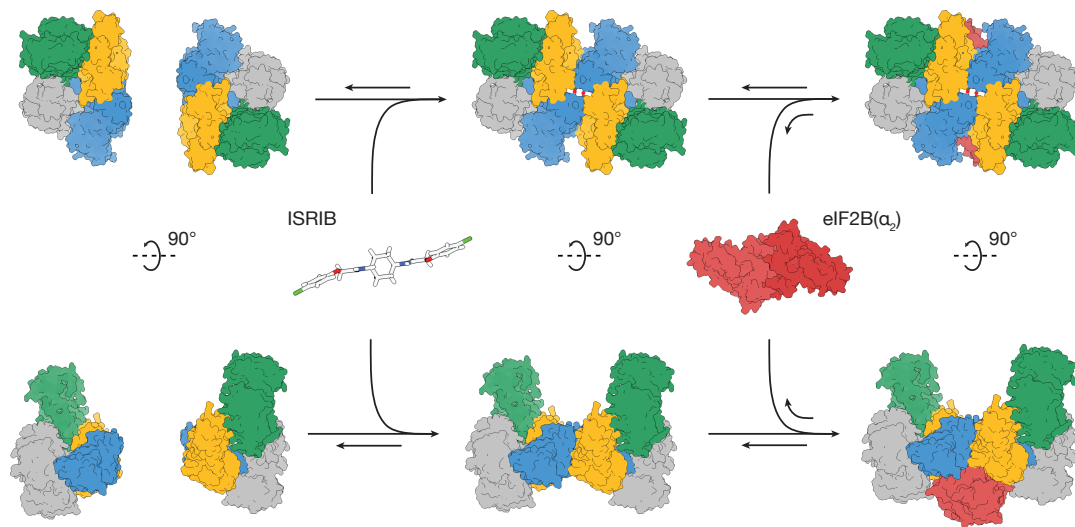


Figure 2-5

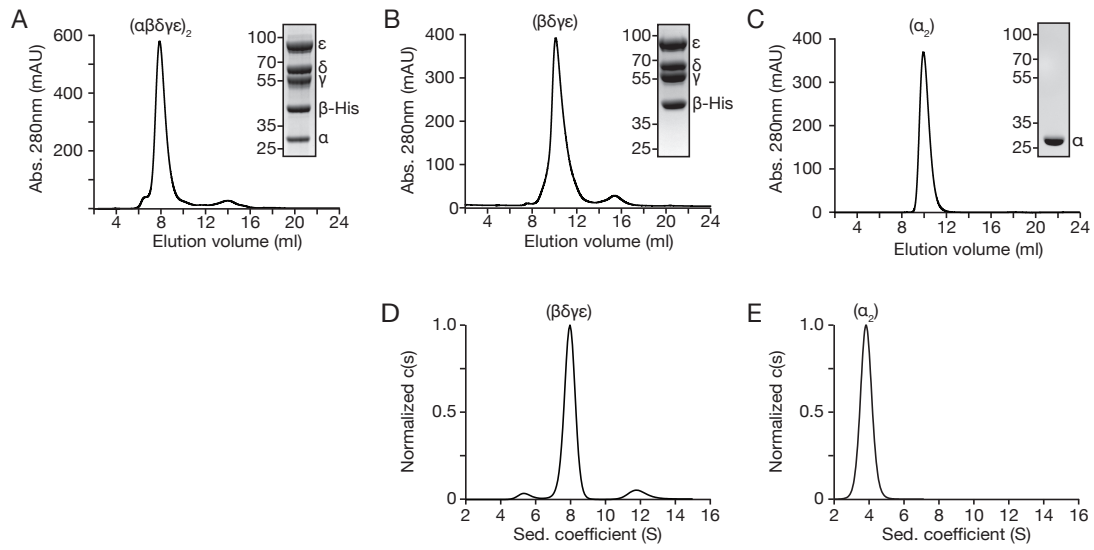
Loss- and gain-of-function dimerization mutants resist or bypass the effects of ISRIB: (A) Surface rendering of core eIF2B β (blue) and eIF2B δ (gold) subunits with residues contacting ISRIB highlighted in gray and with dimer interface indicated by dashed line. Interface residues are highlighted in a lighter hue of the colors of the contacting subunits. (B) Open-book view of the dimer-dimer interface, such that each β and δ subunit is rotated by 90°. β H160, in green, contacts both β' and δ' ; δ L179, also in green, contacts both β' and ISRIB. (C) Characterization of 1 μ M eIF2B($\beta\gamma\delta\epsilon$) containing a β H160D mutation in the presence (right) and absence (left) of 1 μ M ISRIB by analytical ultracentrifugation. (D) GEF activity of eIF2B($\beta\gamma\delta\epsilon$) containing a β H160D mutation in the presence and absence of ISRIB. (E) Characterization of 1 μ M eIF2B($\beta\gamma\delta\epsilon$) containing a δ L179V mutation in the presence (right) and absence (left) 1 μ M ISRIB by analytical ultracentrifugation. (F) GEF activity of eIF2B($\beta\gamma\delta\epsilon$) containing a δ L179V mutation in the presence and absence of ISRIB.

Figure 2-6



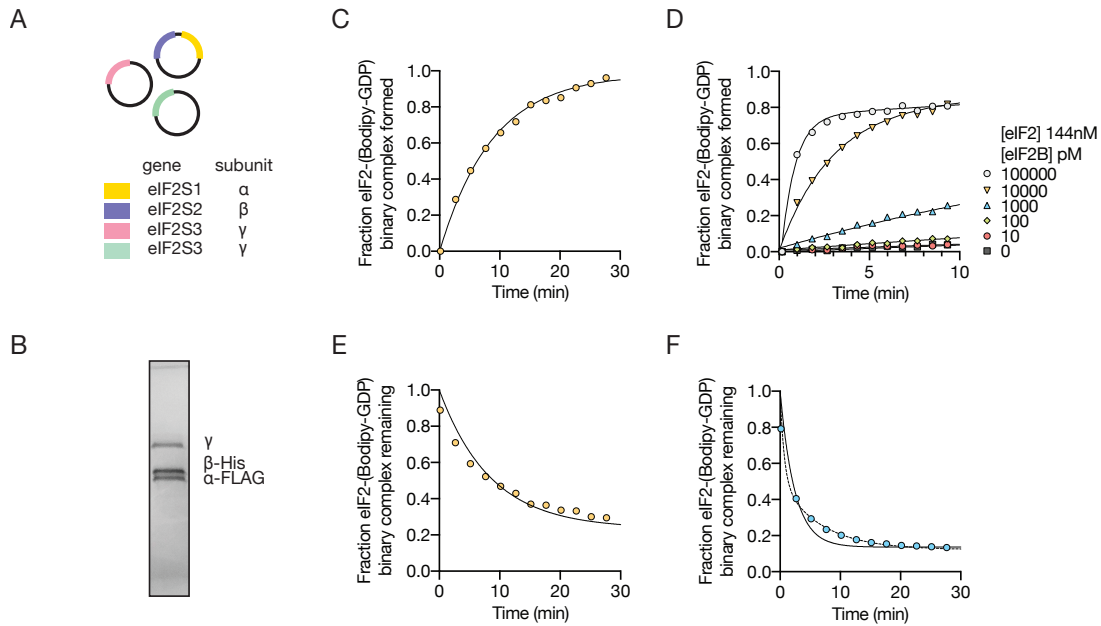
Model for ISRIB's mechanism of action: ISRIB staples together tetrameric eIF2B($\beta\gamma\delta\epsilon$) subcomplexes, building a more active eIF2B($\beta\gamma\delta\epsilon$)₂ octamer. In turn, the ISRIB-stabilized octamer binds eIF2B(α_2) with greater affinity, enhancing the formation of a fully-active, decameric holoenzyme.

Figure 2-S1



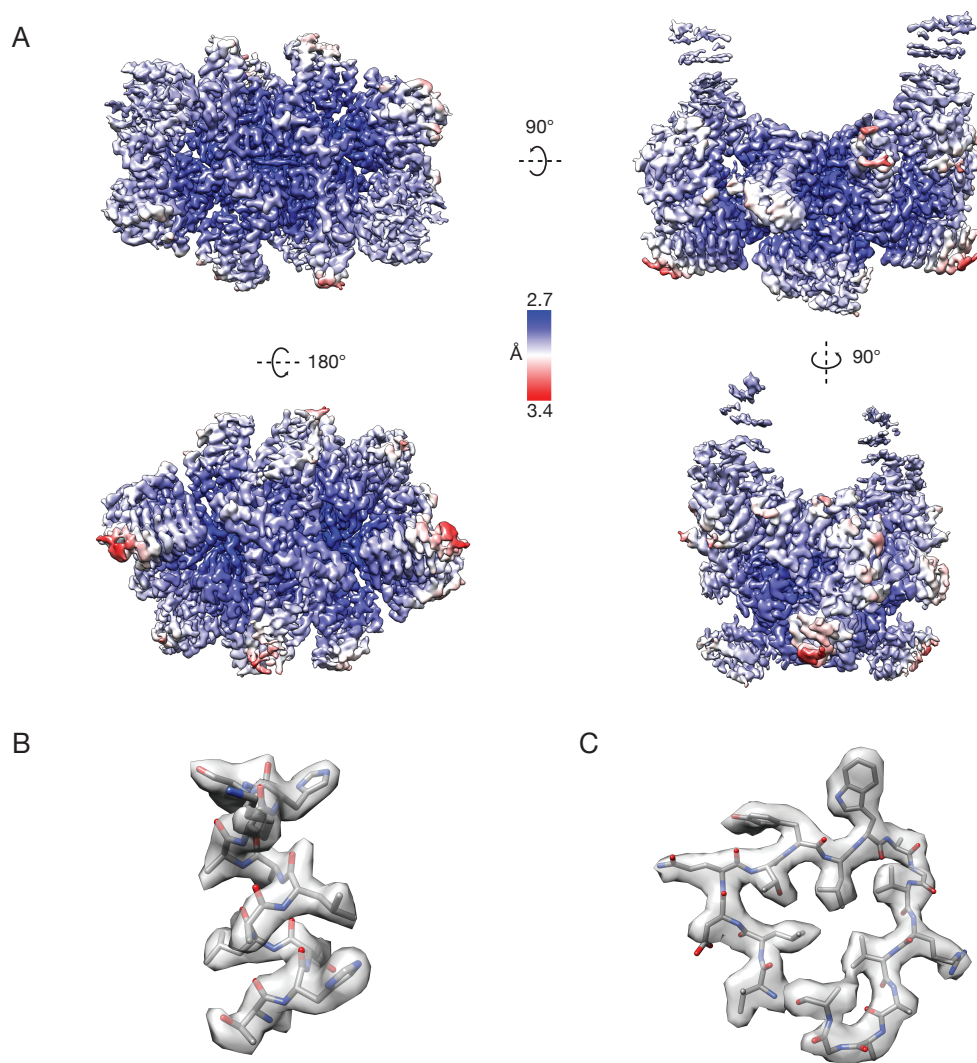
Purification and characterization of decameric eIF2B: Characterization of (A) eIF2B($\alpha\beta\gamma\delta\epsilon$)₂, (B) eIF2B($\beta\gamma\delta\epsilon$), and (C) eIF2B(α_2), by size-exclusion chromatography. Peak fractions were concentrated and characterized further by SDS-PAGE followed by Coomassie blue staining. Characterization of (D) eIF2B($\alpha\beta\gamma\delta\epsilon$)₂ and (E) eIF2B(α_2) by analytical ultracentrifugation.

Figure 2-S2



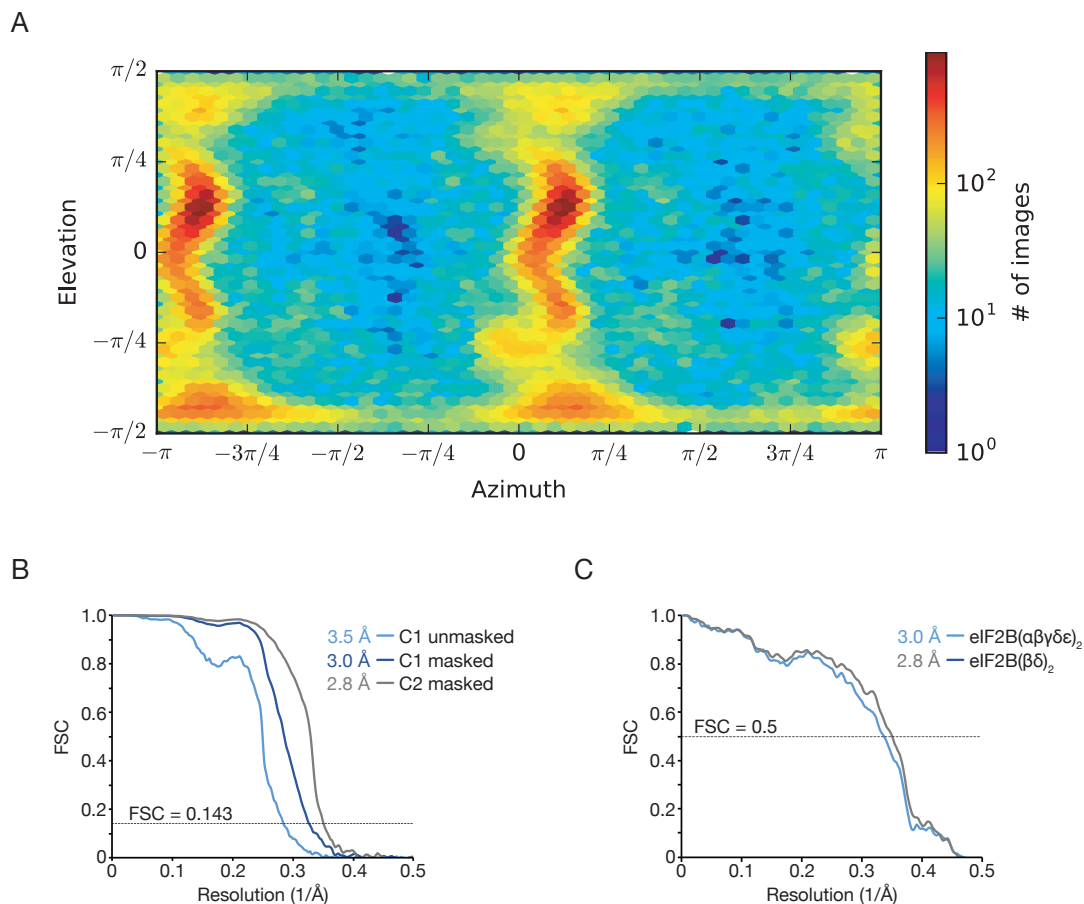
Purification of substrate eIF2 and implementation of GDP exchange assay: (A) Recombinant *S. cerevisiae* expression system for human eIF2 as described in (30). Two copies of eIF2 γ compensate for low expression of this gene. (B) Characterization of purified eIF2 by SDS-PAGE followed by Coomassie blue staining. (C) Fluorescent GDP loading and subsequent (D) unloading curves in the presence of 10 nM eIF2B. (E) GEF activity varies with eIF2B($\alpha\beta\gamma\delta\epsilon$)₂ concentration as measured by loading of fluorescent GDP. (F) Comparison of single-(solid line) and double-exponential (dotted line) fits of ISRIB-mediated GDP unloading. Double-exponential fits correlate better with the data ($R^2 = 0.98$ for double, 0.88 for single) but cannot be explained by current models for nucleotide exchange.

Figure 2-S3



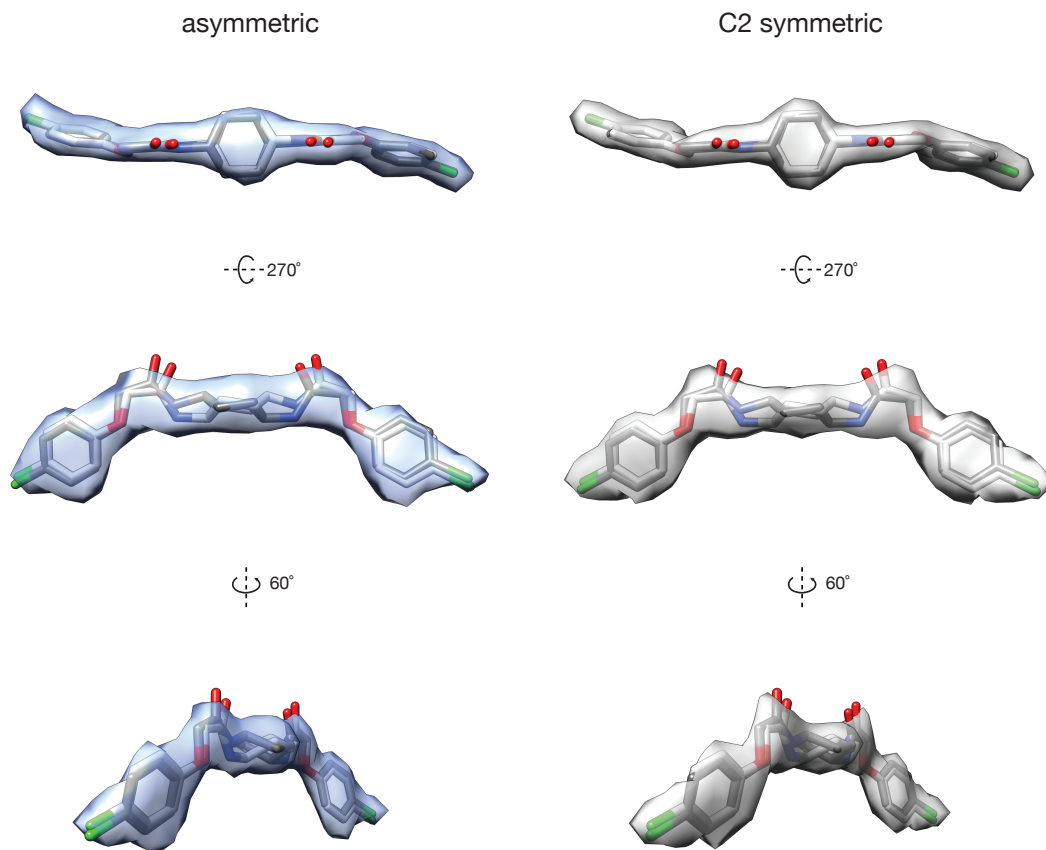
Local resolution: (A) Local resolution estimates determined using RELION 2.1 and displayed using UCSF Chimera. Superlative regions of the cryoEM map rendered as a transparent isosurface and interpreted with atomic coordinates for an (B) alpha-helix and a turn of a (C) beta-solenoid.

Figure 2-S4



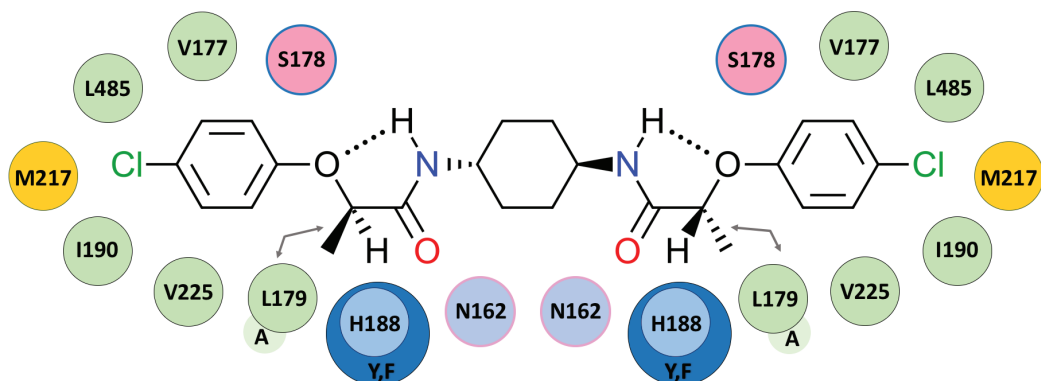
Particle orientation distribution and resolution determination. (A) Plot of per-particle direction distribution over azimuth and elevation angles using CryoSPARC. (B) Fourier shell correlations for independent half maps reconstructed without symmetry or masking, versus without symmetry and with soft masking, and versus with C2 symmetry and soft masking. (C) Fourier shell correlations for the final cryoEM density map versus simulated density maps for the atomic model of the intact decamer versus the ISRIB-stabilized subunits alone.

Figure 2-S5



Symmetry and multiple conformer interpretation of the ligand density: Isosurface representations of the cryoEM density computed without symmetry (left, blue) versus with C2 symmetry imposed throughout refinement (right, gray). Although additional conformers of the ligand remain possible given the density, the pair of chair conformers shown are related by rotations of 180° about the N–C bonds to the central cyclohexane ring, or equivalently by rotation of the entire ligand 180° about the axis orthogonal to the plane of the cyclohexane ring. The U-shaped conformation of the O-aryl glycolamide side chains is consistent with extensive structure–activity studies of ISRIB analogs (see Fig. S6, (28, 34))

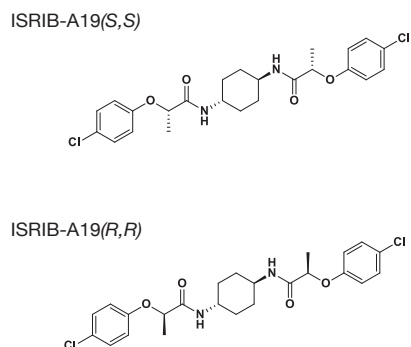
Figure 2-S6



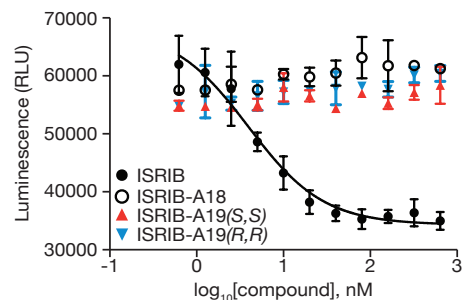
ISRIB binding environment and key mutants: A subset of residues lining the ISRIB binding pocket are rendered as bubbles and color-coded according to amino acid properties. β M217 (yellow) contributes to the hydrophobicity of the pocket and an apparent sulfur-halogen interaction. β I190, β V225, δ L485, δ V177 and δ L179 (green) contribute to the hydrophobicity of deep pockets in the binding site. Mutagenizing δ L179 to Ala (smaller, lighter green circle) opened the binding pocket and enabled the methyl-substituted ISRIB-A19(*R,R*) analog to bind (arrows point to the mutated residue and the added methyl group, also see Figs. 2F and 5D). β N162 (blue), δ S178 (pink), and β H188 (blue) coordinate polar moieties on ISRIB. Mutagenizing β H188 to more electron-rich aromatic residues, Tyr or Phe, (larger, darker blue circle), enhanced ISRIB binding, consistent with a stronger C-H- π interaction in the mutants (also see Figs. 2F, Fig. 3). The proposed upside-down “U-shaped” conformation of the ligand may be stabilized by weak intramolecular hydrogen bonds shown as dashed lines.

Figure 2-S7

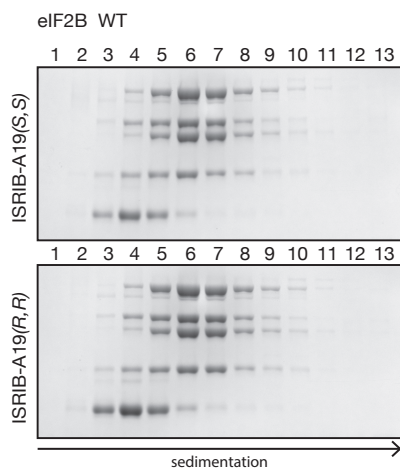
A.



B.

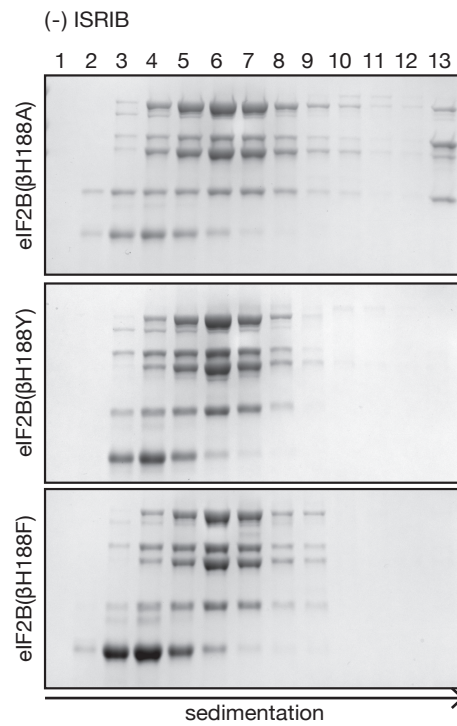


C.



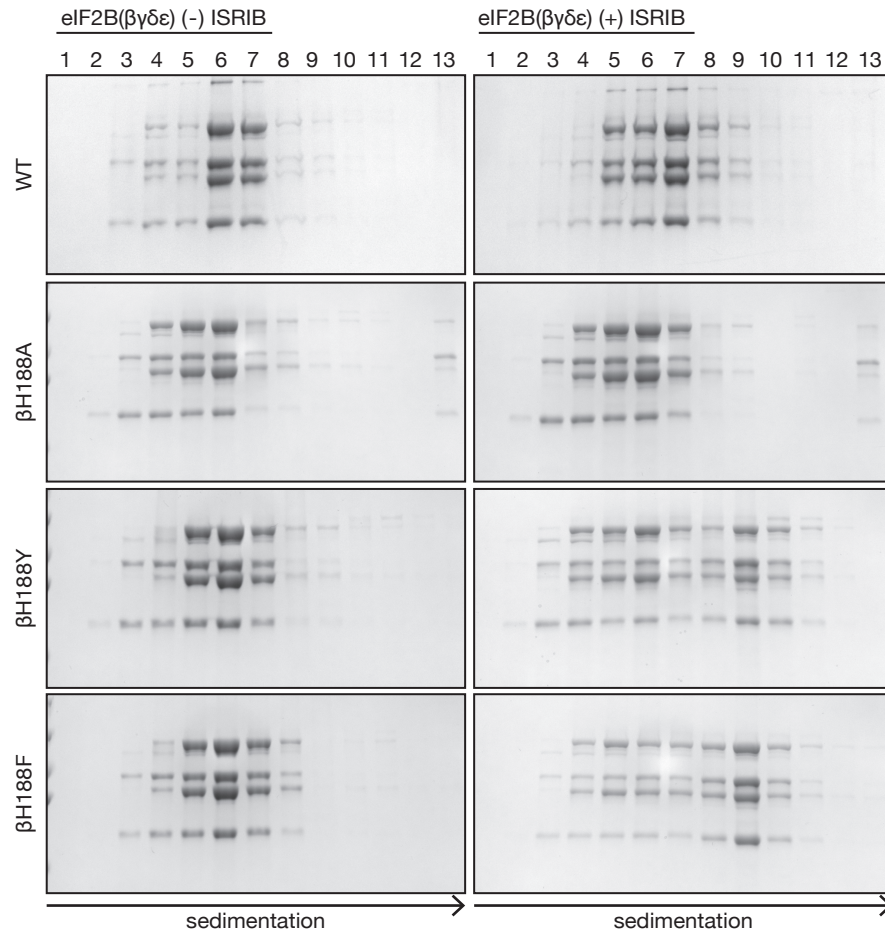
Characterization of ISRIB-A19 enantiomers A19(R,R) and A19(S,S): (A) Chemical structure of ISRIB-A19(R,R) and ISRIB-A19(S,S). (B) Cell-based ATF4-luciferase assay with ISRIB, a previously characterized inactive analog ISRIB-A18 (28), ISRIB-A19(R,R), and ISRIB-A19(S,S) (n = 3). ISRIB was measured to have an EC_{50} of 3.94 nM for reversal of tunicamycin induced ATF-luciferase production. (C) Stability of eIF2B($\alpha\beta\gamma\delta\epsilon$)₂ in the presence of 500 nM ISRIB-A19(R,R) or ISRIB-A19(S,S) as assessed by velocity sedimentation on sucrose gradients.

Figure 2-S8



Characterization of β H188 mutations by sedimentation velocity: Stability of eIF2B($\alpha\beta\gamma\delta\epsilon$)₂ in the context of β H188A, β H188Y, and β H188F mutations as assessed by velocity sedimentation on sucrose gradients in the absence of ISRIB.

Figure 2-S9



eIF2B(βγδε) mutants enhance ISRIB-mediated dimerization: Stability of eIF2B(βγδε)₂ in the context of wild-type, βH188A, βH188Y, and βH188F as assessed by velocity sedimentation on sucrose gradients in the presence and absence of ISRIB.

Table 2-S1**Data Collection Parameters**

Data Collection				
	eIF2B($\alpha\beta\gamma\delta\epsilon$) ₂ + ISRIB at Janelia	eIF2B($\alpha\beta\gamma\delta\epsilon$) ₂ + ISRIB at Berkeley	eIF2B($\alpha\beta\gamma\delta$)	eIF2B($\alpha\beta\gamma\delta$) + ISRIB
Pixel Size (Å)	1.02	0.838	1.15	1.15
Defocus Range (microns)	-0.3 to -3.9	-0.3 to -3.9	-0.7 to -5.5	-0.6 to -5.4
Defocus Mean (microns)	-2.0	-1.8	-1.9	-1.8
Voltage (kV)	300	300	200	200
Magnification (x)	29,000	29,000	36,000	36,000
Spherical Aberration (mm)	2.7	2.62	2.0	2.0
Detector	K2 Summit	K2 Summit	K2 Summit	K2 Summit
Detector Pixel Size (microns)	5.0	5.0	5.0	5.0
Per frame electron dose (e ⁻ /Å ²)	1.19	1.63	1.2	1.2
# of frames	67	27	40	40
Frame Length (seconds)	0.15	0.18	0.2	0.2
Micrographs	1780	1515	129	67

Table 2-S2**Refinement Parameters**

Refinement			
	eIF2B($\alpha\beta\gamma\delta\epsilon$) ₂ + ISRIB at Janelia	eIF2B($\alpha\beta\gamma\delta\epsilon$) ₂ + ISRIB at Berkeley	Combined
Particles following 2D classification	102599	99526	202,125
FSC Average Resolution, unmasked (Å)	3.8	3.5	3.0
FSC Average Resolution, masked (Å)	3.4	3.2	2.8
Map Sharpening B-factor	-75	-75	-78

Table 2-S3**Modeling**

Model Statistics	
Number of Atoms, macromolecules	24208
Number of Atoms, ligands	60
Molprobit Score	1.62
Clashscore, all atoms	5.56
Favored Rotamers (%)	99.76
Outlier Rotamers (%)	0.24
RMS (bonds)	0.0047
RMS (angles)	1.16
Ramachandran Favored (%)	95.43
Ramachandran Outliers (%)	0.00
Ramachandran Allowed (%)	4.57

MATERIALS AND METHODS

Cloning of eIF2B expression plasmids

The five human eIF2B subunits were *E. coli*-codon optimized and synthesized on the BioXp 3200 System (SGI-DNA) in six blunt-end dsDNA fragments. Synthesized sequences are appended at the end of this document. Fragments were cloned into pCR-BluntII-TOPO vector with the Zero Blunt TOPO PCR Cloning Kit (Invitrogen), and verified by sequencing. In brief, subunits of eIF2B were PCR amplified from TOPO cloned vectors and Infusion (Clontech) cloned into multi-gene expression plasmids with compatible drug resistances and origins of replication: pETDuet-1 (Novagen 71146-3), pACYCDuet-1 (Novagen 71147-3), or pCOLADuet-1 (Novagen 71406-3) vectors. Each expression plasmid contains two cloning sites (site1 and site2), enabling simultaneous expression of up to two genes per plasmid. eIF2B1 (encoding the α subunit) was inserted into site1 of pETDuet-1 (pJT066). eIF2B2 (encoding the β subunit) and eIF2B4 (encoding the δ subunit) were inserted into site1 and site2 of pACYCDuet-1, respectively (pJT073). eIF2B3 (encoding the γ subunit) and eIF2B5 (encoding the ϵ subunit) were inserted into site1 and site2 of pCOLADuet-1, respectively (pJT074). To note eIF2B5 was synthesized in two fragments eIF2B5_1 and eIF2B5_2 that were simultaneously inserted into site2 by Infusion.

Purification of decameric eIF2B($\alpha\beta\delta\gamma\epsilon$)₂

pJT066, pJT073, and pJT074 were co-transformed into One Shot BL21 Star (DE3) chemically competent *E. coli* cells (Invitrogen) and grown in Luria-broth containing ampicillin, kanamycin, and chloramphenicol at 37° C on an orbital shaker. When the culture reached an OD600 of 0.6, the temperature was reduced to 16° C, induced with 0.8 mM IPTG (Gold Biotechnology), and

grown for 16 hours. Cells were harvested and lysed with the EmulsiFlex-C3 (Avestin) in a buffer containing [20 mM HEPES-KOH pH 7.5, 250 mM KCl, 1 mM tris(2-carboxyethyl)phosphine (TCEP), 5 mM MgCl₂, 15 mM imidazole, and complete EDTA-free protease inhibitor cocktail (Roche)]. The lysate was clarified at 30,000 x g for 20 min at 4° C. Subsequent purification steps were conducted on the ÄKTA Pure (GE Healthcare) system at 4° C.

The clarified lysate was loaded onto a HisTrap HP 5 ml, washed in binding buffer containing [20 mM HEPES-KOH pH 7.5, 200 mM KCl, 1 mM TCEP, 5 mM MgCl₂, 15 mM imidazole] and eluted with a linear gradient (75 ml) of 15 mM to 300 mM imidazole in the same buffer. The eIF2B fraction eluted from the HisTrap column at 80 mM imidazole. The eIF2B fraction was collected and loaded onto a 20 ml Mono Q HR16/10 column (GE Healthcare), washed in Buffer A [20 mM HEPES-KOH pH 7.5, 200 mM KCl, 1 mM TCEP, 5 mM MgCl₂] and eluted with a linear gradient (200 ml) of 200 mM to 500 mM KCl in the same buffer. The eIF2B fraction eluted off the Mono Q column at a conductivity of 46 mS/cm (corresponding to 390 mM KCl). Fractions were collected, concentrated with an Amicon Ultra-15 concentrator (EMD Millipore) with a 100,000 dalton molecular weight cut-off and loaded onto a Superdex 200 10/300 GL column (GE Healthcare) equilibrated with Buffer A. A typical preparation yielded approximately 0.5 mg of eIF2B($\alpha\beta\delta\gamma\epsilon$)₂ from a 1 liter culture.

EM Sample Preparation and Data Collection

Decameric eIF2B($\alpha\beta\gamma\delta\epsilon$)₂ + ISRIB: Following size exclusion chromatography, eIF2B($\alpha\beta\gamma\delta\epsilon$)₂ was diluted to 500 nM and a stock solution of 200 μ M ISRIB in N-Methyl-2-pyrrolidone (NMP) was added to a final ISRIB concentration of 2 μ M in a final solution containing [20 mM HEPES-KOH pH 7.5, 200 mM KCl, 1 mM TCEP, 5 mM MgCl₂, 0.5% NMP] and incubated on ice for 10

min. This sample was applied to either C-Flat 1.2/1.3-2C grids (EMS, USA) or Quantifoil R 1.2/1.3 200 Au mesh grids (Quantifoil, Germany). C-flat grids were used without additional cleaning or glow discharging. Quantifoil grids were soaked in chloroform for 30 min and desiccated overnight in a fume hood before use without glow discharging. Using a Vitrobot Mark IV at 4° C and 100% humidity, 3.5 μL of sample was applied to the grid, incubated for an additional 10 s, then blotted with -0.5 mm offset for ~ 6 s and plunge frozen in liquid ethane. Two datasets were collected on different microscopes. The first dataset was collected with the 300 kV Titan Krios “2” at the HHMI Janelia Research Campus using a K2 Summit detector operated in super-resolution mode. 1780 images were collected at a magnification of 29,000X (0.51 $\text{\AA}/\text{pixel}$) as dose-fractionated stacks of 67 x 0.15 second exposures ($1.19 \text{ e}^-/\text{\AA}^2$) for a total dose of $\sim 80 \text{ e}^-/\text{\AA}^2$ (see Table S1). The second dataset was collected with the 300 kV Titan Krios at UC Berkeley using a K2 Summit detector operated in super-resolution mode. 1515 images were collected at a magnification of 29,000X (0.42 $\text{\AA}/\text{pixel}$) as dose-fractionated stacks of 27 x 0.18 second exposures ($1.83 \text{ e}^-/\text{\AA}^2$) for a total dose of $\sim 44 \text{ e}^-/\text{\AA}^2$ (see Table S1).

Tetrameric eIF2B($\alpha\beta\gamma\delta$) +/- ISRIB: Following size exclusion chromatography, tetrameric eIF2B($\alpha\beta\gamma\delta$) was diluted to 800 nM and vitrified in the absence of ISRIB and in the presence of 2 μM ISRIB, as described above, but with ~ 4 s blot time. 129 micrographs of ligand-free and 67 micrographs of ISRIB-bound sample were collected on the 200 kV Talos Arctica at UCSF at 36,000X using a K2 Summit detector operated in super-resolution mode (1.15 $\text{\AA}/\text{pixel}$).

Image Analysis and 3D Reconstruction

All dose-fractionated image stacks were corrected for motion artefacts, 2x binned in the Fourier domain, and dose-weighted using MotionCor2 (35), resulting in one dose-weighted and one

unweighted integrated image per stack with pixel sizes of 1.02 Å (Janelia) or 0.838 Å (UC Berkeley). The parameters of the Contrast Transfer Function (CTF) were estimated using GCTF-v1.06 (36) and the motion-corrected but unweighted images. ~1000 particles per dataset were manually selected and averaged in 2D using RELION 2.0 (37). The resulting class sums were then used as templates for automated particle picking using Gautomatch-v0.55 (36), followed by extraction and rescaling to a common pixel size of 0.838 Å and four rounds of 2D classification (see Table S2).

For the 3D reconstruction of decameric eIF2B($\alpha\beta\gamma\delta\epsilon$)₂ + ISRIB, the resulting subset of particles were input into cryoSPARC (38) to compute an *ab-initio* reconstruction without symmetry, followed by homogeneous refinement in both cryoSPARC (dynamic masking) and in RELION 2.0 (unmasked) with no symmetry. Subsequent heterogeneous refinement (cryoSPARC) or multi-class 3D classification (RELION 2.0) removed less than 1% of the remaining particles (see Table S1).

High-resolution homogenous refinement was then performed in parallel in cryoSPARC, RELION 2.1, and FREALIGN (39) using soft-edged masks and imposed C2 symmetry (see Fig. S3-4). All three approaches yielded maps of similar visual quality and that differed in numerical resolution by ~0.1 Å, as measured by Fourier shell correlation. All three maps were low-pass filtered and sharpened using automated procedures and used comparatively during model building in COOT and PHENIX (see below). Molecular graphics and analyses were performed with the UCSF Chimera package and the FREALIGN map. Chimera is developed by the Resource for Biocomputing, Visualization, and Informatics at UCSF (supported by NIGMS P41-GM103311, (40)). The map-versus-model FSC plots were generated using the FREALIGN map (see below and Fig. S4). Accession numbers for the human eIF2B structures determined with

FREALIGN, cryoSPARC, and RELION, respectively, are as follows: EMD-7442, EMD-7443, EMD-7444 (density maps; Electron Microscopy Data Bank) and 6CAJ (coordinates of atomic models; Protein Data Bank).

Atomic Modeling and Validation

An initial model of the human complex was generated using one-to-one threading as implemented in Phyre2 (41) using from the *S. pombe* crystal structure (PDB: 5B04, (8)) structure for the β , γ , δ , and ϵ subunits and the *H. sapiens* crystal structure (PDB: 3ECS, (42)) for the α subunit. The initial ISRIB ligand model was generated in PHENIX eLBOW (43) using the SMILES, manually adjusted in COOT (44), and then refined with phenix.real_space_refine (45) using global minimization and simulated annealing. This initial model was manually adjusted in COOT a second time and further refined in phenix.real_space_refine using global minimization, secondary structure restraints, and local grid search. This model was manually adjusted a third and final time in COOT, minimized in phenix.real_space_refine with per-residue B-factors, and the final model statistics were tabulated using Molprobity (46) (see Table S3). Map versus atomic model FSC plots for the entire decamer and the isolated $\beta\delta\beta'\delta'$ chains were computed using EMAN 2 (47) using calculated density maps from e2pdb2mrc.py with heteroatoms (ISRIB) and per-residue B-factor weighting. Solvent accessible surfaces and buried surface areas were calculated from the atomic models using UCSF ChimeraX. Final atomic models have been deposited at the PDB with accession code 6CAJ.

Cloning of mutant eIF2B expression plasmids

Mutant eIF2B constructs were generated by site-directed mutagenesis on pJT073 using the primer indicated and its reverse complement. Highlighted bases indicate sites of mutagenesis.

δ L179A (pJT091): 5'-tacggttctaaagtttctgctttctctcacctgccgcag-3'

β H188A (pJT089): 5'-gctgctcgtaaacgtaaattcgctgttatcggtgctgaatgcgct-3'

β H188F (pJT094): 5'-gctcgtaaacgtaaattcttcgttatcggtgctgaatg-3'

β H188Y (pJT095): 5'-gctgctcgtaaacgtaaattctacgttatcggtgctgaatg-3'

δ L179V (pJT090): 5'-tacggttctaaagtttctgctttctctcacctgccgcag-3'

β H160D (pJT102): 5'-caggctctggaacacatcgactctaacgaagttatcatg-3'

Purification of tetrameric eIF2B($\beta\delta\gamma\epsilon$)

Tetrameric eIF2B($\beta\delta\gamma\epsilon$) and tetrameric eIF2B($\beta\delta\gamma\epsilon$) mutant proteins were purified using the same protocol as described for the decamer with the exception that expression strains were co-transformed without the eIF2B α subunit expressing plasmid. A typical preparation yielded approximately 0.75 mg of eIF2B($\beta\delta\gamma\epsilon$) from a 1 liter culture.

eIF2B($\beta\delta\gamma\epsilon$) tetramer with co-transformed plasmids: pJT073, pJT074

δ L179A eIF2B($\beta\delta\gamma\epsilon$) tetramer with co-transformed plasmids: pJT091, pJT074

β H188A eIF2B($\beta\delta\gamma\epsilon$) tetramer with co-transformed plasmids: pJT089, pJT074

β H188F eIF2B($\beta\delta\gamma\epsilon$) tetramer with co-transformed plasmids: pJT094, pJT074

β H188Y eIF2B($\beta\delta\gamma\epsilon$) tetramer with co-transformed plasmids: pJT095, pJT074

δ L179V eIF2B($\beta\delta\gamma\epsilon$) tetramer with co-transformed plasmids: pJT090, pJT074

β H160D eIF2B($\beta\delta\gamma\epsilon$) tetramer with co-transformed plasmids: pJT102, pJT074

Purification of eIF2B(α_2)

Purification of the eIF2B(α_2) was adapted from previously published purifications (6, 42). The α subunit was N-terminally tagged with a 6x-His tag followed by a TEV cleavage site (pJT075). pJT075 was transformed into BL21 (DE3) *E. coli* cells and grown in Luria-broth containing ampicillin 37° C on an orbital shaker. When the culture reached an OD600 of 0.8, the temperature was reduced to 20° C, induced with 0.8 mM IPTG, and grown for 16 hours. Cells were harvested and lysed in a buffer containing [20 mM HEPES-KOH pH 7.5, 250 mM KCl, 1 mM TCEP, 5 mM MgCl₂, 20 mM imidazole, and 1x protease inhibitor cocktail] and clarified at 30,000 x g for 20 min at 4° C.

The clarified lysate was loaded onto a 5 ml HisTrap HP column, washed in a buffer containing [20 mM HEPES-KOH pH 7.5, 30 mM KCl, 1 mM TCEP, 5 mM MgCl₂, 20 mM imidazole] and eluted with 75 ml linear gradient of 20 mM to 300 mM imidazole. The HisTrap elution was then passed through a MonoQ HR 16/10 and subsequently a MonoS HR 10/10 (GE Healthcare), both equilibrated in a buffer containing [20 mM HEPES-KOH pH 7.5, 30 mM KCl, 1 mM TCEP, 5 mM MgCl₂]. eIF2B(α_2) was collected in the flow-through fractions of both MonoQ and MonoS columns. The eIF2B(α_2) containing fraction was incubated for 16 h at 4° C with TEV protease (50 μ g TEV per liter of culture) and passed through on a HisTrap HP 5ml. Cleaved eIF2B(α_2) was recovered in the flow-through fraction, concentrated with an Amicon Ultra-15 concentrator (EMD Millipore) with a 30,000 Dalton molecular mass cut-off and chromatographed on a Superdex 75 10/300 GL (GE Healthcare) column equilibrated in a buffer containing [20 mM HEPES-KOH pH 7.5, 200 mM KCl, 1 mM TCEP, 5 mM MgCl₂, 5% glycerol]. A typical preparation yielded approximately 0.3 mg of eIF2B(α_2) from a 1 liter culture.

Preparation of human eIF2

Human eIF2 was prepared from an established recombinant *S. cerevisiae* expression protocol (30). In brief, the yeast strain GP6452 (kind gift from Graham Pavitt's lab, University of Manchester) containing yeast expression plasmids for human eIF2 subunits and a deletion of *GNC2* encoding the only eIF2 kinase in yeast, was grown to saturation in synthetic complete media (Sunrise Science Products) with auxotrophic markers (-Trp, -Leu, -Ura) in 2% dextrose. The β and α subunits of eIF2 were tagged with His6 and FLAG epitopes, respectively. A 12-liter yeast culture was grown in rich expression media containing yeast extract, peptone, 2% galactose and 0.2% dextrose. Cells were harvested and resuspended in lysis buffer [100 mM Tris pH 8.5, 300 mM KCl, 5 mM MgCl₂, 0.1% NP-40, 5 mM Imidazole, 10% glycerol (Thermo Fisher Scientific), 2 mM DTT, 1x protease inhibitor cocktail (Sigma Aldrich #11836170001), 1 μ g/ml each aprotinin (Sigma Aldrich), leupeptin (Sigma Aldrich), pepstatin A (Sigma Aldrich)]. Cells were lysed in liquid nitrogen using a steel blender. The lysate was centrifuged at 10,000 x g for 1 h at 4°C. Subsequent purification steps were conducted on the ÄKTA Pure (GE Healthcare) system at 4° C. Lysate was applied to a 5 ml HisTrap Crude column (Thermo Fisher Scientific) equilibrated in buffer [100 mM HEPES pH 7.5, 100 mM KCl, 5 mM MgCl₂, 0.1% NP-40, 5% glycerol, 1 mM dithiothreitol, 0.5x protease inhibitor cocktail, 1 μ g/ml each aprotinin, leupeptin, pepstatin A]. eIF2 bound to the column, was washed with equilibration buffer and eluted using a 50 ml linear gradient of 5 mM to 500 mM imidazole. Eluted eIF2 was incubated with FLAG M2 magnetic affinity beads, washed with FLAG wash buffer [100 mM HEPES pH 7.5, 100 mM KCl, 5 mM MgCl₂, 0.1% NP-40, 5% glycerol, 1mM TCEP, 1x protease inhibitor cocktail, 1 μ g/ml each aprotinin, leupeptin, pepstatin A] and eluted with FLAG elution buffer [identical to FLAG wash buffer but also containing 100 μ g/ml 3x FLAG peptide (Sigma Aldrich)].

Concentration of purified protein was measured by BCA assay (Thermo Fisher Scientific # PI23225); protein was flash-frozen in liquid nitrogen and stored in elution buffer at -80°C . A typical preparation yielded 1 mg of eIF2 from a 12-liter culture.

GDP exchange assay

In vitro detection of GDP binding to eIF2 was adapted from a published protocol for a fluorescence intensity-based assay describing dissociation of eIF2 and nucleotide (29). We modified the procedure to establish both loading and unloading assays for fluorescent GDP.

For the ‘GDP loading assay’, purified eIF2 (200 pmol) was incubated with a molar equivalent Bodipy-FL-GDP (Thermo Fisher Scientific) in assay buffer [20 mM HEPES pH 7.5, 100 mM KCl, 5 mM MgCl_2 , 1 mM TCEP, 1 mg/ml bovine serum albumin] to a volume of 18 μl in 384 square-well black-walled, clear-bottom polystyrene assay plates (Corning). The reaction was initiated by addition of 2 μl of buffer or purified eIF2B under various conditions to compare nucleotide exchange rates. For comparison of ‘purified decamer’ rates, eIF2B($\alpha\beta\gamma\delta\epsilon$)₂ (2 pmol) was pre-incubated in 0.1% NMP or 0.1% NMP and 2 μM ISRIB for 15 min. These concentrations of vehicle and ISRIB were used throughout, unless otherwise specified. To ensure equal concentrations of GEF catalytic sites in all experiments, comparisons with tetramer used eIF2B($\beta\gamma\delta\epsilon$) (4 pmol). ‘Assembled decamer’ was formed by incubating eIF2B($\beta\gamma\delta\epsilon$) (4 pmol) and eIF2B(α_2) (2 pmol) for 15 minutes in the presence or absence of ISRIB prior to mixing with substrate eIF2. For the ‘GDP unloading assay’, each reaction was initiated by addition of excess unlabeled GDP (200 nmol). Fluorescence intensity for both loading and unloading assays was recorded every ten seconds for 60 or 100 minutes using a TECAN Infinite M200 Pro plate reader

(excitation wavelength: 495 nm, bandwidth 5 nm, emission wavelength: 512 nm, bandwidth: 5 nm). Data collected were fit to a first-order exponential.

Analytical ultracentrifugation

Analytical ultracentrifugation sedimentation velocity experiments were conducted using the ProteomeLab XL-I system (Beckman Coulter) with a Ti60 rotor. Protein samples were loaded into cells in a buffer containing [20 mM HEPES-KOH pH 7.5, 150 mM KCl, 1 mM TCEP, 5 mM MgCl₂]. All runs were conducted at 20° C with a rotor speed of 40,000 rpm. Sedimentation was monitored at an absorbance of 280 nm. Subsequent data analysis was conducted with Sedfit (48) using a non-model based continuous c(s) distribution corrected for time invariant (TI) and radial invariant (RI) noise.

Sucrose gradients

Protocol was adapted from a previous study (28). 5-20% (w/v) sucrose gradients were prepared by tilted tube rotation on the Gradient Master 107ip (Biocomp) in a high salt buffer containing [20 mM HEPES-KOH pH 7.5, 400 mM KCl, 1 mM TCEP, 5 mM MgCl₂]. Protein samples contained 1 μM eIF2B(βδγϵ), 500 nM eIF2B(α₂), 500 nM ISRIB/analog (added from a 500 μM stock solution in NMP to yield a final NMP concentration of 0.1 %). For each gradient 200 μl of sample was loaded and centrifuges in a SW55 rotor (Beckman) for 14 hours at 40,000 rpm 4° C. Thirteen fractions of 400 μl were collected by aspirating from the top of the gradient, and protein was precipitated by addition of trichloroacetic acid to 15%. After incubation for 90 min on ice, the protein precipitate was collected by centrifugation, and the pellet was resuspended in SDS loading buffer, loaded on a 10% SDS-polyacrylamide gel (Bio-rad), and after electrophoresis

stained with Coomassie blue. Stained gels were then imaged on a ChemiDoc XRS+ imaging system (Bio-Rad). Quantification of gels was conducted in ImageJ. Fraction of total eIF2B($\beta\gamma\delta\epsilon$) in each of 13 lanes were quantified using a built-in gel-analyzer function. Area under each densitometry plot was calculated and divided by the sum of all areas measured from lanes 1-13 to obtain 'fraction of eIF2B($\beta\gamma\delta\epsilon$)'.

In-cell luciferase assays

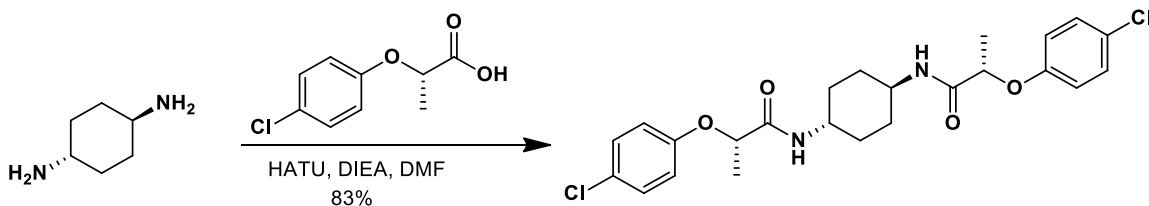
Luciferase assays were conducted using a HEK293T cell line carrying an ATF4 luciferase reporter (18, 28). Cells were plated at a density of 30,000 cells/well in a 96 well poly-lysine coated plate (Greiner Bio-One). Cells were treated the next day with 1 μg / ml tunicamycin and varying ISRIB concentrations for 7 h. Luciferase activity was then assayed using One Glo (Promega) and luminescence quantified in a SpectraMax M5 (Molecular Devices).

ISRIB-A19(*R,R*) and (*S,S*) synthesis & validation

(2*S*)-2-(4-chlorophenoxy)propanoic acid was purchased from Enamine. Reagents and solvents were purchased from Sigma- Aldrich, Acros or TCI America and used as received unless otherwise indicated. Flash column chromatography was carried out using a Biotage Isolera Four system and SiliaSep silica gel cartridges from Silicycle. ¹H NMR spectra were recorded on a Varian INOVA-400 400MHz spectrometer. Chemical shifts are reported in δ units (ppm) relative to residual NMR solvent peaks. Coupling constants (*J*) are reported in hertz (Hz).

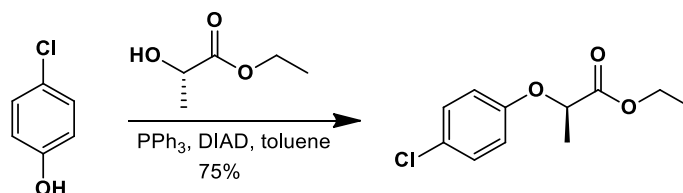
Characterization data are reported as follows: chemical shift, multiplicity (s=singlet, d=doublet, t=triplet, q=quartet, br=broad, m=multiplet), coupling constants, number of protons, mass to charge ratio. LC/MS analyses were performed on a Waters Micromass ZQ/Waters 2795 Separation Module/Waters 2996 Photodiode Array Detector/Waters 2424 Evaporative Light Scattering Detector system. Separations were carried out on XTerra® MS C₁₈ 5 μ m 4.6x50mm column at ambient temperature using a mobile phase of water-methanol containing 0.1% formic acid.

Synthesis of (2*S*)-2-(4-Chlorophenoxy)-N-[(1*r*,4*r*)-4-[(2*S*)-2-(4-chlorophenoxy)propanamido]cyclohexyl]propanamide (ISRIB-A19(*S,S*)):



To a solution of the (2*S*)-2-(4-chlorophenoxy)propanoic acid (0.176 g, 0.88 mmol) in *N,N*-dimethylformamide (4 ml), was added HATU (0.35 g, 0.88 mmol), *trans*-1,4-diaminocyclohexane (0.05 g, 0.44 mmol), and *N,N*-diisopropylethylamine (0.3 ml, 1.76 mmol). The mixture was stirred at ambient temperature until the reaction was judged complete by LC/MS. The reaction mixture was then filtered and the collected material washed with diethyl ether, water, and then dried to obtain 175 mg (83%) of the title compound as a white solid. ¹H NMR (400 MHz, *d*₆-DMSO) δ 7.96 (d, *J* = 8 Hz, 2H), 7.30-7.34 (m, 4H), 6.89-6.93 (m, 4H), 4.63 (q, *J* = 6.6 Hz, 2H), 3.48 (br.s, 2H), 1.73 (d, *J* = 7.3 Hz, 2H), 1.64 (d, *J* = 7.3 Hz, 2H), 1.40(d, *J* = 6.6 Hz, 6H), 1.23-1.33 (m, 4H); ¹³C NMR (100 MHz, CDCl₃) δ 170.40, 156.85, 129.65, 125.17, 117.41, 74.31, 47.33, 31.16, 19.10; LCMS *m/z* 479 (MH⁺).

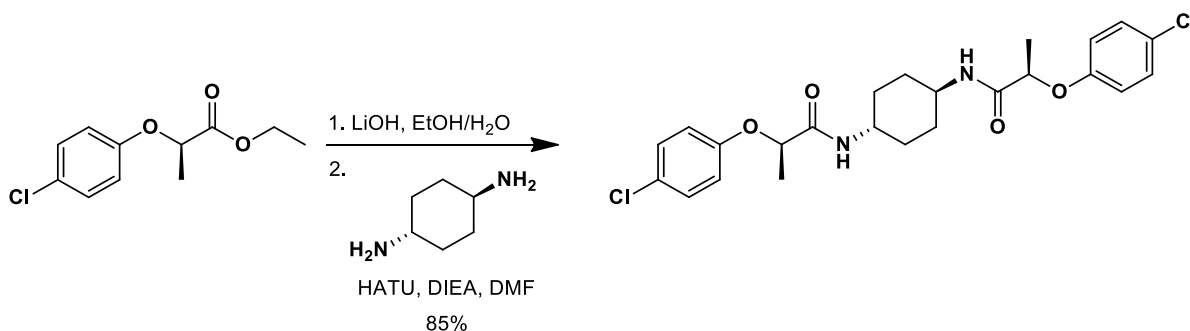
Synthesis of ethyl (2*R*)-2-(4-chlorophenoxy)propanoate:



To a cooled (-20° C) solution of ethyl (2*S*)-2-hydroxypropanoate (0.330 g, 2.8 mmol), 4-chlorophenol (0.359 g, 2.8 mmol) and triphenylphosphine (0.733 g, 2.8 mmol, 1.0 equiv.) in toluene was added diisopropyl azodicarboxylate (0.550 ml, 2.8 mmol). The mixture was stirred at -20° C for an hour and then at ambient temperature for 24 hours. The reaction mixture was concentrated *in vacuo* to remove the toluene solvent. To the resulting residue was added hexanes and the precipitate that formed was filtered off. The filtrate was concentrated *in vacuo* and purified by flash column chromatography (25 g, 0-10% EA/hex) to obtain 0.48 g (75%) of the

product as a yellow oil. $^1\text{H NMR}$ (400 MHz, CDCl_3) δ 7.21-7.26 (m, 2H), 6.80-6.84 (m, 2H), 4.71 (q, $J = 6.8$ Hz, 1H), 4.20-4.25 (m, 2H), 1.62 (d, $J = 6.8$ Hz, 3H), 1.26 (t, $J = 7.2$ Hz, 3H); LCMS m/z 228 (MH $^+$).

Synthesis of (2R)-2-(4-Chlorophenoxy)-N-[(1r,4r)-4-[(2R)-2-(4-chlorophenoxy)propanamido]cyclohexyl]propanamide (ISRIB-A19(R,R)):



To a solution of ethyl (2R)-2-(4-chlorophenoxy)propanoate (0.150 g, 0.7 mmol) in 2:1 mixture of ethanol-water (6 ml) was added 1 M aqueous lithium hydroxide solution (1.312 ml, 1.3 mmol). The mixture was stirred at ambient temperature for 24 h. The reaction mixture was concentrated *in vacuo* to remove ethanol, diluted with water and adjusted to pH 2 with 1 N aqueous hydrochloric acid solution. The mixture was extracted with ethyl acetate. The organic extracts were washed with brine, dried over magnesium sulfate and concentrated to obtain 123 mg of (2R)-2-(4-chlorophenoxy)propanoic acid as a white solid. This material was used directly in the next reaction.

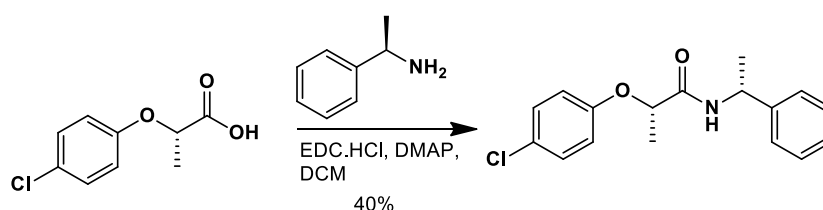
To a solution of the (2R)-2-(4-chlorophenoxy)propanoic acid (0.1 g, 0.5 mmol) in *N,N*-dimethylformamide (2 ml), was added HATU (0.2 g, 0.525 mmol), *trans*-1,4-diaminocyclohexane (0.028 g, 0.25 mmol), and *N,N*-diisopropylethylamine (0.174 ml, 1.0 mmol). The mixture was stirred at ambient temperature until the reaction was judged complete

by LC/MS. The reaction mixture was filtered and the collected material was washed with diethyl ether, water, and then dried to obtain 100 mg (85%) of the title compound as a white solid. ¹H NMR (400 MHz, *d*₆-DMSO) δ 7.96 (d, *J* = 8.3 Hz, 2H), 7.30-7.34 (m, 4H), 6.88-6.92 (m, 4H), 4.63 (q, *J* = 6.5 Hz, 2H), 3.49 (br.s, 2H), 1.73 (d, *J* = 8.3 Hz, 2H), 1.64 (d, *J* = 7.3 Hz, 2H), 1.44 (d, *J* = 6.6 Hz, 6H), 1.22-1.30 (m, 4H); LCMS *m/z* 479 (MH⁺).

Confirmation of inversion of configuration in preparation of intermediates for ISRIB-A19(*R,R*) synthesis.

To confirm inversion of stereochemical configuration during the preparation of ethyl (2*R*)-2-(4-chlorophenoxy)propanoate, the (2*S*)-2-(4-chlorophenoxy)propanoic acid and (2*R*)-2-(4-chlorophenoxy)propanoic acid used in the preparation of ISRIB-A19(*S,S*) and ISRIB-A19(*R,R*), respectively, were coupled to (*R*)-(+)-alpha-methylbenzylamine as detailed below. The resulting amides were found to be single and distinct diastereoisomers, confirming the enantiomeric relationship of the propanoic acids and accordingly of ISRIB-A19(*R,R*) and ISRIB-A19(*S,S*).

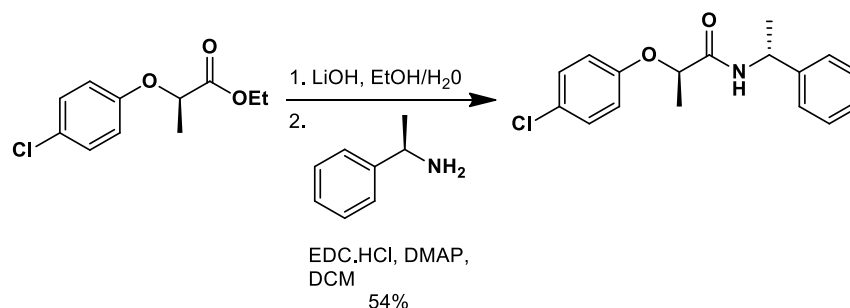
Synthesis of (2*S*)-2-(4-chlorophenoxy)-*N*-[(1*R*)-1-phenylethyl]propanamide:



To a solution of (2*S*)-2-(4-chlorophenoxy)propanoic acid (0.050 g, 0.2 mmol) in CH₂Cl₂ (3 ml) was added 1-(3-dimethylaminopropyl)-3-ethylcarbodiimide hydrochloride (0.048 g, 0.3 mmol), 4-dimethylaminopyridine (0.003 g, 0.025 mmol), and finally (*R*)-(+)-alpha-methylbenzylamine

(0.032 ml, 0.2 mmol). The mixture was stirred at ambient temperature for 24 h. The reaction mixture was then washed with saturated aqueous ammonium chloride, water and brine. The organic layer was separated, dried over magnesium sulfate, filtered and concentrated. The crude product was purified by flash column chromatography (0-50% EtOAc/hexanes) to yield 30 mg (40%) of the title compound as a white solid. ¹H NMR (400 MHz, CDCl₃) δ 7.36-7.40 (m, 2H), 7.27-7.32 (m, 5H), 6.86-6.90 (m, 2H), 6.59 (d, *J* = 7.8 Hz, 1H), 5.15-5.20 (m, 1H), 4.66 (q, *J* = 6.8 Hz, 1H), 1.56 (d, *J* = 6.6 Hz, 3H), 1.43 (d, *J* = 6.8 Hz, 3H); ¹³C NMR (100 MHz, CDCl₃) δ 170.84, 155.49, 142.68, 129.79, 127.53, 127.12, 126.05, 116.87, 75.59, 48.27, 21.63, 18.68; LCMS *m/z* 304 (MH⁺).

Synthesis of (2*R*)-2-(4-chlorophenoxy)-*N*-[(1*R*)-1-phenylethyl]propanamide:



To a solution of ethyl (2*R*)-2-(4-chlorophenoxy)propanoate (0.1 g, 0.44 mmol) in a 2:1 mixture of ethanol-water (6 ml) was added 1 M aqueous lithium hydroxide solution (0.88 ml, 0.88 mmol). The mixture was stirred at ambient temperature for 18 h. The reaction mixture was concentrated *in vacuo* to remove ethanol, diluted with water and adjusted to pH 2 with 1N aqueous hydrochloric acid solution. The mixture was extracted with ethyl acetate. The organic extracts were washed with brine, dried over magnesium sulfate and concentrated to obtain 85 mg of (2*R*)-2-(4-chlorophenoxy)propanoic acid as a white solid. This material was used directly in the next step.

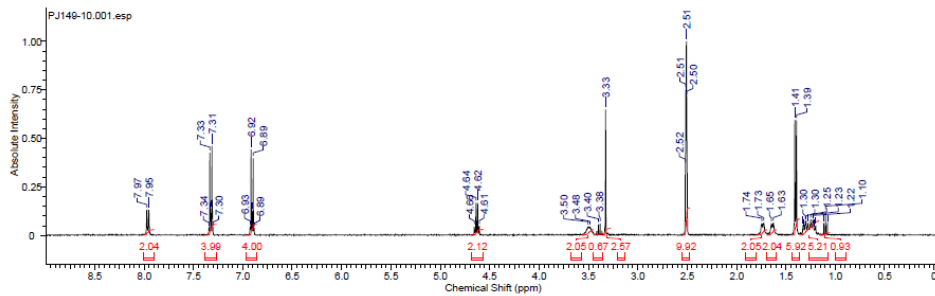
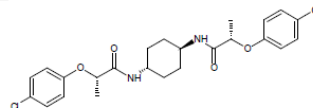
To a solution of the (2*R*)-2-(4-chlorophenoxy)propanoic acid (0.085 g, 0.42 mmol) in CH₂Cl₂ (5 ml) was added 1-(3-dimethylaminopropyl)-3-ethylcarbodiimide hydrochloride (0.082 g, 0.43 mmol), 4-dimethylaminopyridine (0.005 g, 0.042 mmol), and finally (*R*)-(+)- α -methylbenzylamine (0.054 ml, 0.42 mmol). The mixture was stirred at ambient temperature for 24 hours. The reaction mixture was then washed with saturated aqueous ammonium chloride, water and brine. The organic layer was separated, dried over magnesium sulfate, filtered and concentrated. The crude product was purified by flash column chromatography (0-50% EtOAc/hexanes) to yield 70 mg (54%) of the title compound as a white solid. ¹H NMR (400 MHz, CDCl₃) δ 7.21-7.26 (m, 5H), 7.09-7.11 (m, 2H), 6.79-6.83 (m, 2H), 6.56-6.58 (m, 1H), 5.10-5.18 (m, 1H), 4.63 (q, *J* = 6.7 Hz, 1H), 1.61 (d, *J* = 6.6 Hz, 3H), 1.52 (d, *J* = 7.1 Hz, 3H); ¹³C NMR (100 MHz, CDCl₃) δ 170.96, 155.46, 142.67, 129.67, 128.58, 127.36, 127.08, 125.91, 116.89, 75.50, 48.30, 21.80, 18.77; LCMS *m/z* 304 (MH⁺).

Synthesis Validation

10/12/2017 12:32:42 PM

(2S)-2-(4-Chlorophenoxy)-N-[(1R,4R)-4-[(2S)-2-(4-chlorophenoxy)propanamido]cyclohexyl]propanamide (1014817)

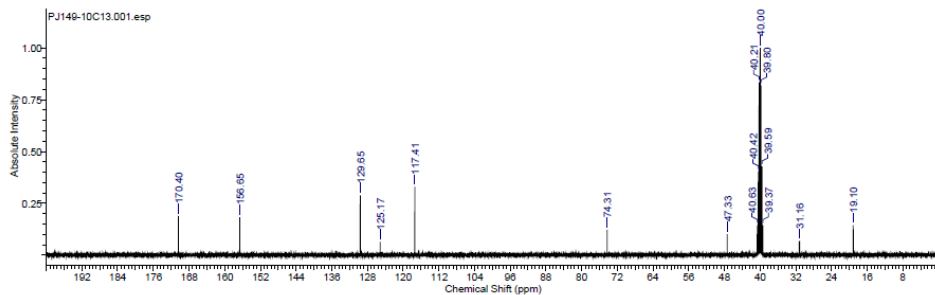
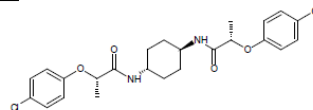
Acquisition Time (sec)	Comment	Z118098_0411 (PA BBO 400S1 BBF-H-D-05.2.SF)	Date
4.1099			15 Feb 2017 14:24:00
Date Stamp	File Name	Number of Transients	Origin
15 Feb 2017 14:24:00	C:\Users\priya\Desktop\NMR\Spectra\NMR#149\149FTD\SI\PJ149-10\11.fid	16	spect
Frequency (MHz)	Nucleus	Points Count	Pulse Sequence
399.54	¹ H	32768	zg30
Original Points Count	Owner	Solvent	Spectrum Offset (Hz)
32768	SMDC_A	DMSO-d6	2467.1362
Receiver Gain	SW(cyclical) (Hz)	Temperature (degree C)	
186.07	7878.72	24.996	
Spectrum Type	Sweep Width (Hz)		
STANDARD	7878.46		



10/12/2017 12:35:49 PM

(2S)-2-(4-Chlorophenoxy)-N-[(1R,4R)-4-[(2S)-2-(4-chlorophenoxy)propanamido]cyclohexyl]propanamide (1014817)

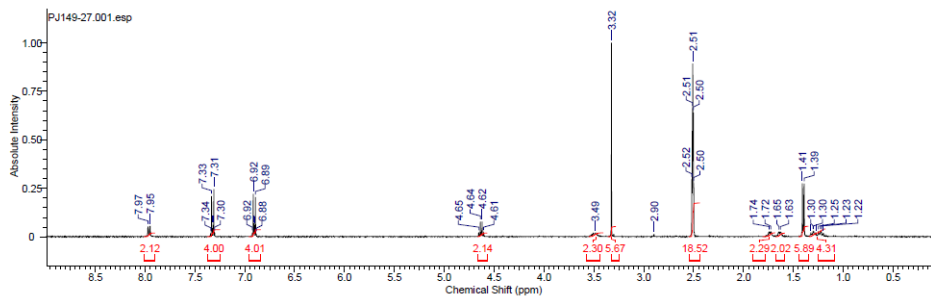
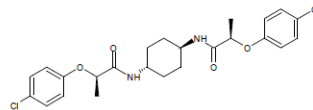
Acquisition Time (sec)	Comment	Z118098_0411 (PA BBO 400S1 BBF-H-D-05.2.SF)	Date
1.3631			12 Oct 2017 09:42:40
Date Stamp	File Name	Number of Transients	Origin
12 Oct 2017 09:42:40	C:\Users\priya\Desktop\NMR\Spectra\NMR#149\149FTD\SI\PJ149-10C13\11.fid	167	spect
Frequency (MHz)	Nucleus	Points Count	Pulse Sequence
100.46	¹³ C	32768	zgpg30
Original Points Count	Owner	Solvent	Spectrum Offset (Hz)
32768	SMDC_A	DMSO-d6	10046.3408
Receiver Gain	SW(cyclical) (Hz)	Temperature (degree C)	
208.51	24038.46	24.996	
Spectrum Type	Sweep Width (Hz)		
STANDARD	24037.73		



10/12/2017 12:38:37 PM

(2R)-2-(4-Chlorophenoxy)-N-[(1R,4r)-4-[(2R)-2-(4-chlorophenoxy)propanamido]cyclohexyl]propanamide (1014869)

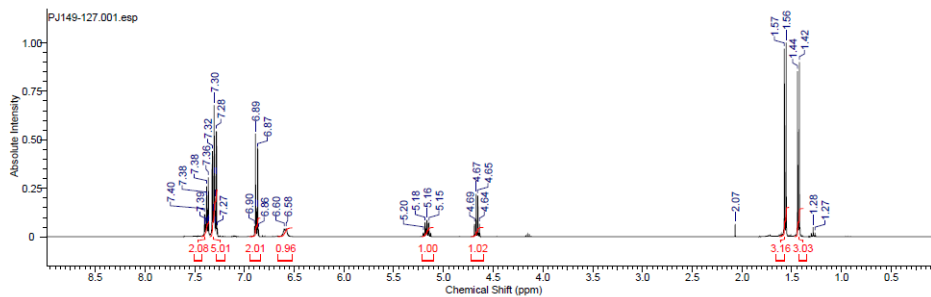
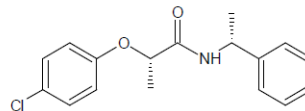
Acquisition Time (sec)	4.1069	Comment	Z116098_0411 (PA BBO 400S1 BBF.H-D-05 Z SP)	Date	15 Mar 2017 09:23:28
Date Stamp	15 Mar 2017 09:23:28	File Name	C:\Users\priya\Desktop\NMR\Spectra\NMR#149\149FTD\9\PU149-27\11fid	Origin	spect
Frequency (MHz)	399.54	Nucleus	¹ H	Number of Transients	16
Original Points Count	32768	Owner	SMDC A	Points Count	32768
Receiver Gain	185.41	SW(cyclical) (Hz)	7978.72	Solvent	DMSO-d6
Spectrum Type	STANDARD	Sweep Width (Hz)	7978.48	Temperature (degree C)	25.002



10/10/2017 11:16:06 AM

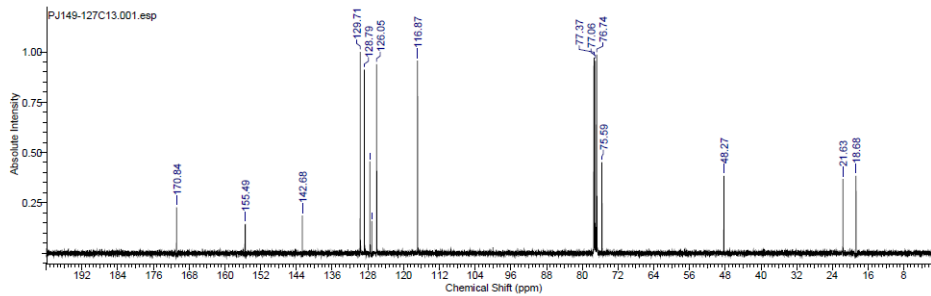
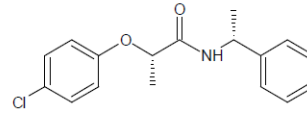
(2S)-2-(4-chlorophenoxy)-N-[(1R)-1-phenylethyl]propanamide

Acquisition Time (sec)	4.1069	Comment	Z116098_0411 (PA BBO 400S1 BBF.H-D-05 Z SP)	Date	25 Sep 2017 10:12:32
Date Stamp	25 Sep 2017 10:12:32	File Name	C:\Users\priya\Desktop\NMR\Spectra\NMR#149\149FTD\9\PU149-127\11fid	Origin	spect
Frequency (MHz)	399.54	Nucleus	¹ H	Number of Transients	16
Original Points Count	32768	Owner	SMDC A	Points Count	32768
Receiver Gain	74.50	SW(cyclical) (Hz)	7978.72	Solvent	CHLOROFORM-d
Spectrum Offset (Hz)	2467.1362	Spectrum Type	STANDARD	Sweep Width (Hz)	7978.48
				Temperature (degree C)	25.002



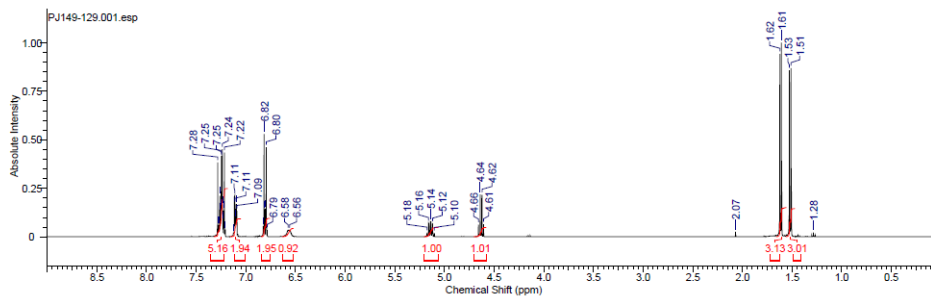
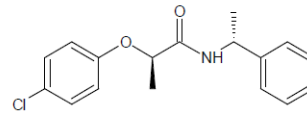
10/12/2017 11:22:58 AM
 (2S)-2-(4-chlorophenoxy)-N-[(1R)-1-phenylethyl]propanamide

Acquisition Time (sec)	1.3631	Comment	Z116098_0411 (PA BBO 400S1 BBF-H-D-05 Z SP)	Date	25 Sep 2017 10:16:48
Date Stamp	25 Sep 2017 10:16:48	Nucleus	¹³ C	File Name	C:\Users\priya\Desktop\NMR\Spectral\NMR#149\149FTD's\PJ149-127C13\1\fid
Frequency (MHz)	100.46	Owner	SMDC A	Number of Transients	130
Original Points Count	32768	SW (cyclical) (Hz)	24038.46	Points Count	32768
Receiver Gain	208.51	Spectrum Type	STANDARD	Solvent	CHLOROFORM-d
Spectrum Offset (Hz)	10046.3408			Sweep Width (Hz)	24037.73
				Temperature (degree C)	25.008



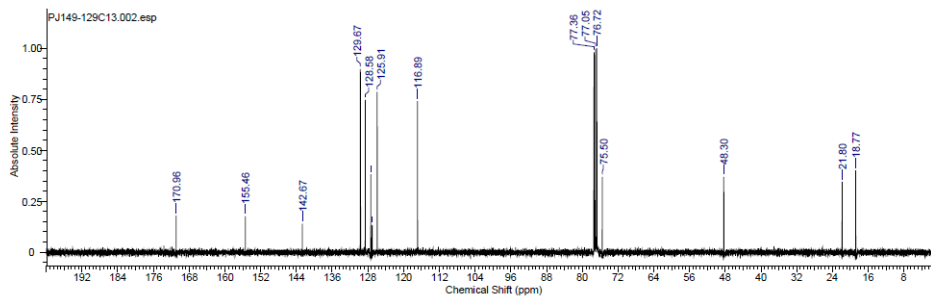
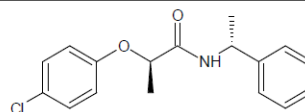
10/12/2017 11:29:54 AM
 (2R)-2-(4-chlorophenoxy)-N-[(1R)-1-phenylethyl]propanamide

Acquisition Time (sec)	4.1069	Comment	Z116098_0411 (PA BBO 400S1 BBF-H-D-05 Z SP)	Date	27 Sep 2017 13:03:12
Date Stamp	27 Sep 2017 13:03:12	Nucleus	¹ H	File Name	C:\Users\priya\Desktop\NMR\Spectral\NMR#149\149FTD's\PJ149-129\1\fid
Frequency (MHz)	399.54	Owner	SMDC A	Number of Transients	16
Original Points Count	32768	SW (cyclical) (Hz)	7978.72	Points Count	32768
Receiver Gain	93.24	Spectrum Type	STANDARD	Solvent	CHLOROFORM-d
Spectrum Offset (Hz)	2467.1362			Sweep Width (Hz)	7978.48
				Temperature (degree C)	24.999



10/12/2017 12:26:50 PM
(2R)-2-(4-chlorophenoxy)-N-(1R)-1-phenylethylpropanamide

Acquisition Time (sec)	1.3631	Comment	Z116098_0411 (PA BBO 400S1 BBF-H-D-05 Z SP)	Date	27 Sep 2017 13:13:52
Date Stamp	27 Sep 2017 13:13:52	File Name	C:\Users\priya\Desktop\NMR\Spectra\NMR#149\149FTD\SI\PJ149-129C13\2\fid		
Frequency (MHz)	100.46	Nucleus	¹³ C	Number of Transients	131
Original Points Count	32768	Owner	SMDC A	Points Count	32768
Receiver Gain	208.51	SW (cyclical) (Hz)	24038.46	Solvent	CHLOROFORM-d
Spectrum Offset (Hz)	10046.3408	Spectrum Type	STANDARD	Sweep Width (Hz)	24037.73
				Temperature (degree C)	24.999



Sequences

> heIF2B1_alpha_codonopt

```
ATGGACGACAAAGAACTGATCGAATACTTCAAATCTCAGATGAAAGAAGACCC
GGACATGGCTTCTGCTGTTGCTGCTATCCGTACCCTGCTGGAGTTCCTGAAACGTGA
CAAAGGTGAAACCATCCAGGGTCTGCGTGCTAACCTGACCTCTGCTATCGAAACCCT
GTGCGGTGTTGACTCTTCTGTTGCTGTTTCTTCTGGTGGTGAACCTGTTCCCTGCGTTTC
ATCTCTCTGGCTTCTCTGGAATACTCTGACTACTCTAAATGCAAAAAAATCATGATC
GAACGTGGTGAACCTGTTCCCTGCGTCGTATCTCTCTGTCTCGTAACAAAATCGCTGAC
CTGTGCCACACCTTCATCAAAGACGGTGTACCATCCTGACCCACGCTTACTCTCGT
GTTGTTCTGCGTGTCTGGAAGCTGCTGTTGCTGCTAAAAAACGTTTCTCTGTTTACG
TTACCGAATCTCAGCCGGACCTGTCTGGTAAAAAAATGGCTAAAGCTCTGTGCCACC
TGAACGTTCCGGTTACCGTTGTTCTGGACGCTGCTGTTGGTTACATCATGGAAAAAG
CTGACCTGGTTATCGTTGGTGTGAAGGTGTTGTTGAAAACGGTGGTATCATCAACA
AAATCGGTACCAACCAGATGGCTGTTTGCCTAAAGCTCAGAACAACCGTTCTACG
TTGTTGCTGAATCTTTCAAATTCGTTCTGTTCCCGCTGAACCAGCAGGACGTTCC
GGACAAATTCAAATACAAAGCTGACACCCTGAAAGTTGCTCAGACCGGTCAGGACC
TGAAAGAAGAACACCCGTGGGTGACTACACCGCTCCGTCTCTGATCACCTGCTGT
TCACCGACCTGGGTGTTCTGACCCCGTCTGCTGTTTCTGACGAACTGATCAAACGTG
ACCTGTAA
```

>heIF2B2_beta_codonopt | 6x His tag, TEV site

```
ATGCATCACCATCATCACCACGGTGGTGGTCTGAAAACCTGTA CTCTCCAGTCT
CCGGTCTGCTGCTAAAGGTTCTGAACTGTCTGAACGTATCGAATCTTTCGTTGAA
ACCCTGAAACGTGGTGGTGGTCCGCGTCTTCTGAAAGAAATGGCTCGTGAAACCCTG
GGTCTGCTGCGTCAGATCATCACCAGCACCGTTGGTCTAACGCTGGTGAACCTGATG
GAACTGATCCGTCGTGAAGGTCGTCGTATGACCGCTGCTCAGCCGTCTGAAACCACC
GTTGGTAACATGGTTCGTCGTGTTCTGAAAATCATCCGTGAAGAATACGGTCGTCTG
CACGGTCGTTCTGACGAATCTGACCAGCAGGAATCTCTGCACAACTGCTGACCTCT
GGTGGTCTGAACGAAGACTTCTCTTCCACTACGCTCAGCTGCAGTCTAACATCATC
GAAGCTATCAACGAACTGCTGGTGAACCTGGAAGGTACGATGGAAAACATCGCTGC
TCAGGCTCTGGAACACATCCACTCTAACGAAGTTATCATGACCATCGGTTTCTCTCG
TACCGTTGAAGCTTTCCTGAAAGAAGCTGCTCGTAAACGTAAATTCCACGTTATCGT
TGCTGAATGCGCTCCGTTCTGCCAGGGTCACGAAATGGCTGTTAACCTGTCTAAAGC
TGGTATCGAAACCACCGTTATGACCGACGCTGCTATCTTCGCTGTTATGTCTCGTGTT
AACAAAGTTATCATCGGTACCAAAACCATCCTGGCTAACGGTGGTCTGCGTGCTGTT
ACCGGTACCCACACCCTGGCTCTGGCTGCTAAACACCCTCTACCCCGCTGATCGTT
TGCGCTCCGATGTTCAAACCTGTCTCCGCAGTTCCTCGAACGAAGAAGACTCTTCCAC
AAATTCGTTGCTCCGGAAGAAGTTCTGCCGTTACCCGAAGGTGACATCCTGGAAAAA
GTTTCTGTTCACTGCCCGGTTTTCGACTACGTTCCGCCGGAACCTGATCACCTGTTCA
TCTCTAACATCGGTGGTAACGCTCCGTCTTACATCTACCGTCTGATGTCTGAACTGTA
CCACCCGGACGACCACGTTCTGTAA
```

>heIF2B3_gamma_codonopt

```
ATGGAGTTCAGGCTGTTGTTATGGCTGTTGGTGGTGGTCTCGTATGACCGAC
CTGACCTCTTCTATCCCGAAACCGCTGCTGCCGGTTGGTAACAAACCGCTGATCTGG
TACCCGCTGAACCTGCTGGAACGTGTTGGTTTCGAAGAAGTTATCGTTGTTACCACC
```

CGTGACGTT CAGAAAGCTCTGTGCGCTGAGTTCAAATGAAAATGAAACCGGACAT
CGTTTGCATCCCGGACGACGCTGACATGGGTACCGCTGACTCTCTGCGTTACATCTA
CCCGAAACTGAAAACCGACGTTCTGGTTCTGTCTTGCGACCTGATCACCGACGTTGC
TCTGCACGAAGTTGTTGACCTGTTCCGTGCTTACGACGCTTCTCTGGCTATGCTGATG
CGTAAAGGTCAGGACTCTATCGAACCGGTTCCGGGTCAGAAAGGTAAAAAAAAAAGC
TGTTGAACAGCGTGAFTTCATCGGTGTTGACTCTACCGGTAAACGTCTGCTGTTTAT
GGCTAACGAAGCTGACCTGGACGAAGAACTGGTTATCAAAGGTTCTATCCTGCAGA
AACACCCGCGTATCCGTTTCCACACCGGTCTGGTTGACGCTCACCTGTACTGCCTGA
AAAAATACATCGTTGACTTCCTGATGGAAAACGGTTCTATCACCTCTATCCGTTCTG
AACTGATCCCGTACCTGGTTCGTAAACAGTTCTCTTCTGCTTCTTCTCAGCAGGGTCA
GGAAGAAAAAGAAAGACCTGAAAAAAAAAAGAACTGAAATCTCTGGACATCTAC
TCTTTCATCAAAGAAGCTAACACCCTGAACCTGGCTCCGTACGACGCTTGCTGGAAC
GCTTGCCGTGGTGACCGTTGGGAAGACCTGTCTCGTTCTCAGGTTTCGTTGCTACGTT
ACATCATGAAAGAAGGTCTGTGCTCTCGTGTCTTACCCTGGGTCTGTACATGGAAG
CTAACCGTCAGGTTCCGAAACTGCTGTCTGCTCTGTGCCCGGAAGAACCGCCGGTTC
ACTCTTCTGCTCAGATCGTTTCTAAACACCTGGTTGGTGTGACTCTCTGATCGGTCC
GGAAACCCAGATCGGTGAAAAATCTTCTATCAAACGTTCTGTTATCGGTTCTTCTTG
CCTGATCAAAGACCGTGTACCATACCAACTGCCTGCTGATGAACTCTGTTACCGT
TGAAGAAGGTTCTAACATCCAGGTTCTGTTATCTGCAACAACGCTGTTATCGAAAA
AGGTGCTGACATCAAAGACTGCCTGATCGGTTCTGGTCAGCGTATCGAAGCTAAAGC
TAAACGTGTTAACGAAGTTATCGTTGGTAACGACCAGCTGATGGAAATCTAA

>heIF2B4_delta_codonopt | isoform 2

ATGGCTGCTGTTGCTGTTGCTGTTTCGTGAAGACTCTGGTTCTGGTATGAAAGCTG
AACTGCCGCCGGGTCCGGGTGCTGTTGGTTCGTGAAATGACCAAAGAAGAAAAACTG
CAGCTGCGTAAAGAAAAAAACAGCAGAAAAAAAACGTAAAGAAGAAAAAGGTG
CTGAACCGGAAACCGGTTCTGCTGTTTCTGCTGCTCAGTGCCAGGTTGGTCCGACCC
GTGAACTGCCGGAATCTGGTATCCAGCTGGGTACCCCGCGTGAAAAAGTTCCGGCTG
GTCGTTCTAAAGCTGAACTGCGTGCTGAACGTCGTGCTAAACAGGAAGCTGAACGT
GCTCTGAAACAGGCTCGTAAAGGTGAACAGGGTGGTCCGCCGCCGAAAGCTTCTCC
GTCTACCGCTGGTGAAACCCCGTCTGGTGTAAACGTCGTGCCGGAATACCCGCAGGT
TGACGACCTGCTGCTGCGTCTGTTAAAAAACCGGAACGTCAGCAGGTTCCGAC
CCGTAAAGACTACGGTTCTAAAGTTTCTCTGTTCTCTCACCTGCCGCAGTACTCTCGT
CAGAACTCTCTGACCCAGTTCATGTCTATCCCGTCTTCTGTTATCCACCCGGCTATGG
TTCGTCTGGGTCTGCAGTACTCTCAGGGTCTGGTTTCTGGTTCTAACGCTCGTTGCAT
CGCTCTGCTGCGTGCTCTGCAGCAGGTTATCCAGGACTACACCACCCCGCCGAACGA
AGAACTGTCTCGTGACCTGGTTAACAAACTGAAACCGTACATGTCTTTCCTGACCCA
GTGCCGTCGCTGTCTGCTTCTATGCACAACGCTATCAAATTCCTGAACAAAGAAAT
CACCTCTGTTGGTTCTTCTAAACGTGAAGAAGAAGCTAAATCTGAACTGCGTGCTGC
TATCGACCGTTACGTTTCAGGAAAAAATCGTTCTGGCTGCTCAGGCTATCTCTCGTTTC
GCTTACCAGAAAATCTCTAACGGTGACGTTATCCTGGTTTACGGTTGCTCTTCTCTGG
TTTCTCGTATCCTGCAGGAAGCTTGGACCGAAGGTCGTCGTTTCCGTGTTGTTGTTGT
TGACTCTCGTCCGTGGCTGGAAGGTCGTCACACCCTGCGTTCTCTGGTTCACGCTGGT
GTTCCGGCTTCTTACCTGCTGATCCCGGCTGCTTCTTACGTTCTGCCGGAAGTTTCTA
AAGTTCTGCTGGGTGCTCACGCTCTGCTGGCTAACGGTTCTGTTATGTCTCGTGTGG
TACCGCTCAGCTGGCTCTGGTTGCTCGTGCTACAACGTTCCGGTTCTGGTTTGCTGC

TGTCTTGGTTCTCTCAGCGTGACACCACCGACAAAGGTCAGCAGCTGCGTAAAAACC
AGCAGCTGCAGCGTTTCATCCAGTGGCTGAAAGAAGCTGAAGAAGAATCTTCTGAA
GACGACTAA

ACKNOWLEDGEMENTS

We thank Jirka Peschek, Elif Karagöz, Robert Stroud, James Fraser, Geeta Narlikar, Ron Vale, Axel Brilot, Nicole Schirle Oakdale, Nathaniel Talledge, Pearl Tsai, Ni Mu, Joseph Choe, Christopher Upjohn, Matt Jacobson, Chakrapani Kalyanaraman, and the Walter and Frost labs for reagents, technical advice and helpful discussions. We thank Michael Braunfeld, David Bulkley, and Alexander Myasnikov of the UCSF Center for Advanced CryoEM and Daniel Toso and Paul Tobias of the Berkeley Bay Area CryoEM Facility, which are supported by in part from NIH grants S10OD020054 and 1S10OD021741 and the Howard Hughes Medical Institute (HHMI). We also thank Zhiheng Yu, Rick Huang, and Chuan Hong of the CryoEM Facility at the Janelia Research Campus of the HHMI. We thank the QB3 shared cluster and NIH grant 1S10OD021596-01 for computational support. The Titan X Pascal used for this research was donated by the NVIDIA Corporation. **Funding:** This work was supported by funding to AF from a Faculty Scholar grant from the HHMI, the Searle Scholars Program, and NIH grant 1DP2GM110772-01, and by funding to PW from Calico Life Sciences LLC, the Rogers Family Foundation, the Weill Foundation, and the HHMI. AF is a Chan Zuckerberg Biohub Investigator, and PW is an Investigator of the HHMI. **Author Contributions:** JCT, LMV, AAA, ARR, AF, PW: Conception & design, analysis and interpretation of data. JCT, LMV, AAA, PJ, HCN: Acquisition of data. JCT, LMV, AAA, AF, PW: Writing – original draft preparation. JCT, LMV, AAA, PJ, HCN, ARR, AF, PW: Writing – review & editing. **Competing Interests:** PW and ARR are inventors on US Patent 9708247 held by the Regents of the University of California that describes ISRIB and its analogs. Rights to the invention have been licensed by UCSF to Calico. **Accession Numbers:** Accession numbers for the human eIF2B structures determined with FREALIGN, cryoSPARC, and RELION, respectively, are as follows: EMD-7442, EMD-

7443, EMD-7444 (density maps; Electron Microscopy Data Bank) and 6CAJ (coordinates of atomic models; Protein Data Bank). **Data availability:** All data needed to evaluate the conclusions in the paper are present in the paper and/or the Supplementary Materials, and the structural data is available in public databases. All of the raw cryoEM particle images are available upon request. We thank Graham Pavitt for the GP6452 yeast strain used in the purification of eIF2 which is available under a material transfer agreement with The University of Manchester.

REFERENCES

1. R. P. Dalton, D. B. Lyons, S. Lomvardas, Co-Opting the Unfolded Protein Response to Elicit Olfactory Receptor Feedback. *CELL*. **155**, 321–332 (2013).
2. M. Costa-Mattioli *et al.*, Translational control of hippocampal synaptic plasticity and memory by the eIF2 α kinase GCN2. *Nature*. **436**, 1166–1173 (2005).
3. D. H. Munn *et al.*, GCN2 kinase in T cells mediates proliferative arrest and anergy induction in response to indoleamine 2,3-dioxygenase. *Immunity*. **22**, 633–642 (2005).
4. N. C. Wortham, M. Martinez, Y. Gordiyenko, C. V. Robinson, C. G. Proud, Analysis of the subunit organization of the eIF2B complex reveals new insights into its structure and regulation. *The FASEB Journal*. **28**, 2225–2237 (2014).
5. Y. Gordiyenko *et al.*, eIF2B is a decameric guanine nucleotide exchange factor with a $\gamma 2\epsilon 2$ tetrameric core. *Nat Commun*. **5**, 3902 (2014).
6. A. M. Bogorad *et al.*, Insights into the Architecture of the eIF2B $\alpha/\beta/\delta$ Regulatory Subcomplex. *Biochemistry*, 140520123219000 (2014).
7. B. Kuhle, N. K. Eulig, R. Ficner, Architecture of the eIF2B regulatory subcomplex and its implications for the regulation of guanine nucleotide exchange on eIF2. *Nucleic Acids Research*. **43**, 9994–10014 (2015).
8. K. Kashiwagi *et al.*, Crystal structure of eukaryotic translation initiation factor 2B. *Nature*. **531**, 122–125 (2016).
9. E. Gomez, S. S. Mohammad, G. D. Pavitt, Characterization of the minimal catalytic domain within eIF2B: the guanine-nucleotide exchange factor for translation initiation. *EMBO J*. **21**, 5292–5301 (2002).
10. W. M. Yang, A. G. Hinnebusch, Identification of a regulatory subcomplex in the guanine

- nucleotide exchange factor eIF2B that mediates inhibition by phosphorylated eIF2. *Molecular and Cellular Biology*. **16**, 6603–6616 (1996).
11. G. D. Pavitt, K. Ramaiah, S. R. Kimball, A. G. Hinnebusch, eIF2 independently binds two distinct eIF2B subcomplexes that catalyze and regulate guanine-nucleotide exchange. *Genes & Development*. **12**, 514–526 (1998).
 12. T. Krishnamoorthy, G. D. Pavitt, F. Zhang, T. E. Dever, A. G. Hinnebusch, Tight binding of the phosphorylated alpha subunit of initiation factor 2 (eIF2alpha) to the regulatory subunits of guanine nucleotide exchange factor eIF2B is required for inhibition of translation initiation. *Molecular and Cellular Biology*. **21**, 5018–5030 (2001).
 13. A. G. Hinnebusch, J. R. Lorsch, The Mechanism of Eukaryotic Translation Initiation: New Insights and Challenges. *Cold Spring Harbor Perspectives in Biology*. **4**, a011544–a011544 (2012).
 14. A. G. Hinnebusch, The scanning mechanism of eukaryotic translation initiation. *Annu. Rev. Biochem.* **83**, 779–812 (2014).
 15. H. P. Harding *et al.*, Regulated translation initiation controls stress-induced gene expression in mammalian cells. *Molecular Cell*. **6**, 1099–1108 (2000).
 16. K. M. Vattam, R. C. Wek, Reinitiation involving upstream ORFs regulates ATF4 mRNA translation in mammalian cells. *Proc. Natl. Acad. Sci. U.S.A.* **101**, 11269–11274 (2004).
 17. H. P. Harding *et al.*, An integrated stress response regulates amino acid metabolism and resistance to oxidative stress. *Molecular Cell*. **11**, 619–633 (2003).
 18. C. Sidrauski *et al.*, Pharmacological brake-release of mRNA translation enhances cognitive memory. *eLife*. **2**, e00498–e00498 (2013).
 19. C. Sidrauski, A. M. McGeachy, N. T. Ingolia, P. Walter, The small molecule ISRIB

- reverses the effects of eIF2 α phosphorylation on translation and stress granule assembly. *eLife*. **4** (2015), doi:10.7554/eLife.05033.
20. G. V. Di Prisco *et al.*, Translational control of mGluR-dependent long-term depression and object-place learning by eIF2 α . *Nature Neuroscience*. **17**, 1073–1082 (2014).
 21. H. P. Harding, D. Ron, in *Translational Control in Biology and Medicine*, M. B. Mathews, N. Sonenberg, J. W. B. Hershey, Eds. (Cold Spring Harbor, NY, 2007), pp. 345–368.
 22. P. Remondelli, M. Renna, The Endoplasmic Reticulum Unfolded Protein Response in Neurodegenerative Disorders and Its Potential Therapeutic Significance. *Front Mol Neurosci*. **10**, 187 (2017).
 23. J. Obacz *et al.*, Endoplasmic reticulum proteostasis in glioblastoma—From molecular mechanisms to therapeutic perspectives. *Sci. Signal*. **10**, eal2323 (2017).
 24. G. Martínez, C. Duran-Aniotz, F. Cabral-Miranda, J. P. Vivar, C. Hetz, Endoplasmic reticulum proteostasis impairment in aging. *Aging Cell*. **16**, 615–623 (2017).
 25. P. A. J. Leegwater *et al.*, Subunits of the translation initiation factor eIF2B are mutant in leukoencephalopathy with vanishing white matter. *Nature Genetics*. **29**, 383–388 (2001).
 26. M. Halliday *et al.*, Partial restoration of protein synthesis rates by the small molecule ISRIB prevents neurodegeneration without pancreatic toxicity. *Cell Death & Dis*. **6**, e1672–9 (2015).
 27. A. Chou *et al.*, Inhibition of the integrated stress response reverses cognitive deficits after traumatic brain injury. *Proc. Natl. Acad. Sci. U.S.A.* **114**, E6420–E6426 (2017).
 28. C. Sidrauski *et al.*, Pharmacological dimerization and activation of the exchange factor eIF2B antagonizes the integrated stress response. *Elife*. **4**, e07314 (2015).

29. Y. Sekine *et al.*, Mutations in a translation initiation factor identify the target of a memory-enhancing compound. *Science*. **348**, aaa6986–1030 (2015).
30. R. A. de Almeida *et al.*, A Yeast Purification System for Human Translation Initiation Factors eIF2 and eIF2B ϵ and Their Use in the Diagnosis of CACH/VWM Disease. *PLoS ONE*. **8**, e53958–11 (2013).
31. A. G. Rowlands, R. Panniers, E. C. Henshaw, The catalytic mechanism of guanine nucleotide exchange factor action and competitive inhibition by phosphorylated eukaryotic initiation factor 2. *J. Biol. Chem.* **263**, 5526–5533 (1988).
32. D. D. Williams, N. T. Price, A. J. Loughlin, C. G. Proud, Characterization of the mammalian initiation factor eIF2B complex as a GDP dissociation stimulator protein. *J. Biol. Chem.* **276**, 24697–24703 (2001).
33. B. L. Craddock, C. G. Proud, The alpha-subunit of the mammalian guanine nucleotide-exchange factor eIF-2B is essential for catalytic activity in vitro. *Biochem. Biophys. Res. Commun.* **220**, 843–847 (1996).
34. B. R. Hearn *et al.*, Structure-Activity Studies of Bis-O-Arylglycolamides: Inhibitors of the Integrated Stress Response. *ChemMedChem*. **11**, 870–880 (2016).
35. S. Q. Zheng *et al.*, MotionCor2: anisotropic correction of beam-induced motion for improved cryo-electron microscopy. *Nat Meth.* **14**, 331–332 (2017).
36. K. Zhang, Gctf: Real-time CTF determination and correction. *J. Struct. Biol.* **193**, 1–12 (2016).
37. D. Kimanius, B. O. Forsberg, S. H. Scheres, E. Lindahl, Accelerated cryo-EM structure determination with parallelisation using GPUs in RELION-2. *Elife*. **5**, e18722 (2016).
38. A. Punjani, J. L. Rubinstein, D. J. Fleet, M. A. Brubaker, cryoSPARC: algorithms for

- rapid unsupervised cryo-EM structure determination. *Nat Meth.* **14**, 290–296 (2017).
39. N. Grigorieff, Frealign: An Exploratory Tool for Single-Particle Cryo-EM. *Meth. Enzymol.* **579**, 191–226 (2016).
 40. E. F. Pettersen *et al.*, UCSF Chimera--a visualization system for exploratory research and analysis. *J Comput Chem.* **25**, 1605–1612 (2004).
 41. L. A. Kelley, S. Mezulis, C. M. Yates, M. N. Wass, M. J. E. Sternberg, The Phyre2 web portal for protein modeling, prediction and analysis. *Nat Protoc.* **10**, 845–858 (2015).
 42. T. B. Hiyama, T. Ito, H. Imataka, S. Yokoyama, Crystal Structure of the α Subunit of Human Translation Initiation Factor 2B. *Journal of Molecular Biology.* **392**, 937–951 (2009).
 43. N. W. Moriarty, R. W. Grosse-Kunstleve, P. D. Adams, electronic Ligand Builder and Optimization Workbench (eLBOW): a tool for ligand coordinate and restraint generation. *Acta Crystallogr. D Biol. Crystallogr.* **65**, 1074–1080 (2009).
 44. P. Emsley, B. Lohkamp, W. G. Scott, K. Cowtan, Features and development of Coot. *Acta Crystallogr. D Biol. Crystallogr.* **66**, 486–501 (2010).
 45. P. D. Adams *et al.*, PHENIX: a comprehensive Python-based system for macromolecular structure solution. *Acta Crystallogr. D Biol. Crystallogr.* **66**, 213–221 (2010).
 46. V. B. Chen *et al.*, MolProbity: all-atom structure validation for macromolecular crystallography. *Acta Crystallogr. D Biol. Crystallogr.* **66**, 12–21 (2010).
 47. S. J. Ludtke, Single-Particle Refinement and Variability Analysis in EMAN2.1. *Meth. Enzymol.* **579**, 159–189 (2016).
 48. P. Schuck, Size-distribution analysis of macromolecules by sedimentation velocity ultracentrifugation and Lamm equation modeling. *Biophys. J.* **78**, 1606–1619 (2000).

49. A. F. Zyryanova *et al.*, Binding of the integrated stress response inhibitor, ISRIB, reveals a regulatory site in the nucleotide exchange factor, eIF2B. *bioRxiv*. 224824 (2017).

Appendix A

Pharmacokinetics of ISRIB 1.5

MATERIALS AND METHODS

Formulation

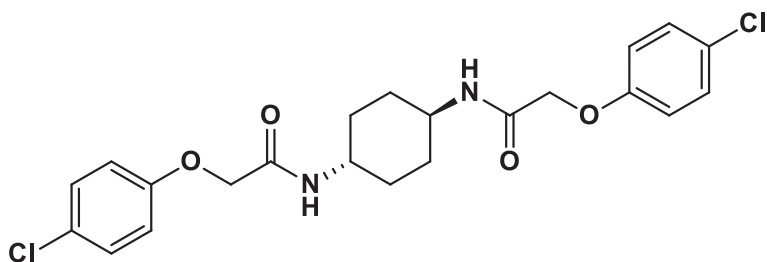
ISRIB 1.0 or ISRIB 1.5 were prepared the day of administration and dissolved into 5 mg/ml in either DMSO or NMP by vortexing, heating, and sonication. Immediately prior to PO dosing nine volumes of HPMT was slowly added to 5 mg/ml solvent dissolved ISRIB to generate a milky suspension of 0.5 mg/ml. Mice were subsequently dosed at 10 ul/g. Immediately prior to IP dosing, solvent dissolved ISRIB 1.0 or ISRIB 1.5 was diluted to 4 mg/ml and combined 1:1 with PEG400. Mice were then dosed at 2.5 ul/g.

ACKNOWLEDGEMENTS

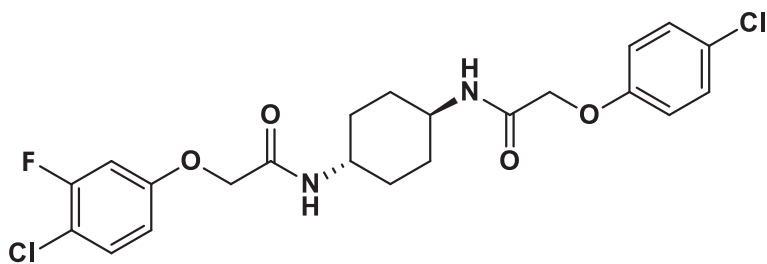
This work was done in collaboration with Byron Hann and Paul Phojanakong at the UCSF Preclinical Therapeutics Core. Design and conception by Jordan Tsai, Aditya Anand, and Peter Walter.

Figure A-1

(A)

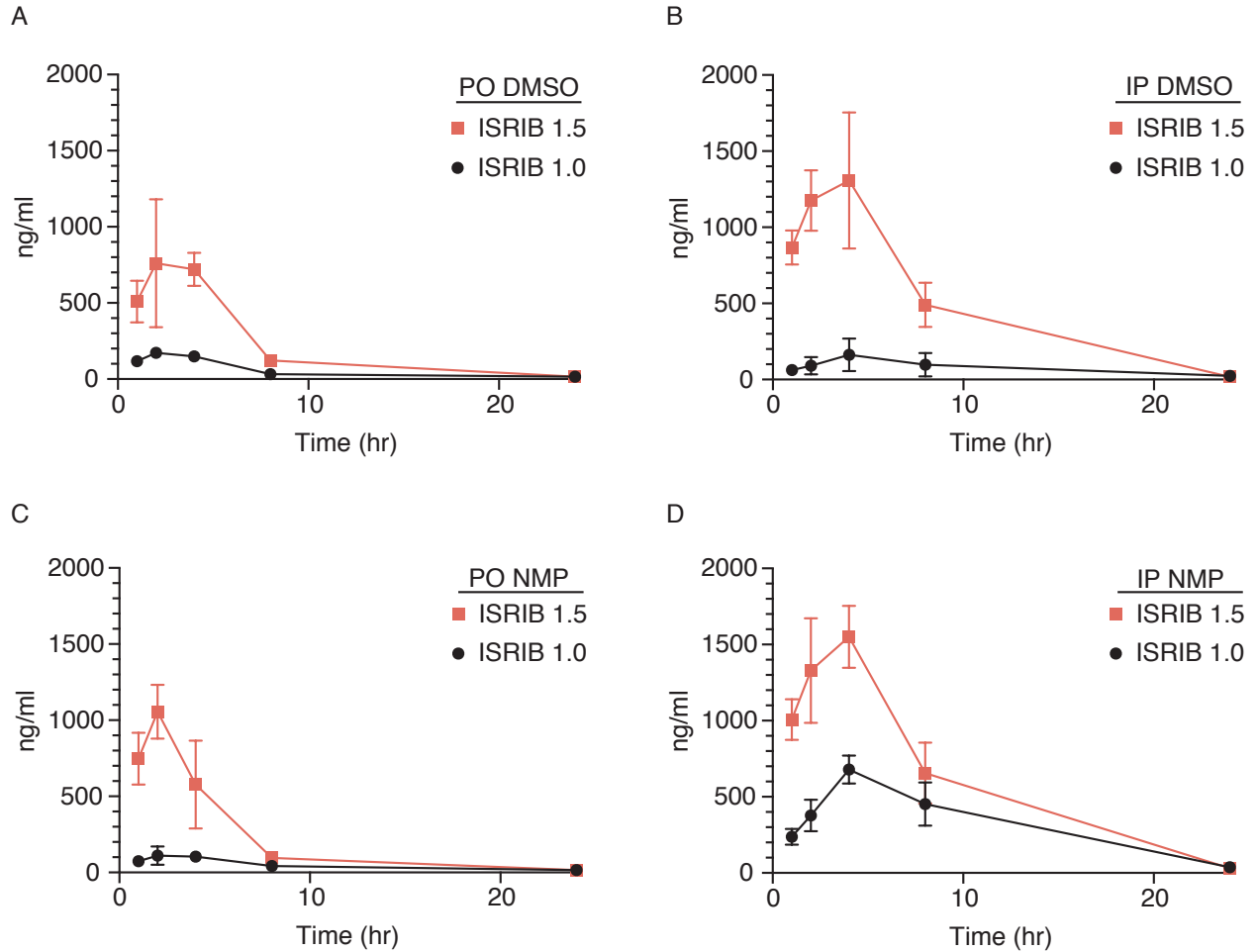


(B)



Structures of (A) ISRIB 1.0 and analog (B) ISRIB 1.5

Figure A-2



Pharmacokinetics summary Plasma concentrations measured for (A) PO or (B) IP administration of ISRIB 1.0 and ISRIB 1.5 in a DMSO solvent. Plasma concentrations measured for (C) PO or (D) IP administration of ISRIB 1.0 and ISRIB 1.5 in a N-Methyl-2-pyrrolidone (NMP) solvent. Points displayed represent mean \pm SD; n=3 for collection at 1, 2, 4, 8, and 24 hours after dosing.

Table A-1**Dosing route and volume**

Ear tag	Weight (g)	ISIRIB (solvent)	Route	Dosing Volume (μ l)
341	30.6	1.0 (DMSO)	PO	306
342	28.1	1.0 (DMSO)	PO	281
343	30.8	1.0 (DMSO)	PO	308
344	30	1.0 (NMP)	PO	300
345	26.9	1.0 (NMP)	PO	269
346	30.7	1.0 (NMP)	PO	307
347	32.2	1.5 (DMSO)	PO	322
348	29.5	1.5 (DMSO)	PO	295
349	29	1.5 (DMSO)	PO	290
350	28.4	1.5 (NMP)	PO	284
351	27.6	1.5 (NMP)	PO	276
352	29.9	1.5 (NMP)	PO	299
353	30.2	1.0 (DMSO)	IP	302
354	30.1	1.0 (DMSO)	IP	301
355	26.4	1.0 (DMSO)	IP	264
356	29	1.0 (NMP)	IP	290
357	29.4	1.0 (NMP)	IP	294
358	26.8	1.0 (NMP)	IP	268
359	29.6	1.5 (DMSO)	IP	296
360	27.7	1.5 (DMSO)	IP	277
361	27.7	1.5 (DMSO)	IP	277
362	31.1	1.5 (NMP)	IP	311
363	31.2	1.5 (NMP)	IP	312
364	30.1	1.5 (NMP)	IP	301

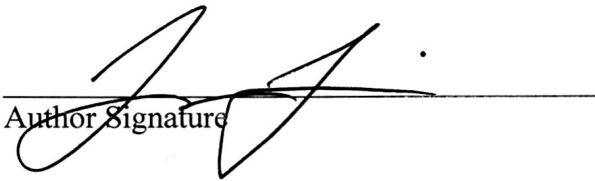
Publishing Agreement

It is the policy of the University to encourage the distribution of all theses, dissertations, and manuscripts. Copies of all UCSF theses, dissertations, and manuscripts will be routed to the library via the Graduate Division. The library will make all theses, dissertations, and manuscripts accessible to the public and will preserve these to the best of their abilities, in perpetuity.

Please sign the following statement:

I hereby grant permission to the Graduate Division of the University of California, San Francisco to release copies of my thesis, dissertation, or manuscript to the Campus Library to provide access and preservation, in whole or in part, in perpetuity.

Author Signature

A handwritten signature in black ink, consisting of stylized, overlapping loops and lines, written over a horizontal line.

March 23, 2018
Date